NTNU

Norwegian University of
Science and Technology

Finite Element Approximation of the Acoustic Impedance in Transducer Layers Comprising Silver Coated Monodisperse Polymer Spheres in a Polymer Adhesive

Sindre Kongshaug Blomvik

Master of Science in Mechanical Engineering
Submission date: June 2017
Supervisor: Leif Rune Hellevik, KT
Co-supervisor: Ole Martin Brende, SURF Technology AS
Ola Myhre, ISB

Norwegian University of Science and Technology
Department of Structural Engineering

Abstract

In this work, we study the acoustic impedance of Isotropic Conductive Adhesives (ICAs) consisting of silver coated monodisperse polymer spheres. These ICAs are intended to be used as thermal conductive isolation and matching layers in dual frequency ultrasound transducers because of their low acoustic impedance. In order to design the transducer layers, it is necessary to understand how the geometric parameters (such as particle size, coating thickness and particle density) alter the acoustic impedance. As far as the author know, there are no studies of the acoustic impedance of these ICAs. We use the Finite Element Method (FEM) and the Three Phase Model (TPM) (also known as the Generalized Self-Consistent Method) to approximate the effective acoustic impedance of composites and compare our results to experimentally measured acoustic impedances. Finally, we use the models to do numerical experiments in design. In conclusion, the TPM is just as good as the Finite Element (FE) model at approximating the homogeneous properties. However, we show that the composite used as a transducer layer may be too thin to be assumed homogeneous at a macroscopic level. Large particles seem favourable to use in thermal conductive transducer layers, and polystyrene is more favourable than PMMA as the core material.

Preface

This master's thesis is submitted to the Norwegian University of Science and Technology (NTNU) for the degree Master of Science. The work has been carried out at the Department of Structural Engineering, NTNU in the period between 15th of January and the 11th of June 2017.

Acknowledgements

I would like to thank my supervisor Leif Rune Hellevik for guidance throughout the semester. Furthermore, I thank Bjørn Atle Angelsen for trusting me with this problem. Also, I would like to give a special thanks to my co-supervisors Ole Martin Brende and Ola Myhre for sharing their thoughts, guiding me through the jungle of ultrasound and signal processing, as well as providing me with experimental data. In addition, I would like to thank my present and former roommates: Aksel Sveier, Cristian Livik, Eirik Aspesletten, Eirik Sandberg, Håkon Elvsaas, Kristoffer Helleve, Scott Green, Simen Bredvold, Sindre Løndal and Truls Bache.

The author is solely responsible for the content of this thesis.

Table of Contents

Abstract **i**

Preface **ii**

Table of Contents **v**

List of Tables **viii**

List of Figures **x**

Acronyms **xi**

Nomenclature **xiii**

1 Introduction **3**

2 Theory **7**

2.1 Elastic Materials 7

2.1.1 Linear Elastic Materials 8

2.1.2 Isotropic Elasticity 9

2.1.3 Elastic Waves 11

2.1.4 Reflection and Transmission 13

2.2 Ultrasound Transducer 16

2.2.1 Piezoelectric Element . . . 17
2.2.2 Matching Layers . . . 18
2.2.3 Isolation Layer . . . 20
2.3 Thermal Conductivity Using ICA . . . 21
2.4 Homogenization of Heterogeneous Material . . . 22
2.4.1 Representative Volume Element . . . 22
2.4.2 Volumetric Averaging . . . 22
2.4.3 Three Phase Model . . . 24
2.5 Finite Element Method . . . 26
2.5.1 Axisymmetric Stress and Strains . . . 27
2.5.2 Explicit Method . . . 28
2.5.3 Infinite Elements . . . 30

3 Finite Element Approximation of a Composite Material 33
3.1 Unit Cells . . . 36
3.2 Boundary Conditions and Infinite Elements . . . 38
3.3 Choice of Elements . . . 39
3.4 The Pressure Pulse . . . 40
3.5 Materials . . . 41
3.6 Time Delay Estimation . . . 42
3.7 Velocity Estimation . . . 45
3.8 Computational Costs . . . 47
3.9 Two-Step Homogenization scheme . . . 48
3.10 Verification of the FE model . . . 49
3.10.1 Method . . . 49
3.10.2 Results . . . 54
3.10.3 Discussion . . . 61
3.11 Comparing the FE Model with the ICA . . . 68
3.12 Numerical Experiment in Design . . . 71

4 Results **75**

4.1 Comparing the FE Model with the ICA 75

4.2 Numerical Experiment in Design 77

4.2.1 Young's Modulus 78

4.2.2 Poisson's Ratio 79

4.2.3 Density 80

4.2.4 Radius 81

4.2.5 Shell Thickness 82

4.2.6 Scaling 83

4.2.7 Contact Width 84

4.2.8 Volume Fraction of Particles 85

4.2.9 Ideal Concentration 86

5 Discussion **87**

5.1 FE Model Approximations 87

5.2 Comparing the FE Model with the ICA 88

5.3 Numerical Experiment in Design 90

6 Conclusion **93**

6.1 Future Work 93

Bibliography **94**

List of Tables

3.1 Material parameters used in the FE models. 42

3.2 Mesh study of the ordered FE model with silver as the only material. 59

3.3 Mesh study of the random FE model with silver as the only material. 59

3.4 Mesh study of the ordered FE model for the composite. 59

3.5 Mesh study of the random FE model for the composite 60

3.6 Particles and measured data provided by SURF Technology 70

4.1 Acoustic impedance of particles with $\eta = 140\,\mathrm{nm}$ 75

4.2 Acoustic impedance of particles with $R = 5\,\mu\mathrm{m}$ 76

4.3 Young's modulus of the core. 78

4.4 Young's modulus of the shell. 78

4.5 Young's modulus of the matrix. 78

4.6 Poisson's ratio of the core. 79

4.7 Poisson's ratio of the shell. 79

4.8 Poisson's ratio of the matrix. 79

4.9 Density of the core. 80

4.10 Density of the shell. 80

4.11 Density of the matrix. 80

4.12 Radius of the core. 81

4.13 Thickness of the shell. 82

4.14 Scaling of the particle. 83
4.15 Contact width between particles. 84
4.16 Volume fraction of particles. 85

5.1 Parameters sorted by the most sensitive. 91

List of Figures

1.1 Transducer stack. 5

2.1 Reflection and transmission of an incident wave 13
2.2 Waves in the piezo electric element 18
2.3 Reflection and transmission of waves in the matching layer. 19
2.4 The Three Phase Model. 24
2.5 Axisymmetric stress and strains. 28

3.1 Cross-sections of contact zones between particles. 36
3.2 The unit cells. 37
3.3 The contact zone between two particles. 38
3.4 The boundaries of the FE model. 38
3.5 The axisymmetric approximation of the composite. 39
3.6 Reflection from adjacent particles 39
3.7 The pressure pulse used in ABAQUS. 41
3.8 Velocity estimation 43
3.9 Tukey filter. 45
3.10 Integration point. 45
3.11 Velocity profiles. 46
3.12 The weighted average. 47
3.13 Computational costs 48

3.14 Two step homogenization scheme 48
3.15 PMMA with $R = 5\,\mu\text{m}$, $\eta = 0.1\,\mu\text{m}$, $\vartheta_p = 0.55$ and $\xi = 0.5\,\mu\text{m}$ 54
3.16 PMMA with $R = 10\,\mu\text{m}$, $\eta = 0.1\,\mu\text{m}$, $\vartheta_p = 0.55$ and $\xi = 0.5\,\mu\text{m}$ 55
3.17 PMMA with $R = 15\,\mu\text{m}$, $\eta = 0.1\,\mu\text{m}$, $\vartheta_p = 0.55$ and $\xi = 0.5\,\mu\text{m}$ 55
3.18 PMMA with $R = 8\,\mu\text{m}$, $\eta = 0.2\,\mu\text{m}$, $\vartheta_p = 0.45$ and $\xi = 1.5\,\mu\text{m}$ 56
3.19 Polystyrene with $R = 5\,\mu\text{m}$, $\eta = 0.1\,\mu\text{m}$ and $\vartheta_p = 0.55$ 56
3.20 Polystyrene with $R = 10\,\mu\text{m}$, $\eta = 0.1\,\mu\text{m}$ and $\vartheta_p = 0.55$ 57
3.21 Polystyrene with $R = 15\,\mu\text{m}$, $\eta = 0.1\,\mu\text{m}$ and $\vartheta_p = 0.55$ 57
3.22 Polystyrene with $R = 8\,\mu\text{m}$, $\eta = 0.2\,\mu\text{m}$ and $\vartheta_p = 0.45$ 58
3.23 The velocity profiles with different meshing. 60
3.24 Random model boundaries. 61

4.1 Comparison with measured impedance 76
4.2 Young's modulus 78
4.3 Poisson's ratio 79
4.4 Density 80
4.5 Core radius 81
4.6 Shell thickness 82
4.7 Scaling 83
4.8 Contact width 84
4.9 Volume fraction of particles 85
4.10 Ideal volume fraction of shell material 86
4.11 The ideal volume fraction of particles 86

Acronyms

FE Finite Element.

FEA Finite Element Analysis.

FEM Finite Element Method.

HF High Frequency.

ICA Isotropic Conductive Adhesive.

LF Low Frequency.

PE piezoelectric.

PMMA Poly(methyl methacrylate).

PS Polystyrene.

RVE Representative Volume Element.

SURF Second-order UltRasound Field.

TDE Time Delay Estimation.

TPM Three Phase Model.

Nomenclature

A	Wave amplitude
B	Strain-displacement matrix
C_{ijkl}	Forth order compliance tensor
$\hat{D}^{\mathrm{XC}}$	Approximated time delay
E	Young's modulus
$\mathbf{F^{ext}}$	External loading vector
G	Shear modulus; Damping matrix
$\mathbf{H}$	Zero-divergence vector used in the Helmholtz Decomposition
J	Wave intensity
K	Stiffness matrix
L	Thickness of the matching layer/sample
L^{elem}	Characteristic length of the smallest element
M	Mass matrix
N	Interpolation functions matrix
$P\left(t\right)$	Pressure pulse
R	Radius of the core
$R^{12}_{\sigma/\dot{u}}$	Reflection coefficient of the stress/velocity field when propagating from medium 1 to medium 2
$\hat{R}^{\mathrm{XC}}$	Approximated cross-correlation
S	Surface

$T^{12}_{\sigma/\dot{u}}$	Transmission coefficient of the stress/velocity field when propagating from medium 1 to medium 2
T^{12}_{J}	Transmitted coefficient of the intensity propagating from medium 1 to medium 2
U_0	Strain energy
V	Volume of a RVE
Z_{L}	Longitudinal acoustic impedance
a_{ij}	Transformation matrix
c	Speed of sound
c_{L}	Longitudinal wave velocity
$\bar{c}_{\mathrm{L}}$	Approximated longitudinal velocity with the finest meshing
$\hat{c}_{\mathrm{L}}$	Approximated longitudinal velocity
c_{T}	Transverse wave velocity
$\mathbf{d}$	Nodal displacement vector
f	Frequency
f_i	Body force in the direction of the coordinate axis x_i
f_0	Centre frequency
h	Height of the unit cell
k	Wave number
t	Time
t_0	Time shift of cosine window
u_i	Displacement in the direction of the coordinate axis x_i
$\dot{u}_i$	Velocity in the direction of the coordinate axis x_i
$\ddot{u}_i$	Acceleration in the direction of the coordinate axis x_i
u^{I}	Incident displacement wave
u^{R}	Reflected displacement wave
u^{T}	Transmitted displacement wave
w	Width of the unit cell/FE model
Δ	Strain-displacement operator matrix
Φ	Traction force

α_{L}	Longitudinal dampening constant in infinite elements
α_{T}	Transverse dampening constant in infinite elements
δ	Length scale of averaging
δ_{ij}	Kronecker Delta
ε_{ij}	Second order strain tensor
ε_v	Volumetric strain
$\langle \varepsilon_{ij} \rangle$	Average strain
$\epsilon_{c_{\mathrm{L}}}^{\mathrm{RVE}}$	Error in longitudinal velocity of the RVE
$\epsilon_{c_{\mathrm{L}}}^{\mathrm{comp}}$	Error in longitudinal velocity of the composite material
$\epsilon_{c_{\mathrm{L}}}^{\mathrm{pure}}$	Error in longitudinal velocity of the pure material
η	Shell thickness
κ	Bulk modulus
λ	Lamé's first parameter
Λ	Wavelength
μ	Lamé's second parameter; Shear modulus
∇	Vector differential operator
ν	Poisson's ratio
ω	Angular frequency
Ψ	Scalar used in the Helmholtz Decomposition
ρ	Density
σ_{ij}	Second order stress tensor
σ_H	Hydrostatic stress
$\langle \sigma_{ij} \rangle$	Average stress
τ	Time lag of cross-correlation
ϑ_p	Volume fraction of particles
ϑ_{I}	Volume fraction of inclusions
$\vartheta_{\mathrm{core}}$	Volume fraction of core in the particle
$\vartheta_{\mathrm{shell}}$	Volume fraction of shell in the particle
ξ	Radius of the contact zone between connected particles

Chapter 1

Introduction

Ultrasonic treatment and imaging is based upon the use of an ultrasonic transducer. The transducer transmits acoustic waves into the body, commonly approximated as pressure waves, i.e. assuming the shear modulus of tissue is 0. By transmitting a continuous wave for a longer time period, tissue is heated due to thermoviscous losses in the wave propagation, and this effect is used in *treatment*. *Images* are made from echoes owing to reflections as the acoustic waves get reflected at interfaces of materials of different *acoustic impedance*. The *longitudinal* acoustic impedance is defined as

$$Z_{\mathrm{L}} = \rho c_{\mathrm{L}} \tag{1.1}$$

where ρ and c_L is the density and longitudinal wave velocity of the material, respectively. Acoustic impedance and how it affects reflection and transmission of acoustic energy will be further explained in chapter 2. Images are created by measuring the time delay and magnitude of the reflected waves. An imaging transducer thus sends out short pulses and records the echoes, whereas a treatment transducer may transmit a continuous acoustic wave. Treatment transducers usually transmit greater intensity, compared to imaging transducers. One limiting factor is heat generation, which causes delamination of the layers.

SURF Technologies develops dual frequency transducers that transmit both Low Frequency (LF) and High Frequency (HF) pulses. The LF pulse is used to manipulate the non-linear elasticity of the medium observed by the HF pulse to achieve optimal noise suppression.[20] This technique

is known as SURF (Second-order UltRasound Field) imaging. When designing the transducer stack used in SURF imaging, one uses what is known as *isolation layers* between the LF section and the HF section. Myhre *et. al.* [19] have shown that these isolation layers are of alternating high and low impedance, and suggested that these high impedance layers might function as heat sinks in the transducer stack.

SURF Technologies AS together with Conpart AS are exploring the possibility of using composites comprising silver coated monodisperse polymer spheres in polymer adhesive as a way of increasing the thermal conductivity of the low impedance isolation layers used in the ultrasound transducer stack. By increasing the thermal conductivity of the transducer layers, they can transport heat from the piezoelectric (PE) elements to the high impedance layers which can function as heat sinks. This type of conductive composite is known as an Isotropic Conductive Adhesive. As we will show in chapter 2, these transducer layers need specific mechanical properties to optimize the transmitted intensity into tissue.

There have been extensive studies of how solid particle reinforced adhesives alter the mechanical properties of transducer layers, and these particle reinforced layers are what is normally used to alter the acoustic impedance of transducer layers. As far as the author of this thesis know of, there is no information on how polymers reinforced with metal coated polymer spheres will alter the mechanical properties. We will in this thesis therefore shed some light on the mechanical properties and their impact on the acoustic impedance by doing numerical experiments in the design of the ICA. Note that whenever impedance is mentioned in this thesis, it is the *longitudinal specific acoustic impedance*.

Transducer layers need specific acoustic impedances, typically higher than the impedance of polymers. The common practice is to modify the polymers by mixing in metal powder to increase the acoustic impedance. By using the coated polymer spheres instead, one can utilize the necessary metal by moving it out to the periphery of the particles and obtain connectivity between the highly conductive particles. This is illustrated in fig. 1.1 for isolation layers.

An extensive amount of work has gone into developing the scripts used to generate FE models and to post-process data. The most important scripts can be found at `https://github.com/sindrebl/mastersthesis_scripts` where there is a README file that explains the use.

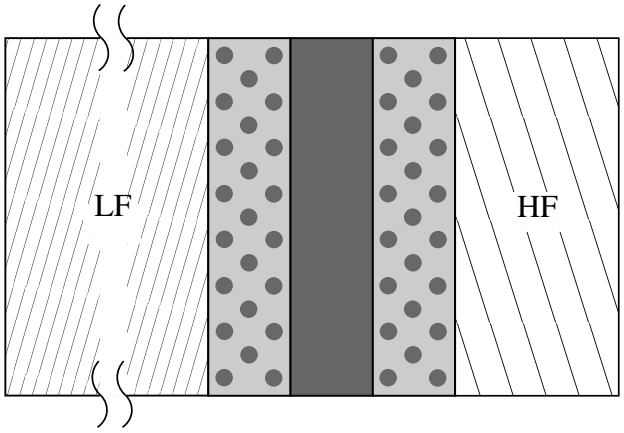

(a) Connectivity is not achieved using traditional transducer layers.

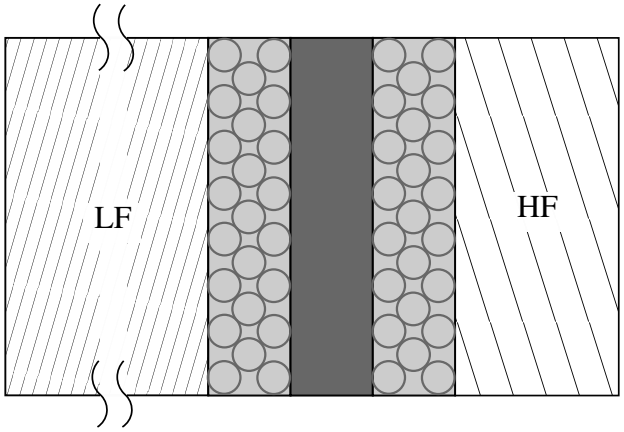

(b) Connectivity is achieved by using coated polymer spheres.

Figure 1.1: Transducer stack with a LF transducer, three isolation layers and a HF transducer.

These are just the basic scripts, as we have used a great number of models which usually require some changes for each case. We recommend the reader to take a look at these scripts while reading through chapter 3.

Chapter 2 covers relevant theory of elasticity and elastic waves, ultrasound and transducer layers, thermal conductivity using ICA and the Three Phase Model. Last is a section covering the Finite Element Method.

Chapter 3 explains the methods used to approximate the acoustic impedance using ABAQUS and MATLAB. We also present the method we use to compare our approximations to ICA and the method used for the numerical experiment in design. A verification study and its results are presented, and these results are used for all FE models for the rest of the thesis.

Chapter 4 presents the result of the comparison study and the numerical experiment in design.

Chapter 5 discusses the assumptions made in the FE model, how well the FE model and TPM describes the ICA, as well as discussing the design of the composite.

Chapter 6 presents the concluding remarks as well as future work that we would be interested in doing.

Chapter 2

Theory

In this chapter, we cover the relevant equations of elastic materials, and use them to derive expressions for the longitudinal and transverse velocity of stress waves. We will then cover the theory of reflection and transmission of stress waves and how they apply to ultrasound transducer layers. This is essential in order to understand the problem we address and in the understanding of the analyses and discussions later on. We also present the Three Phase Model, an analytic homogenization method that will be tested whether appropriate for use in our case. We finish with some background theory on the Finite Element Method.

2.1 Elastic Materials

The following theory is adapted from [11, 12]. A material is said to be *elastic* if, under isothermal conditions, the stress depends only on the strain. There is a unique relation between stresses and strains in the body and the stored elastic energy is independent of the strain path. Further, a material is said to be *hyperelastic* if there exists a strain energy function $U_0\left(\epsilon_{ij}\right)$ such that

$$\sigma_{ij} = \frac{\partial U_0}{\partial \varepsilon_{ij}}, \tag{2.1}$$

where σ_{ij} and ε_{ij} is the second order stress and strain tensor, respectively. As a result of eq. (2.1) the stresses are functions of the strains for hyperelastic materials: $\sigma_{ij} = \sigma_{ij}\left(\varepsilon_{ij}\right)$, thus implying

that there is a one-to-one relation between stresses and strains. Therefore, a hyperelastic material falls under the definition of elastic materials. Note that it is not necessarily the other way around.

2.1.1 Linear Elastic Materials

If the relation between the stress and strains in a material is linear, it is said to be *linear elastic*. The most general form of a linear elastic material is defined by the *generalized Hooke's law*

$$\sigma_{ij} = C_{ijkl}\varepsilon_{kl}, \tag{2.2}$$

where C_{ijkl} is a forth order tensor of elastic constants, or *compliances*. The *compliance tensor* has $3^4 = 81$ components. Under the assumption that the forces on a continuum only are contact forces and body forces, the law of balance of angular and linear momentum (known as *Euler's 1. & 2. axiom*) implies that the stress matrix is symmetric:

$$\sigma_{ij} = \sigma_{ji}. \tag{2.3}$$

Using the *Green strain tensor* for infinitesimal strains

$$\varepsilon_{kl} = \frac{1}{2}\left(\frac{\partial u_k}{\partial x_l} + \frac{\partial u_l}{\partial x_k}\right) \Leftrightarrow \varepsilon_{kl} = \frac{1}{2}\left(u_{k,l} + u_{l,k}\right), \tag{2.4}$$

where u_k is the displacement in the direction of the coordinate axis x_k. From eq. (2.4) it is straightforward to see that the strain tensor is symmetric, i.e. $\varepsilon_{kl} = \varepsilon_{lk}$.

The symmetries implied by eqs. (2.3) and (2.4) are referred to as the *minor symmetries*. Using these symmetries

$$\sigma_{ij} = \sigma_{ji} \Rightarrow C_{ijkl} = C_{jikl}, \tag{2.5}$$

$$\varepsilon_{kl} = \varepsilon_{lk} \Rightarrow C_{ijkl} = C_{jilk}, \tag{2.6}$$

and the compliance tensor is reduced from 81 to 36 independent coefficients. We now assume the material to be hyperelastic, and consider the stress-strain relation using the strain energy function

U_0 as in eq. (2.1).

$$\sigma_{ij} = \frac{\partial U_0}{\partial \varepsilon_{ij}} = C_{ijkl}\varepsilon_{kl}, \tag{2.7}$$

By differentiating σ_{ij} with respect to ε_{kl}, we find an expression for the compliance tensor

$$C_{ijkl} = \frac{\partial \sigma_{ij}}{\partial \varepsilon_{kl}} = \frac{\partial^2 U_0}{\partial \varepsilon_{kl}\partial \varepsilon_{ij}} = \frac{\partial^2 U_0}{\partial \varepsilon_{ij}\partial \varepsilon_{kl}} = C_{klij}. \tag{2.8}$$

By introducing the assumption of hyperelasticity, it implies that the compliance tensor exhibits in addition to the minor symmetries, the *major symmetries*

$$C_{ijkl} = C_{klij}, \tag{2.9}$$

and the compliance tensor is reduced further to 21 independent coefficients, a symmetric 6-by-6 matrix.

2.1.2 Isotropic Elasticity

For an isotropic elastic material, there are no preferred directions of orientation; the compliances at a given particle must be the same for all possible choices of Cartesian coordinate systems:

$$C^*_{ijkl} = C_{ijkl}, \tag{2.10}$$

where C^*_{ijkl} and C_{ijkl} are the compliance matrices for a coordinate system with basis vectors $(\mathbf{e}^*_i)$ and $(\mathbf{e}_i)$, respectively. For further simplification of the compliance tensor, a transformation rule for the tensor is needed. First, by integrating eq. (2.7), the strain energy function U_0 for a linear elastic material yields

$$U_0 = \frac{1}{2} C_{ijkl}\varepsilon_{ij}\varepsilon_{kl}. \tag{2.11}$$

Now, by expressing the strain energy function in two basis systems $(\mathbf{e}^*_i)$ and $(\mathbf{e}_i)$

$$U_0 = \frac{1}{2} C^*_{ijkl}\varepsilon^*_{ij}\varepsilon^*_{kl} = \frac{1}{2} C_{mnrs}\varepsilon_{mn}\varepsilon_{rs}, \tag{2.12}$$

where the relation between the two bases is given by a transformation matrix $\mathbf{a}$: $\mathbf{e}_i^* = a_{ij}\mathbf{e}_j$. Using the transformation rule for a second order tensor gives $\varepsilon_{mn} = a_{im}a_{jn}\varepsilon_{ij}^*$ and $\varepsilon_{rs} = a_{kr}a_{ls}\varepsilon_{kl}^*$. Inserting these expressions into eq. (2.12), we get

$$\left(C_{ijkl}^* - a_{im}a_{jn}a_{kr}a_{ls}C_{mnrs}\right)\varepsilon_{ij}^*\varepsilon_{kl}^* = 0. \tag{2.13}$$

Since ε is arbitrary, the expression inside the parenthesis is zero, and we have the transformation rule for C_{ijkl} as

$$C_{ijkl}^* = a_{im}a_{jn}a_{kr}a_{ls}C_{mnrs}. \tag{2.14}$$

By systematically rotating the system about the x_1, x_2 and the x_3 axis, using the rotation matrices:

$$\begin{bmatrix} 1 & 0 & 0 \\ 0 & \cos\theta & \sin\theta \\ 0 & -\sin\theta & \cos\theta \end{bmatrix}, \begin{bmatrix} \cos\theta & 0 & -\sin\theta \\ 0 & 1 & 0 \\ \sin\theta & 0 & \cos\theta \end{bmatrix} \quad \text{and} \quad \begin{bmatrix} \cos\theta & \sin\theta & 0 \\ -\sin\theta & \cos\theta & 0 \\ 0 & 0 & 1 \end{bmatrix}, \tag{2.15}$$

the compliance tensor is reduced to only two unknowns, the *Lamé parameters*, λ and μ, and we can express the compliance tensor as

$$C_{ijkl} = \lambda\delta_{ij}\delta_{kl} + \mu\left(\delta_{ik}\delta_{jl} + \delta_{il}\delta_{jk}\right), \tag{2.16}$$

where δ_{ij} is the Kronecker Delta. Substituting eq. (2.16) into eq. (2.2), results in the generalized Hooke's law for isotropic materials:

$$\sigma_{ij} = \lambda\varepsilon_{kk}\delta_{ij} + 2\mu\varepsilon_{ij}, \tag{2.17}$$

$$\varepsilon_{ij} = -\frac{\lambda}{2\mu\left(3\lambda + 2\mu\right)}\sigma_{kk}\delta_{ij} + \frac{1}{2\mu}\sigma_{ij}. \tag{2.18}$$

Now, let us introduce the *volumetric strain*, ε_{v}, and *hydrostatic stress*, σ_{H}, as

$$\varepsilon_{\mathrm{v}} = \varepsilon_{ii} \quad \text{and} \quad \sigma_{\mathrm{H}} = \frac{1}{3}\sigma_{ii}. \tag{2.19}$$

By computing the hydrostatic stress, using eq. (2.17), we find a relation between hydrostatic stress and volumetric strain, namely the *bulk modulus*, κ, as

$$\sigma_H = \kappa \epsilon_v, \quad \kappa = \lambda + \frac{2}{3}\mu. \tag{2.20}$$

The relation between the Lamé constants and the much-used elastic moduli, namely Young's modulus, E, shear modulus, G, and Poisson's ratio, ν is given by

$$\lambda = \frac{\nu E}{(1+\nu)(1-2\nu)} \quad \text{and} \quad \mu = G = \frac{E}{2(1+\nu)}. \tag{2.21}$$

The Young's modulus and Poisson's ratio can also be expressed using the bulk modulus and shear modulus as

$$E = \frac{9\kappa\mu}{3\kappa+\mu} \quad \text{and} \quad \nu = \frac{3\kappa - 2\mu}{2(3\kappa+\mu)}. \tag{2.22}$$

2.1.3 Elastic Waves

The theory is adopted from [10, 22]. The governing equation for wave propagation in three-dimensional infinite media can be derived from *The Cauchy's equation of motion:*

$$\rho \ddot{\mathbf{u}} = \rho \mathbf{f} + \nabla \sigma \quad \Leftrightarrow \quad \rho \ddot{u}_i = \rho f_i + \sigma_{ij,j}, \tag{2.23}$$

where f_i is a body force and $\ddot{u}_i$ is the acceleration in the direction of the coordinate axis x_i. Equation (2.23) is valid for motions in any continuum, both solids and liquids. Rewriting it using eqs. (2.4) and (2.17), we get what is known as the *Navier equations*

$$\rho \ddot{u}_i = (\lambda + \mu) u_{j,ij} + \mu u_{i,jj} + \rho f_i. \tag{2.24}$$

The vector equivalent of eq. (2.24) is

$$\rho \ddot{\mathbf{u}} = (\lambda + \mu) \nabla (\nabla \cdot \mathbf{u}) + \mu \nabla^2 \mathbf{u} + \rho \mathbf{f}. \tag{2.25}$$

Introducing the *Helmholtz Decomposition* as

$$\mathbf{u} = \nabla\Psi + \nabla \times \mathbf{H}, \quad \nabla \cdot \mathbf{H} = 0, \tag{2.26}$$

where a vector field $\mathbf{u}$ is expressed as the gradient of a scalar, Ψ, and the curl of the zero-divergence vector, $\mathbf{H}$. By neglecting the body forces in eq. (2.25) and expressing $\mathbf{u}$ using eq. (2.26), we get

$$\rho\left(\nabla\ddot{\Psi} + \nabla \times \ddot{\mathbf{H}}\right) = (\lambda + \mu)\,\nabla\left[\nabla \cdot (\nabla\Psi + \nabla \times \mathbf{H})\right] + \mu\nabla^2\left(\nabla\Psi + \nabla \times \mathbf{H}\right). \tag{2.27}$$

Then, using the following vector identities

$$\nabla^2\mathbf{u} = \nabla\left(\nabla \cdot \mathbf{u}\right) - \nabla \times \left(\nabla \times \mathbf{u}\right) \quad \text{and} \quad \nabla \cdot \left(\nabla \times \mathbf{H}\right) = 0, \tag{2.28}$$

eq. (2.27) is reduced to

$$\nabla\left[(\lambda + 2\mu)\,\nabla^2\Psi - \rho\ddot{\Psi}\right] + \nabla \times \left[\mu\nabla^2\mathbf{H} - \rho\ddot{\mathbf{H}}\right] = 0, \tag{2.29}$$

which is only satisfied if both terms vanish. This gives us the wave equations

$$\nabla^2\Psi = \frac{1}{c_{\mathrm{L}}^2}\frac{\partial^2\Psi}{\partial t^2}, \tag{2.30}$$

$$\nabla^2\mathbf{H} = \frac{1}{c_{\mathrm{T}}^2}\frac{\partial^2\mathbf{H}}{\partial t^2}, \tag{2.31}$$

where

$$c_{\mathrm{L}}^2 = \frac{\lambda + 2\mu}{\rho} \quad \text{and} \quad c_{\mathrm{T}}^2 = \frac{\mu}{\rho} \tag{2.32}$$

are the longitudinal and transverse wave velocity, respectively. Expressing it using the relation from eq. (2.21) yields

$$c_{\mathrm{L}}^2 = \frac{(1-\nu)}{(1+\nu)(1-2\nu)}\frac{E}{\rho} \quad \text{and} \quad c_{\mathrm{T}}^2 = \frac{1}{2(1+\nu)}\frac{E}{\rho}. \tag{2.33}$$

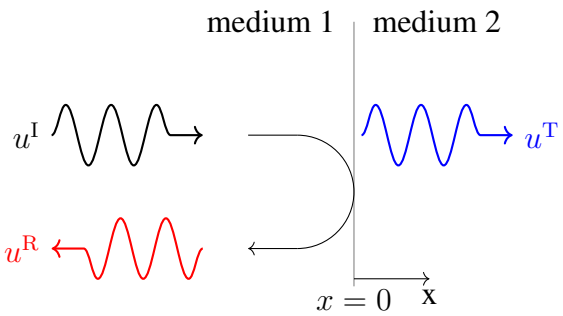

Figure 2.1: An incident wave being reflected and transmitted at the interface between two media of different acoustic impedance

2.1.4 Reflection and Transmission

Theory adopted from [22]. We are interested in finding an expression for the reflected and transmitted intensity of the acoustic waves. To do so, we need to find the expressions for both the reflected and transmitted stress and velocity field. We start by introducing a harmonic plane longitudinal displacement wave, u_i, propagating along coordinate axis x_i, described by the 1D version of eq. (2.30). It has the following general solution

$$u_i = A_1 e^{i(kx_i - \omega t)} + A_2 e^{-i(kx_i + \omega t)}, \tag{2.34}$$

where $k = \omega / c_{\mathrm{L}}$ is the wave number, ω is the angular frequency and A_1 & A_2 are the wave amplitudes. The first term in eq. (2.34) describes a wave propagating in the positive x_i-direction, known as *the forward propagating wave*, and the second term describes *the backward propagating wave*. Consider the problem in fig. 2.1. An incident harmonic plane longitudinal displacement wave, u^{I}, is propagating in the positive x-direction in medium 1. At the interface between the two media, it divides into two components; a transmitted displacement wave, u^{T}, and a reflected displacement wave, u^{R}. Consider the incident waveform as

$$u^{\mathrm{I}} = A^{\mathrm{I}} e^{i(k^{(1)} x - \omega t)}, \quad k^{(1)} = \frac{\omega}{c_{\mathrm{L}}^{(1)}}, \tag{2.35}$$

where the superscript "(1)" denotes medium 1. In this case, the reflected wave form can be written as

$$u^{\mathrm{R}} = A^{\mathrm{R}} e^{-i(k^{(1)}x+\omega t)}. \tag{2.36}$$

and the transmitted wave form propagating in the second medium is

$$u^{\mathrm{T}} = A^{\mathrm{T}} e^{i(k^{(2)}x-\omega t)}, \quad k^{(2)} = \frac{\omega}{c_{\mathrm{L}}^{(2)}}, \tag{2.37}$$

where A^{R} and A^{T} are unknown amplitudes of the waves. The entire elastic field in medium 1 is

$$u^{(1)} = u^{\mathrm{I}} + u^{\mathrm{R}} = A^{\mathrm{I}} e^{i(k^{(1)}x-\omega t)} + A^{\mathrm{R}} e^{-i(k^{(1)}x+\omega t)}, \tag{2.38}$$

and in medium 2,

$$u^{(2)} = u^{\mathrm{T}} = A^{\mathrm{T}} e^{i(k^{(2)}x-\omega t)}. \tag{2.39}$$

At the interface, the displacement and the stresses must be the same for medium 1 and 2. This gives us the following boundary conditions at the interface:

$$u^{(1)}|_{x=0} = u^{(2)}|_{x=0}, \tag{2.40}$$

$$\sigma^{(1)}|_{x=0} = \sigma^{(2)}|_{x=0}. \tag{2.41}$$

Using the generalized Hooke's law for isotropic materials eq. (2.17) and the assumption of infinite span in the transverse direction, the strains in transverse directions can be neglected. The normal stress can then be written as

$$\sigma_{11} = (\lambda + 2\mu)\,\varepsilon_{11} = (\lambda + 2\mu)\,\frac{\partial u_1}{\partial x_1}. \tag{2.42}$$

We find expressions for the incident, transmitted and reflected stress field by substituting eqs. (2.35) to (2.37) into eq. (2.42), which yields

$$\sigma_I = \left(\lambda^{(1)} + 2\mu^{(1)}\right) ik^{(1)} A^{\mathrm{I}} e^{i(k^{(1)}x - \omega t)}, \tag{2.43}$$

$$\sigma^{\mathrm{R}} = -\left(\lambda^{(1)} + 2\mu^{(1)}\right) ik^{(1)} A^{\mathrm{R}} e^{-i(k^{(1)}x + \omega t)}, \tag{2.44}$$

$$\sigma^{\mathrm{T}} = \left(\lambda^{(2)} + 2\mu^{(2)}\right) ik^{(2)} A^{\mathrm{T}} e^{i(k^{(2)}x - \omega t)}. \tag{2.45}$$

It follows that the stress fields in medium 1 and 2 are

$$\sigma_{11}^{(1)} = \left(\lambda^{(1)} + 2\mu^{(1)}\right) ik^{(1)} \left(A^{\mathrm{I}} e^{i(k^{(1)}x - \omega t)} - A^{\mathrm{R}} e^{-i(k^{(1)}x + \omega t)}\right), \tag{2.46}$$

$$\sigma_{11}^{(2)} = \left(\lambda^{(2)} + 2\mu^{(2)}\right) ik^{(2)} A^{\mathrm{T}} e^{i(k^{(2)}x - \omega t)}. \tag{2.47}$$

We want to find the relation between the incident amplitude and the reflected and transmitted amplitude. First, the continuity in displacement at the interface must be fulfilled. Substituting eq. (2.38) and eq. (2.39) into eq. (2.40), yields

$$A^{\mathrm{I}} + A^{\mathrm{R}} = A^{\mathrm{T}}. \tag{2.48}$$

Second, the continuity in stress at the interface must be fulfilled. Substituting eq. (2.46) and eq. (2.46) into eq. (2.41) yields

$$\left(\lambda^{(1)} + 2\mu^{(1)}\right) k^{(1)} \left(A^{\mathrm{I}} - A^{\mathrm{R}}\right) = \left(\lambda^{(2)} + 2\mu^{(2)}\right) k^{(2)} A^{\mathrm{T}}. \tag{2.49}$$

Finally, using that

$$\lambda^{(n)} + 2\mu^{(n)} = \rho^{(n)} [c_{\mathrm{L}}^{(n)}]^2, \quad k^{(n)} = \frac{\omega}{c_{\mathrm{L}}^{(n)}} \quad \text{and} \quad n = 1, 2, \tag{2.50}$$

where n is the medium number, we get the following system:

$$A^{\mathrm{I}} + A^{\mathrm{R}} = A^{\mathrm{T}} \tag{2.51}$$

$$\rho^{(1)} c_{\mathrm{L}}^{(1)} \left(A^{\mathrm{I}} - A^{\mathrm{R}}\right) = \rho^{(2)} c_{\mathrm{L}}^{(2)} A^{\mathrm{T}}. \tag{2.52}$$

Using the definition of acoustic impedance $\rho^{(n)} c_{\mathrm{L}}^{(n)} = Z_n$, and solving the system, gives

$$A^{\mathrm{R}} = \frac{Z_1 - Z_2}{Z_1 + Z_2} \cdot A^{\mathrm{I}}, \tag{2.53}$$

$$A^{\mathrm{T}} = \frac{2Z_1}{Z_1 + Z_2} \cdot A^{\mathrm{I}}. \tag{2.54}$$

The stress reflection and transmission coefficients are obtained as follows:

$$R_\sigma^{12} = \left.\frac{\sigma^{\mathrm{R}}}{\sigma^{\mathrm{I}}}\right|_{x=0} = -\frac{A^{\mathrm{R}}}{A^{\mathrm{I}}} = \frac{Z_2 - Z_1}{Z_1 + Z_2}, \tag{2.55}$$

$$T_\sigma^{12} = \left.\frac{\sigma^{\mathrm{T}}}{\sigma^{\mathrm{I}}}\right|_{x=0} = \frac{\left(\lambda^{(2)} + 2\mu^{(2)}\right) k^{(2)}}{\left(\lambda^{(1)} + 2\mu^{(1)}\right) k^{(1)}} \frac{A^{\mathrm{T}}}{A^{\mathrm{I}}} = \frac{Z_2}{Z_1} \frac{A^{\mathrm{T}}}{A^{\mathrm{I}}} = \frac{2Z_2}{Z_1 + Z_2}, \tag{2.56}$$

where the superscript "12" of the coefficients means that the wave propagates from medium 1 to medium 2. A similar argument for the *velocity field*, $\dot{u}$, provides

$$R_{\dot{u}}^{12} = \left.\frac{\dot{u}^{\mathrm{R}}}{\dot{u}^{\mathrm{I}}}\right|_{x=0} = -\frac{A^{\mathrm{R}}}{A^{\mathrm{I}}} = \frac{Z_2 - Z_1}{Z_1 + Z_2}, \tag{2.57}$$

$$T_{\dot{u}}^{12} = \left.\frac{\dot{u}^{\mathrm{T}}}{\dot{u}^{\mathrm{I}}}\right|_{x=0} = \frac{A^{\mathrm{T}}}{A^{\mathrm{I}}} = \frac{2Z_1}{Z_1 + Z_2}. \tag{2.58}$$

The power flow through a unit area normal to the direction of propagation is defined as the *intensity*, J, of the wave.

$$J = \frac{\partial}{\partial t}\left(\frac{\Phi}{S} u\right) = \frac{\Phi}{S} \dot{u} = \sigma \dot{u}, \tag{2.59}$$

where Φ is a traction force on a surface S. The intensity transmission coefficient, is obtained as

$$T_{\mathrm{J}}^{12} = \left.\frac{J^{\mathrm{T}}}{J^{\mathrm{I}}}\right|_{x=0} = \frac{T_\sigma^{12} T_{\dot{u}}^{12} \sigma^{\mathrm{I}} \dot{u}^{\mathrm{I}}}{\sigma^{\mathrm{I}} \dot{u}^{\mathrm{I}}} = \frac{4Z_1 Z_2}{(Z_1 + Z_2)^2}. \tag{2.60}$$

2.2 Ultrasound Transducer

In this section, we present the layers that constitute the ultrasound transducer and the design criteria to optimize the transmitted intensity. Most of the theory is adapted from [3].

2.2.1 Piezoelectric Element

An *ultrasound transducer* can be made of a plate of piezoelectric material with thin metal electrodes on each surface. If a voltage source is coupled to the electrodes, the PE plate either contracts/expands. If pressure is applied to the PE plate, it generates a voltage between the electrodes. Therefore, the PE plate can function as a coupling between acoustic waves and electrical voltage. When it gets excited by an electric voltage, it will in the same manner as a spring pulled out from its equilibrium, start to vibrate around its original thickness in its resonance frequency (also known as centre frequency), f_0.

If we connect a vibrating PE plate to tissue, it will cause the surface of the tissue to vibrate and therefore radiate a beam of acoustic waves, known as an *ultrasound beam*, into the tissue. Because a PE plate is very stiff, its displacement amplitude is low even though the pressure force might be large. For the soft tissue, a large pressure force would generate a large displacement. The small displacement amplitudes generated by the vibration of the PE plate, does not couple the energy effectively into the soft tissue, because small deformations in the tissue means small pressure forces, and the transmitted intensity is therefore low. This was explained in section 2.1.4, by means of the acoustic impedance.

As can be seen by investigating the coefficient of transmitted intensity in eq. (2.60), T_{J}^{12} can be written as

$$T_{\mathrm{J}}^{12} = 1 - \frac{(Z_1 - Z_2)^2}{(Z_1 + Z_2)^2} = 1 - R_{\mathrm{J}}^{12}, \tag{2.61}$$

and it is obvious that to increase the transmitted intensity, the acoustic impedance of the PE plate and the tissue should be as similar as possible. Because we cannot manipulate the tissue, the acoustic impedance of the PE plate should be decreased. This is done by *dicing* the PE plate into small bars of less than half a wavelength ($\Lambda/2$) in width. The wavelength is defined as

$$\Lambda = \frac{c}{f} \tag{2.62}$$

where c is the sound velocity of the material and f is the frequency. The space between the bars is filled with epoxy, creating a *composite piezoelectric material*. The soft epoxy in-between the bars allows the bars to compress/expand more freely, as there is less straining in transverse direc-

tion. Thus, the expansion/compression imposed by the Poisson's ratio experiences less resistance. Another reason for using the composite PE, is not to reduce the acoustic impedance, but to reduce transverse waves in the PE plate. In the same way as the plate vibrates in the thickness mode, the plate may also vibrate in the transverse direction. In pulse echo measurements, one usually drives the transducer on a wide frequency range, such that resonant modes outside the a $\Lambda/2$ mode can be excited and disturb the ultrasound beam from the transducer. This is usually avoided using composite PE material, because the thin bars will have a single thickness mode of vibration in the frequency range of interest.

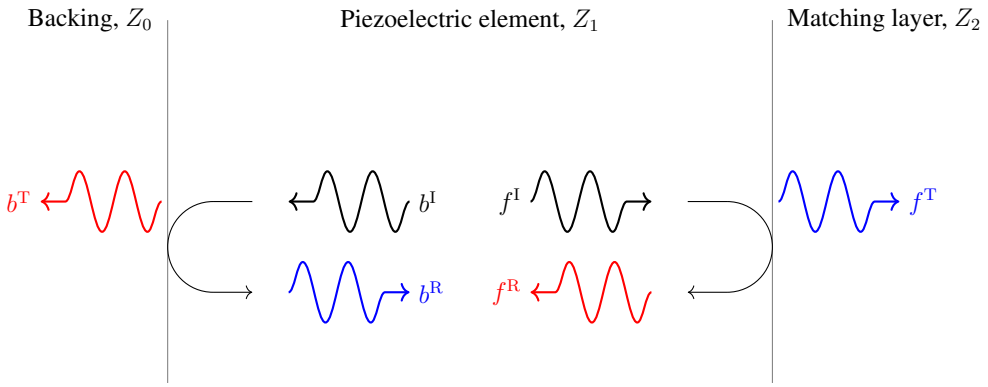

Figure 2.2: The forward and backward propagating waves and their transmitted and reflected waves

When the PE elements are excited, they generate two pressure waves; a forward and a backward propagating wave. At surfaces of the PE elements, there usually is a mismatch in the acoustic impedance. Thus, partly reflecting and transmitting the wave, generating two new waves. The two reflected waves will propagate to the opposite interfaces and again be transmitted and reflected. This back and forth reflection, illustrated in fig. 2.2, is known as *ringing*, and will continue until all the energy is transmitted out. The length of the generated pulse is decided by the *ring down* of the element. A long ring down results in a long pulse and a narrow bandwidth. To reduce the ring down, usually one or multiple *matching layers* are placed between the PE elements and the tissue.

2.2.2 Matching Layers

The matching layer is placed between the piezoelectric element and the load. For a medical ultrasonic transducer, this means between the PE of high impedance(Z_0), and the body tissue of low

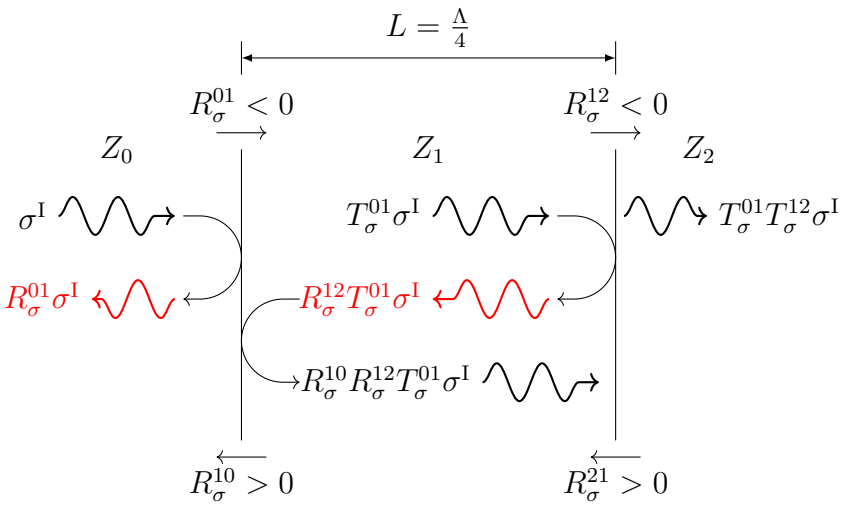

Figure 2.3: When a wave hits an interface, parts of it gets reflected and transmitted equivalent to the transmission and reflection coefficients. The stress reflection coefficient is positive when propagating from a high to a low impedance medium, and negative when propagation from a low to a high impedance medium ($Z_0 > Z_1 > Z_2$).

impedance(Z_2). The ideal impedance of the matching layer is the impedance that maximizes the transmitted intensity.

$$\begin{aligned} J^{\mathrm{T}} = \sigma^{\mathrm{T}}\dot{u}^{\mathrm{T}} &= T_\sigma^{01}T_\sigma^{12}\sigma^{\mathrm{I}} \cdot T_v^{01}T_v^{12}\dot{u}^{\mathrm{I}} \\ &= \frac{2Z_1}{Z_0+Z_1}\frac{2Z_2}{Z_1+Z_2}\sigma^{\mathrm{I}} \cdot \frac{2Z_0}{Z_0+Z_1}\frac{2Z_1}{Z_1+Z_2}\dot{u}^{\mathrm{I}} \\ J^{\mathrm{T}} &= \frac{16Z_1^2Z_2Z_0}{(Z_0+Z_1)^2(Z_1+Z_2)^2}J^{\mathrm{I}} \end{aligned} \tag{2.63}$$

We now have the transmitted intensity, J^{T}, as a function of the variable Z_1. Finding the maximum transmitted intensity by altering the impedance of the matching layer is an optimization problem:

$$\frac{\partial J^{\mathrm{T}}}{\partial Z_1} = 0 \quad \Rightarrow \quad Z_1^2 = Z_0Z_2. \tag{2.64}$$

The ideal thickness is the one that makes forward propagating reflected waves in phase. As illustrated in fig. 2.3 it is the distance needed for the wave $R_{10}R_{12}T_{01}\sigma^{\mathrm{I}}$ and $T_{01}\sigma^{\mathrm{I}}$ to stay in phase as they propagate in to medium 2. First we inspect the phase shifts imposed by the reflection

coefficients. From equation eq. (2.55) we see that

$$R_\sigma^{12} = \frac{Z_2 - Z_1}{Z_1 + Z_2} = \begin{cases} > 0, & \text{if } Z_1 < Z_2 \\ = 0, & \text{if } Z_1 = Z_2 \\ < 0, & \text{if } Z_1 > Z_2 \end{cases} \tag{2.65}$$

if the stress wave propagates from a high to low impedance ($Z_1 > Z_2$), the reflection coefficient is negative, and positive from low to high ($Z_1 < Z_2$). The wave $R_{10}R_{12}T_{01}\sigma^{\mathrm{I}}$ has been reflected twice, where $R_\sigma^{12} < 0$ and $R_\sigma^{10} > 0$. The negative reflection coefficient gives the reflected wave a π phase shift. For the waves to be in phase, we set the exponent in the wave equation equal to zero:

$$kx - \omega t = 0 \quad \Rightarrow \quad k(2L) - \pi = 0, \tag{2.66}$$

where k is the wavenumber and L is the thickness of the matching layer. The distance traveled inside the matching layer is thus equal to $2L$. Using that the wavenumber $k = 2\pi/\Lambda$, we get the ideal thickness of the matching layer to be

$$L = \frac{\Lambda}{4}. \tag{2.67}$$

This is also the case when the wave propagates from the tissue into the transducer. Therefore, a layer with impedance somewhere between the two adjacent layers ($Z_0 \lesseqgtr Z_1 \lesseqgtr Z_2$) has what is known as a $\frac{\Lambda}{4}$ thickness resonance. If the layer has the ideal thickness, it is known as a *quarter-wave impedance transformer*.

2.2.3 Isolation Layer

Theory presented here is taken from [19, 20]. When designing the ultrasound stack used in SURF imaging, the High Frequency transducer is placed in front of the Low Frequency transducer with multiple isolation layers in between. These insulation layers make up the isolation section, which has two functions; preventing propagation from the HF section into the LF section, and serving as

a matching structure for the LF section to the load. The reflection at HF/isolation interface should be as high as possible to avoid backward propagating waves, thus the isolation section should have a very low acoustic impedance. Myhre et al. [20] shows that using an odd number of a $\Lambda/4$ isolation layers is advantageous for achieving a low HF backing impedance, and that odd numbered layers should have a low acoustic impedance and even numbered layers should have a high acoustic impedance. The high impedance layers can be represented by copper, which has a high thermal conductivity and high sound speed. High sound speed means thicker material, as its thickness is decided by its wavelength. The combination of large thickness and high thermal conductivity makes the copper layer suitable as a heat sink in the transducer stack.

2.3 Thermal Conductivity Using ICA

Traditionally, Isotropic Conductive Adhesives are made of an epoxy mixed with metal fillers, usually metal flakes. Silver flakes are the most widely used because of its high conductivity and ease of manufacturing.[9] However, a downside of using silver flakes is the high cost of silver. The amount in $\mathrm{vol}\%$ of silver flakes used in traditional ICA typically range from 20-30 $\mathrm{vol}\%$. Gakkestad et al. [9] have shown that a thermal conductivity of $1\,\mathrm{W\,m^{-1}\,K^{-1}}$ can be achieved by using only $1.4\,\mathrm{vol}\%$ of silver when using metal coated polymer spheres. Achieving the same with silver flakes requires $16\,\mathrm{vol}\%$ silver. This clearly demonstrates the cost benefits of the silver coated polymer spheres. Reducing the amount of silver also has another benefit when used in an ultrasound transducer. Silver has a high acoustic impedance, thus reducing the amount also reduces the acoustic impedance of the ICA, which is important for the isolation layers. Jain et al. [14; 15] has studied how the different geometric properties affect the electrical conductivity, and it is known that the thermal conductivity is proportional to the electrical conductivity (Weidemann-Franz law). We can thus use these results to evaluate how the geometric properties affect the thermal conductivity. Unsurprisingly the conductivity increases with an increase in shell thickness. Gakkestad et al. [9] shows how the same thermal conductivity is obtained with less $\mathrm{vol}\%$ when larger particles are used. They explain the result by saying that the thermal conductivity is dependent on the thermal resistance of the particles and the thermal contact resistance between the particles. Larger particles need fewer contact points

over the same thickness, thus larger particles are advantageous. Jain et al. [15] achieves a better conductivity for the smaller particles, but also argues that the silver is more efficiently used when applied to larger spheres.

2.4 Homogenization of Heterogeneous Material

Theory adapted from Christensen [7]. The developments in the present chapter assume conditions of linear elastic behavior. Further, the individual phases are assumed homogeneous and isotropic.

2.4.1 Representative Volume Element

We assume there exists a characteristic dimension of the inhomogeneity, for example, in a system of spherical inclusions, this could be the radius of spheres or the distance between the spheres. This characteristic dimension is a gross idealization of a necessarily statistical description of the heterogeneous system. For every heterogeneous system, if one increases a length scale long enough, there is a length scale where the heterogeneous properties can be averaged in a meaningful way. Call the length scale of averaging δ. This scale, δ must be of a dimension much larger than the characteristic length of the inhomogeneity. If δ is small compared to the characteristic dimension of the body, we say that the material is macroscopically homogeneous. The material can be idealized as being effectively homogeneous, and problems of mechanical nature can be solved using these average properties associated with the length scale δ.

Now, let us introduce a volume element of the heterogeneous material. If this volume element has a dimension identical to the averaging dimension, δ, it is known as a Representative Volume Element (RVE).

2.4.2 Volumetric Averaging

For an RVE the average stress is defined by

$$\langle \sigma_{ij} \rangle = \frac{1}{V} \int_V \sigma_{ij}\left(x_i\right) \mathrm{d}v, \tag{2.68}$$

and the average strain by

$$\langle \varepsilon_{ij} \rangle = \frac{1}{V} \int_V \varepsilon_{ij}\left(x_i\right) \mathrm{d}v, \tag{2.69}$$

where V designates its volume.

Using the most general form of a linear elastic material defined in eq. (2.2), the effective compliance tensor, designated by C^{eff}_{ijkl} is defined through its presence in the relation

$$\langle \sigma_{ij} \rangle = C^{\mathrm{eff}}_{ijkl} \langle \varepsilon_{kl} \rangle . \tag{2.70}$$

The problem of interest is a two-phase heterogeneous system, where one material is assumed continuous, the matrix, and the other is in the form of discrete inclusions. Both are assumed isotropic, and the stress strain relationship can be expressed using eq. (2.17) for the two materials by

$$\sigma^{\mathrm{M}}_{ij} = \lambda_{\mathrm{M}} \varepsilon^{\mathrm{M}}_{kk} \delta_{ij} + 2\mu_{\mathrm{M}} \varepsilon^{\mathrm{M}}_{ij}, \tag{2.71}$$

for the matrix phase and by

$$\sigma^{\mathrm{I}}_{ij} = \lambda^{\mathrm{I}} \varepsilon^{\mathrm{I}}_{kk} \delta_{ij} + 2\mu^{\mathrm{I}} \varepsilon^{\mathrm{I}}_{ij}, \tag{2.72}$$

for the inclusion phase.

The average stress formulation eq. (2.68) can be written as

$$\langle \sigma_{ij} \rangle = \frac{1}{V} \int_{V - \sum_{n=1}^{N} V_n} \sigma^{\mathrm{M}}_{ij} \mathrm{d}v + \frac{1}{V} \sum_{n=1}^{N} \int_{V_n} \sigma^{\mathrm{I}}_{ij} \mathrm{d}v, \tag{2.73}$$

where there are N inclusions inside the RVE. The first integral designates the matrix region, and the second integral designates the inclusions. By writing out the stress in the first integral using the relation in eq. (2.71), and decomposing it, we get

$$C^{\mathrm{eff}}_{ijkl} \langle \varepsilon_{kl} \rangle = \lambda_{\mathrm{M}} \delta_{ij} \langle \varepsilon_{kk} \rangle + 2\mu_{\mathrm{M}} \langle \varepsilon_{ij} \rangle + \frac{1}{V} \sum_{n=1}^{N} \int_{V_n} \left(\sigma^{\mathrm{I}}_{ij} - \lambda_{\mathrm{M}} \delta_{ij} \varepsilon^{\mathrm{M}}_{kk} - 2\mu_{\mathrm{M}} \varepsilon^{\mathrm{M}}_{ij} \right) \mathrm{d}v. \tag{2.74}$$

We have up till now used superscripts on stresses and strains to describe the material they “operate”

in. The material is represented by the Lamé constants; thus, we drop the superscripts and rewrite eq. (2.74):

$$C^{\text{eff}}_{ijkl} \langle \varepsilon_{kl} \rangle = \lambda_{\text{M}} \delta_{ij} \langle \varepsilon_{kk} \rangle + 2\mu_{\text{M}} \langle \varepsilon_{ij} \rangle + \frac{1}{V} \sum_{n=1}^{N} \int_{V_n} (\sigma_{ij} - \lambda_{\text{M}} \delta_{ij} \varepsilon_{kk} - 2\mu_{\text{M}} \varepsilon_{ij}) \, \mathrm{d}v. \tag{2.75}$$

This formula is of use for derivation of effective properties. The derivations of some of these can be found in [7]. This paper will only present one homogenization scheme for nondilute suspensions, namely the *Three Phase Model*.

2.4.3 Three Phase Model

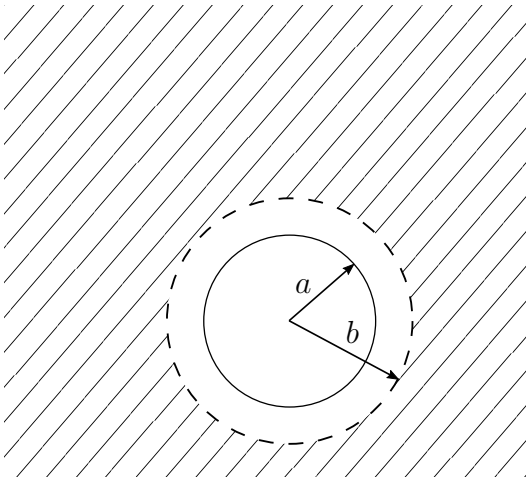

Figure 2.4: The Three Phase Model [7]. The hatched area is the equivalent homogeneous medium.

The Three Phase Model, also known as the Generalized Self Consistent Method, was first introduced by Kerner [16], but has later been criticized for its brevity and assumptions [6]. It is the work of Christensen and Lo [5] that is most precise, and the following theory is therefore adapted from their work. The TPM is used to find the equivalent homogeneous medium of a two-phase composite, comprising spherical inclusions in a continuous matrix. The TPM is composed of one particle surrounded by a layer of matrix in a ratio a/b, and the particle-matrix sphere with radius b is called a composite sphere. This composite particle is embedded in the equivalent homogeneous medium, as shown in fig. 2.4. It requires that the effective medium possesses the same average conditions of stress and strains as the model in fig. 2.4. The objective is to solve for the stiffness

properties of an equivalent homogeneous medium, such that under the same applied displacement conditions, this equivalent homogeneous medium stores the same energy U as the configuration of fig. 2.4. The derivation is left out, but can be found in Christensen and Lo [5]. The effective bulk modulus is found to be

$$\kappa = \kappa_{\mathrm{M}} + \frac{(\kappa_{\mathrm{I}} - \kappa_{\mathrm{M}})\vartheta_{\mathrm{I}}}{1 + (1 - \vartheta_{\mathrm{I}})\left[(\kappa_{\mathrm{I}} - \kappa_{\mathrm{M}})/(\kappa_{\mathrm{M}} + \frac{4}{3}\mu_{\mathrm{M}})\right]}, \tag{2.76}$$

where $\vartheta_{\mathrm{I}} = (a/b)^3$ is the volume fraction of inclusions, subscript I and M denote the inclusion and matrix phase, respectively. The solution for the shear modulus is presented on the same form as in [7]; as the solution of the quadratic equation

$$A\left(\frac{\mu}{\mu_{\mathrm{M}}}\right)^2 + 2B\left(\frac{\mu}{\mu_{\mathrm{M}}}\right) + C = 0, \tag{2.77}$$

where

$$\begin{aligned} A = {} & 8\left(\frac{\mu_{\mathrm{I}}}{\mu_{\mathrm{M}}} - 1\right)(4 - 5\mu_{\mathrm{M}})\eta_1\vartheta_{\mathrm{I}}^{10/3} - 2\left[63\left(\frac{\mu_{\mathrm{I}}}{\mu_{\mathrm{M}}} - 1\right)\eta_2 + 2\eta_1\eta_3\right]\vartheta_{\mathrm{I}}^{7/3} \\ & + 252\left(\frac{\mu_{\mathrm{I}}}{\mu_{\mathrm{M}}} - 1\right)\eta_2\vartheta_{\mathrm{I}}^{5/3} - 50\left(\frac{\mu_{\mathrm{I}}}{\mu_{\mathrm{M}}} - 1\right)(7 - 12\nu_{\mathrm{M}} + 8\nu_{\mathrm{M}}^2)\eta_2\vartheta_{\mathrm{I}} + 4(7 - 10\nu_{\mathrm{M}})\eta_2\eta_3, \end{aligned} \tag{2.78}$$

$$\begin{aligned} B = {} & -2\left(\frac{\mu_{\mathrm{I}}}{\mu_{\mathrm{M}}} - 1\right)(1 - 5\nu_{\mathrm{M}})\eta_1\vartheta_{\mathrm{I}}^{10/3} + 2\left[63\left(\frac{\mu_{\mathrm{I}}}{\mu_{\mathrm{M}}} - 1\right)\eta_2 + 2\eta_1\eta_3\right]\vartheta_{\mathrm{I}}^{7/3} \\ & - 252\left(\frac{\mu_{\mathrm{I}}}{\mu_{\mathrm{M}}} - 1\right)\eta_2\vartheta_{\mathrm{I}}^{5/3} + 75\left(\frac{\mu_{\mathrm{I}}}{\mu_{\mathrm{M}}} - 1\right)(3 - \nu_{\mathrm{M}})\eta_2\nu_{\mathrm{M}}\vartheta_{\mathrm{I}} + \frac{3}{2}(15\nu_{\mathrm{M}} - 7)\eta_2\eta_3, \end{aligned} \tag{2.79}$$

$$\begin{aligned} C = {} & 4\left(\frac{\mu_{\mathrm{I}}}{\mu_{\mathrm{M}}} - 1\right)(5\nu_{\mathrm{M}} - 7)\eta_1\vartheta_{\mathrm{I}}^{10/3} - 2\left[63\left(\frac{\mu_{\mathrm{I}}}{\mu_{\mathrm{M}}} - 1\right)\eta_2 + 2\eta_1\eta_3\right]\vartheta_{\mathrm{I}}^{7/3} \\ & + 252\left(\frac{\mu_{\mathrm{I}}}{\mu_{\mathrm{M}}} - 1\right)\eta_2\vartheta_{\mathrm{I}}^{5/3} + 25\left(\frac{\mu_{\mathrm{I}}}{\mu_{\mathrm{M}}} - 1\right)(\nu_{\mathrm{M}}^2 - 7)\eta_2\vartheta_{\mathrm{I}} - (7 + 5\nu_{\mathrm{M}})\eta_2\eta_3, \end{aligned} \tag{2.80}$$

with

$$\begin{aligned}
\eta_1 &= (49 - 50\nu_{\mathrm{I}}\nu_{\mathrm{M}})\left(\frac{\mu_{\mathrm{I}}}{\mu_{\mathrm{M}}} - 1\right) + 35\frac{\mu_{\mathrm{I}}}{\mu_{\mathrm{M}}}(\nu_{\mathrm{I}} - 2\nu_{\mathrm{M}}) + 35(2\nu_{\mathrm{I}} - \nu_{\mathrm{M}}),\\
\eta_2 &= 5\nu_{\mathrm{I}}\left(\frac{\mu_{\mathrm{I}}}{\mu_{\mathrm{M}}} - 8\right) + 7\left(\frac{\mu_{\mathrm{I}}}{\mu_{\mathrm{M}}} + 4\right),\\
\eta_3 &= \frac{\mu_{\mathrm{I}}}{\mu_{\mathrm{M}}}(8 - 10\nu_{\mathrm{M}}) + (7 - 5\nu_{\mathrm{M}}).
\end{aligned} \tag{2.81}$$

2.5 Finite Element Method

The Finite Element Method is a method for solving partial differential equations of field problems. The field problem is discretized into elements and solved using the boundary conditions and interpolation functions. We assume that the reader is familiar with Finite Element Analysis (FEA). However, some of the theory is presented here. The commercial FEA program Abaqus 6.14-1 by Dassault Systèmes Simulia Corp. is used to for numerical analysis. All the following theory is adapted from [4, 8].

The basic assumption of FEM states that a field variable can be expressed using nodal displacements and interpolation functions, i.e.

$$\mathbf{u} = N\mathbf{d}, \tag{2.82}$$

where $\mathbf{u}$ is the vector containing the displacement field, N is the interpolation functions matrix, and $\mathbf{d}$ is the nodal displacement vector. For problems of time-independent loading, the problem can be approximated by

$$K\mathbf{d} = \mathbf{F}^{\mathbf{ext}}, \tag{2.83}$$

where K is the stiffness matrix and $\mathbf{F}^{\mathbf{ext}}$ is the external loading vector. The stiffness matrix is

$$K = \int_V B^T C B \mathrm{d}v \tag{2.84}$$

where C is the compliance tensor from eq. (2.2) and B is the strain-displacement matrix. The

strain-displacement matrix, B, is related to N in the same way as ε is related to $\mathbf{u}$:

$$\varepsilon = \Delta \mathbf{u}, \tag{2.85}$$

$$B = \Delta N, \tag{2.86}$$

where Δ is an operator matrix dependent on the problem we are solving. Because we will approximate our model using axisymmetric approximation, Δ will take a specific form and will be presented in section 2.5.1. The shape function N is decided by what type of elements we choose to use.

The integral in eq. (2.84) is solved by Gauss quadrature. When specifying elements in ABAQUS, one can choose to use full integration or reduced integration elements. *Full integration* is defined as the quadrature rule with the lowest order that *exactly* integrates the stiffness matrix. It may lead to an over stiff solution, due to the assumed displacement field. The real solution will always be displaced in the displacement field that requires the least energy. *Reduced integration* is the integration rule of one order lower than the full integration. Using reduced integration has its benefits; it reduces computational time, but it may also improve the accuracy of the FE result, because it "softens" the too stiff estimate. However, reduced integration may lead to *spurious energy modes*; deformation modes that does not absorb energy. A remedy is to use enhanced hourglass control in ABAQUS.

2.5.1 Axisymmetric Stress and Strains

If a solid can be generated by revolving a plane figure about an axis in space, it is axisymmetric. It is best described using the cylindrical coordinates r, θ and z, as is illustrated in fig. 2.5. If the loading is axisymmetric as well, we can assume

$$u_\theta = 0 \quad \text{and} \quad \sigma_{r\theta} = \sigma_{\theta z} = \varepsilon_{r\theta} = \varepsilon_{\theta_z} = 0. \tag{2.87}$$

Because we can remove the two shear stresses and strains, the stress and strain vectors are reduced from six to four components, and a problem that used to be three-dimensional is now for an arbitrary

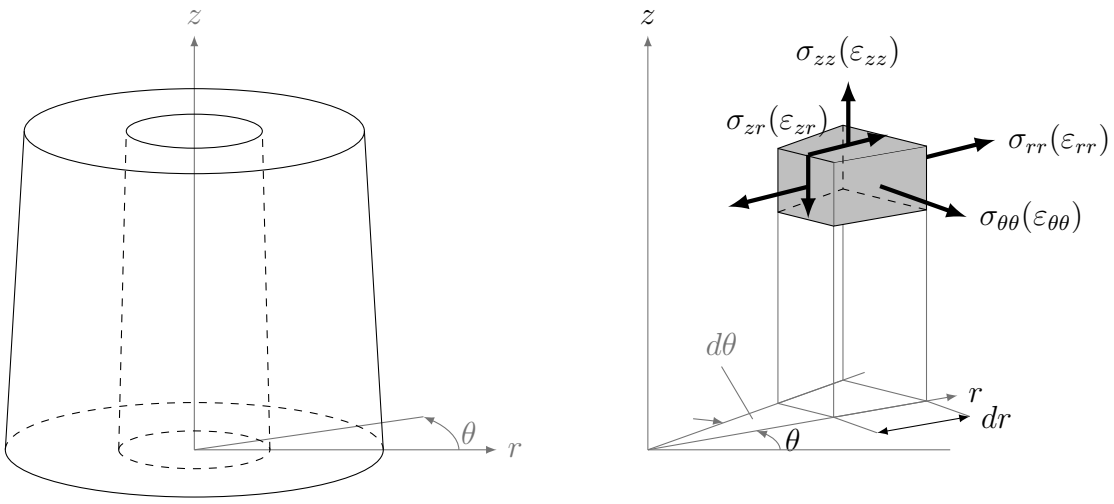

Figure 2.5: Axisymmetric stress and strains [4]

value of θ, reduced to two dimensions. The stresses and strains for an axisymmetric volume element can be seen in fig. 2.5 and the strain vector is

$$\boldsymbol{\varepsilon} = \begin{bmatrix} \varepsilon_{rr} \\ \varepsilon_{\theta\theta} \\ \varepsilon_{zz} \\ 2\varepsilon_{zr} \end{bmatrix} = \begin{bmatrix} \frac{\partial}{\partial r} & 0 \\ \frac{1}{r} & 0 \\ 0 & \frac{\partial}{\partial z} \\ \frac{\partial}{\partial z} & \frac{\partial}{\partial r} \end{bmatrix} \begin{bmatrix} u_r \\ u_z \end{bmatrix} = \Delta \mathbf{u} \tag{2.88}$$

where Δ is the same operator as in eq. (2.86).

2.5.2 Explicit Method

The theory is adapted from [1, 8]. We are in this thesis going to solve a time dependent problem, thus we must solve the dynamic equilibrium equation, which is approximated with a set of ordinary differential equations (ODE) in time:

$$M\ddot{\mathbf{d}} + G\dot{\mathbf{d}} + K\mathbf{d} = \mathbf{F}^{\mathbf{ext}}, \tag{2.89}$$

where M is the *mass matrix*, G is the *damping matrix*, and K and $\mathbf{F}^{\mathbf{ext}}$ are the stiffness matrix and external load vector as before.

To model wave propagation in our FE model, we must solve the dynamic differential equation using the direct integration explicit method. ABAQUS/Explicit solves the dynamic equilibrium equation with the velocity lagging by half a time step

$$M\ddot{\mathbf{d}}_n + G\dot{\mathbf{d}}_{n-\frac{1}{2}} + K\mathbf{d}_n = \mathbf{F}_n^{\mathbf{ext}}, \tag{2.90}$$

and approximates the velocities and accelerations by the half step central differences

$$\dot{\mathbf{d}}_{n+\frac{1}{2}} = \frac{1}{\Delta t}\left(\mathbf{d}_{n+1} - \mathbf{d}_n\right), \tag{2.91}$$

$$\dot{\mathbf{d}}_{n-\frac{1}{2}} = \frac{1}{\Delta t}\left(\mathbf{d}_n - \mathbf{d}_{n-1}\right), \tag{2.92}$$

$$\ddot{\mathbf{d}}_n = \frac{1}{\Delta t^2}\left(\mathbf{d}_{n+1} - 2\mathbf{d}_n + \mathbf{d}_{n-1}\right), \tag{2.93}$$

where the subscript "n" signifies that the variable is evaluated at time step t_n. Substituting eqs. (2.92) and (2.93) into eq. (2.90) and solving for $\mathbf{d}_{n+1}$ yields

$$\frac{1}{\Delta t^2}M\mathbf{d}_{n+1} = \mathbf{F}_n^{\mathbf{ext}} + \left(\frac{2}{\Delta t^2}M - \frac{1}{\Delta t}G - K\right)\mathbf{d}_n - \left(\frac{1}{\Delta t^2}M - \frac{1}{\Delta t}G\right)\mathbf{d}_{n-1}. \tag{2.94}$$

ABAQUS/Explicit uses diagonal (lumped) mass matrix, thus there is no equation solving necessary to find $\mathbf{d}_{n+1}$, and every time step has a low computational cost. Lumped mass matrix together with the central difference method will also be more accurate, because the central difference method gives a period contraction, while the diagonal mass matrix gives a period elongation. Further explanation can be found in [8].

Explicit methods are conditionally stable, which means that there is a *critical time step* Δt_{cr} that must not be exceeded. If it does, the numerical process will "blow up" and become unstable. The critical time step, Δt_{cr}, is

$$\Delta t_{\mathrm{cr}} \leq \frac{L^{\mathrm{elem}}}{c_{\mathrm{L}}}, \tag{2.95}$$

where L^{elem} is the characteristic length of the smallest element and c_{L} is the longitudinal wave velocity of the material. Equation (2.95) is known as the *CFL-condition* after Courant, Friedrichs, and Lewy. It can be interpreted that Δt_{cr} must be small enough that information does not propagate

more than the distance between adjacent nodes during one time step.

In ABAQUS/Explicit it is possible for the user to decide the increment size or use the automatic time incrementation method. The automatic time incrementation requires no user intervention, and can be based on a global or element-by-element estimation [1]. The global estimation is not used when there are infinite elements included in the model. We will in our simulations use the infinite elements to damp out reflections, which we will discuss in more detail in sections 2.5.3 and 3.2. We will therefore use the automatic time incrementation which compute the stable time increment using the CFL-condition element-by-element. The automatic time incrementation method is convenient in our case, because our models have many variations in design that alter the minimum sized elements, materials used and so on. It would therefore be cumbersome to decide the time increment ourselves of every model.

2.5.3 Infinite Elements

The theory is adapted from [1]. *Infinite elements* can be used for problems in which the region of interest is small compared to the surrounding medium. It is particularly of concern in dynamic analysis, when the boundary of the mesh may reflect energy back into the region being modeled. If only finite elements are used, the mesh should be extended to a far distance from the region of interest, so that the influence of the boundaries is considered small enough to be neglected. This approach can be very inefficient since a great number of elements are used outside the area of interest. A better approach is to use infinite elements: elements defined over semi-infinite domains with suitably chosen decay functions.

The dynamic response of the infinite elements is based on the consideration of plane waves propagating normal to the boundary. Let us consider a wave propagating along the x_1-axis. The approach is similar for waves along the x_2- and x_3-axis. First, we introduce distributed damping on

the boundary between the finite and infinite elements, such that

$$\sigma_{11} = -\alpha_{\mathrm{L}} \dot{u}_1, \tag{2.96}$$

$$\sigma_{12} = -\alpha_{\mathrm{T}} \dot{u}_2, \tag{2.97}$$

$$\sigma_{13} = -\alpha_{\mathrm{T}} \dot{u}_3, \tag{2.98}$$

where the dampening constants α_{L} and α_{T} are to be chosen to avoid reflections of the longitudinal and transverse wave energy back into the finite region. Rewriting the equations for an incident and reflected plane displacement wave

$$u^{\mathrm{I}} = A^{\mathrm{I}} e^{i(k^{(1)}x - \omega t)}, \tag{2.35}$$

$$u^{\mathrm{R}} = A^{\mathrm{R}} e^{-i(k^{(1)}x + \omega t)}. \tag{2.36}$$

The normal stress, σ_{11}, in the finite region is equal to eq. (2.46). Expressing σ_{11} using u^{I} and u^{R}, yields

$$\sigma_{11} = (\lambda + 2\mu)\, ik \left(u^{\mathrm{I}} - u^{\mathrm{R}}\right). \tag{2.99}$$

The displacement field in the finite region is $u = u^{\mathrm{I}} + u^{\mathrm{R}}$, making

$$\dot{u} = -i\omega \left(u^{\mathrm{I}} + u^{\mathrm{R}}\right). \tag{2.100}$$

Substituting eqs. (2.99) and (2.100) into eq. (2.96), yields

$$(\lambda + 2\mu - c_{\mathrm{L}}\alpha_{\mathrm{L}})u^{\mathrm{I}} - (\lambda + 2\mu + c_{\mathrm{L}}\alpha_{\mathrm{L}})u^{\mathrm{R}} = 0, \tag{2.101}$$

where it has been used that $c_{\mathrm{L}} = \omega/k$. To damp out reflections, we can ensure that the displacement field is not reflected by setting $u^{\mathrm{R}} = 0$. Then for any arbitrary u^{I}, we get

$$\alpha_{\mathrm{L}} = \frac{\lambda + 2\mu}{c_{\mathrm{L}}} = \rho c_{\mathrm{L}} = Z_{\mathrm{L}}. \tag{2.102}$$

A similar argument for shear waves provides

$$\alpha_{\mathrm{T}} = \rho c_{\mathrm{T}} = Z_{\mathrm{T}}. \tag{2.103}$$

From the above discussion, we see that the infinite elements will damp out all reflections if the material behavior close to the boundary is linear elastic and that the incident waves are plane and normal to the boundary. These boundaries work quite well even in cases that involve non-plane body waves that do not impinge normal on the boundary, provided that they are arranged so that the dominant direction of wave propagation is normal to the boundary.[1]

Chapter 3

Finite Element Approximation of a Composite Material

We will use the commercial Finite Element Analysis program Abaqus 6.14-1 by Dassault Systèmes Simulia Corp. to do FEA. All the Finite Element models are made from python scripts developed by the author. Python is a general-purpose programming language, and ABAQUS can read the scripts and generate the FE models, run simulations and operate on the outputs. Creating models using scripts is of great convenience when doing numerical experiments in design, because of the great number of different models needed. All the analyses are using the functions in `myUtilites.py` to generate models, and depending on the different design variables of interest, different for-loops are created. An example is found in the file `CreateModel_Comparison.py`. It is the actual script used to approximate the results in section 4.1, and shows the convenience of creating basic functions that can be run using different types of loops. All the data in the following chapter are extracted from ABAQUS and post processed in MATLAB as explained in sections 3.6 and 3.7. The models will be used to numerically approximate the effective acoustic impedance of a heterogeneous material comprising silver coated, mono-disperse polymer spheres in a polymer adhesive. The material is manufactured by Conpart AS, and is supposed to transfer heat in an ultrasound transducer while being the isolation and matching layers [19]. Because we want the material to be an Isotropic Conductive Adhesive, the volume fraction of spheres must be above the percolation limit, which Conpart AS has found to be approximately $40\ \mathrm{vol}\%$. We must limit our model in order

to verify its acceptability, so that we can use it for numerical experiments in design. Based on previous composite samples and the interest of this thesis, we have narrowed the geometric parameters to be inside the following range:

$$R = 5 - 15\,\mu\mathrm{m}, \tag{3.1}$$

$$\eta = 100 - 230\,\mathrm{nm}, \tag{3.2}$$

$$\vartheta_p = 45 - 55\%, \tag{3.3}$$

where R is the radius of the core, η is the shell thickness and ϑ_p is the volume fraction of particles. Our FE model must be able to represent the material we want to simulate; thus, we need to create a representative volume element.

The speed of sound in a material varies with frequency and it is therefore necessary to calculate acoustic impedance at the frequency range of interest. In section 3.11 we present material samples and their measured acoustic impedance. We want to compare our approximations with these results, and should therefore use the same centre frequency when defining the pressure pulse used in our FE models. The pressure pulse is presented in section 3.4. As there is no direct way of extracting the acoustic impedance of the composite in ABAQUS, we need to measure the longitudinal velocity of the composite. To do so, we create a FE model that simulates a stress wave propagating through the composite, induced by a pressure pulse applied to the surface. This pressure pulse will then simulate the pressure a transducer layer would be exposed to, when it is attached to excited PE elements. From the simulations, we may estimate the transit time of the pressure wave from the top to bottom of the FE model, and knowing the distance traveled, the bulk velocity and acoustic impedance of the material can be calculated using the relation

$$c_{\mathrm{L}} = \frac{\Delta d}{\Delta t} \tag{3.4}$$

where Δd is the distance between two points of measure and Δt is the time delay. We will measure the stress at the top and bottom of our RVE. The transit time of the pressure wave will be found by using cross-correlation of the pressure in the top elements and the pressure in the bottom elements, and is further explained in section 3.6. In the real composite the particles are randomly dispersed in

the matrix, as they are mixed into the adhesive. Random packing of spheres is a major topic beyond the scope of this thesis, we hence introduce some simplifications: The physical three-dimensional problem is assumed to be axisymmetric, reducing it to a two-dimensional problem, but also limiting it to an ordered system of spheres. The axisymmetric approximation is illustrated in fig. 3.5. The spheres must be stacked on top of each other in a straight line, because a sphere with centre outside the axis of revolution would result in a torus, not a sphere. From inspections of the composite [21], one has seen that not only are the spheres in contact, they even "solder" together during curing of the adhesive, as shown by fig. 3.1. The contact zone varies proportionally with the thickness of the silver layer, and has a length of $\sim 1\,\mu\mathrm{m}$ for the thickest silver coating. If we assume the contact area to be circular, it is unlikely that one cuts straight through the centre of the circular contact area. The contact area in fig. 3.1 might therefore seem smaller than it actually might be.

Two different FE models will be used; the ordered and random axisymmetric model. The ordered model is a highly ordered axisymmetric model, where all the spheres are evenly spaced. The random model allows spheres to be in direct contact in the z-direction. We call it the random model because the number of spheres that are in contact (creating chains) in our model can be decided randomly. The idea, which we explore in sections 3.10.1 to 3.10.3, is that a model where all the spheres are connected and a model where no spheres are connected may act as bounds for the distribution of all the random models.

For convenience, the constituents are assumed *linear elastic* and *isotropic*. It is further assumed *perfect bonding* between the core and shell, and shell and matrix. This means neglecting any loss due to viscous effects in the viscoelastic polymers, as well as loss due to friction between the constituents.

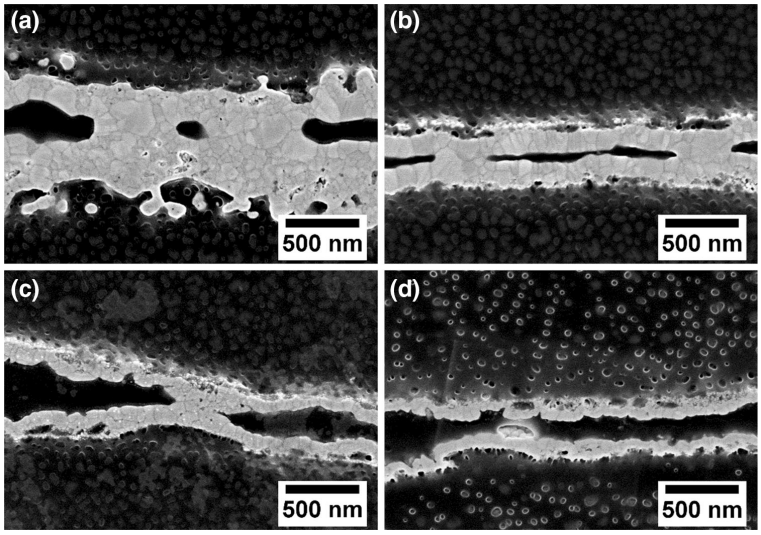

Figure 3.1: Representative cross-sections of contact zones between two particles of radius $15\,\mu\mathrm{m}$ with shell thickness varying from $270\,\mathrm{nm}$ Ag (a), $150\,\mathrm{nm}$ Ag (b), $100\,\mathrm{nm}$ Ag (c), and $60\,\mathrm{nm}$ Ag (d). In the three thickest coatings, the metallurgic connections were observable in the contact zones. For the $60\,\mathrm{nm}$ Ag no such continuous contacts were observed [21].

3.1 Unit Cells

When we create the FE models, we must make sure it is possible to change the radius of the core, R, the shell thickness, η, the volume fraction of particles, ϑ_p, and the number of spheres, N. We therefore introduce what we call our *unit cells*. They will act as building blocks for our RVEs, as the RVEs will be built by stacking unit cells on top of each other. Because we are creating two types of FE models, we also need two types of unit cells; one for the ordered system and a second for the random system. The unit cells are illustrated in fig. 3.2. When we create the *ordered unit cell*, we want a sphere to have the same distance to the spheres above and below, as to the adjacent spheres in the horizontal plane, thus the height, i.e.

$$h = 2w \tag{3.5}$$

where w is the width of the cell, and is found by considering the volume fraction of particles in the adhesive. First by using the volume of a sphere and a cylinder

$$V_{sphere} = \frac{4}{3}\pi(R+\eta)^3, \quad V_{cell} = 2w(\pi w^2) \tag{3.6}$$

and substituting them into the volume fraction, we get an expression for the width of the unit cell

$$\vartheta_p = \frac{V_{sphere}}{V_{cell}} \quad \Leftrightarrow \quad w = \sqrt[3]{\frac{2}{3\vartheta_p}}\,(R+\eta)\,. \tag{3.7}$$

Now, when we create the *random unit cell*, we base it on the design of the ordered unit cell. In that way, we have full control of both the volume fraction and the width of the model, regardless of the length of a chain of spheres in contact. Because of the possibility of sphere contact, the ordered unit cell must be split into two new ones; one that just includes the sphere, and a second that includes the cutoff (adhesive). These two cells together constitute the random unit cell. The splitting of the ordered unit cell is illustrated by dashed red lines in fig. 3.2a. These two cells can then be stacked separately, as spheres are connected.

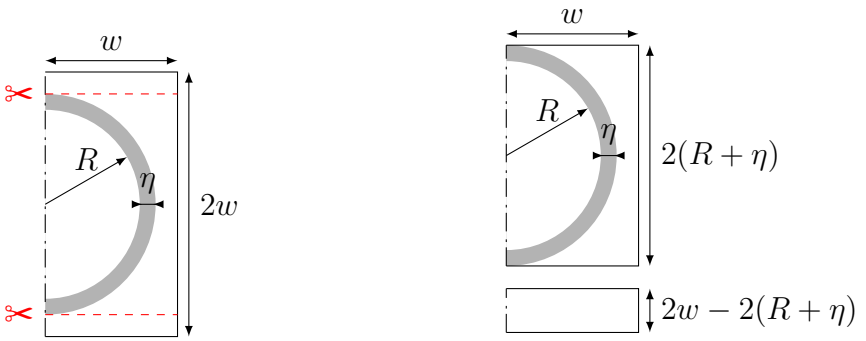

(a) the ordered unit cell **(b)** the random unit cell

Figure 3.2: The ordered and the random unit cell. The red dashed lines drawn on the ordered unit cell is where the cell is split to create the two cells that constitute the random unit cell; one of pure matrix and the other of the composite.

Whenever cells are in contact, their shells will merge together as shown in fig. 3.3. A bottom sphere will only have this contact zone on top, where it is connected to another sphere. In the same way, a top sphere is only connected at the bottom and middle spheres are connected on both top and bottom. Note that the contact width, is the length of the radius of the contact zone, due to the axisymmetry. Now as the building blocks of the RVEs are clearly defined, we need to decide how many unit cells (or particles) we need to include in our FE model for it to be a RVE. This topic will be addressed in section 3.10, where we do a convergence study of the longitudinal velocity with respect to number of particles included in the model.

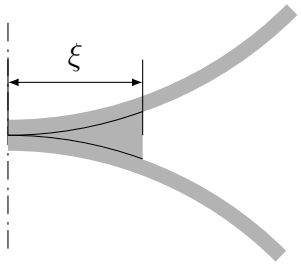

Figure 3.3: The contact zone between two particles. The radius of the contact zone is denoted ξ.

3.2 Boundary Conditions and Infinite Elements

Before we can run any simulations, we need to define our boundary conditions. The material is supposed to be a matching/isolation layer inside an ultrasound transducer. From eq. (2.67) we know that the thickness of the matching/isolation layer is a $\Lambda/4$. Typical lateral dimensions of ultrasound transducers are 15-25 mm in diameter [3], which is around $30-50\Lambda$. We can therefore start by assuming infinite extent in the x- and y-direction. We then idealize the material as an array of space filling hexagonal columns, and approximate each column by an axisymmetric cylinder, as seen in fig. 3.5. The height of the model is decided by a convergence study in section 3.10. A pressure pulse will be evenly distributed on the top boundary, DC, in fig. 3.4. The stress will be measured on the bottom boundary, AB, and the z-axis is the axis of revolution. Due to the assumed infinite extent in x and y direction, the displacement in the r-direction is zero. This is because any adjacent RVE will be exposed to the exact same force and have the exact same deformation, creating a balance in forces in the radial direction at the BC boundary. To avoid any reflections of the propagating stress at the bottom boundary, the adhesive is assumed to extend infinitely in the negative z-direction at AB boundary. Instead of creating a

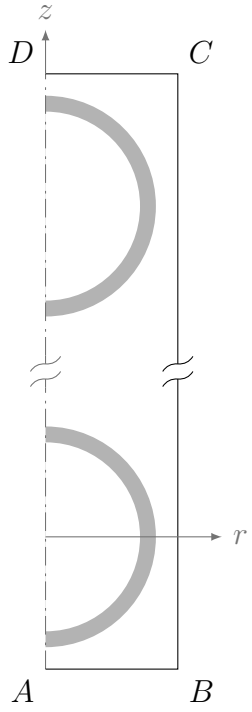

Figure 3.4: The model is compressed in the z-direction, and shows the top and bottom sphere. The spheres in-between are left out.

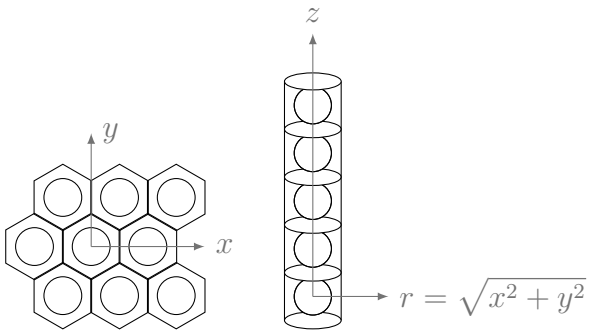

Figure 3.5: The composite is first idealized as an array of space filling hexagonal columns, and then each column is approximated by an axisymmetric cylinder consisting of the particles in adhesive.

model that extends long enough for the reflections not to be an issue, ABAQUS has what is known as infinite elements. These are elements that dampen out all the energy entering, cancelling out any reflected stress, as described in section 2.5.3. Having total reflection on the other boundaries is necessary, as these reflections will capture the stress waves from adjacent spheres, as illustrated in fig. 3.6.

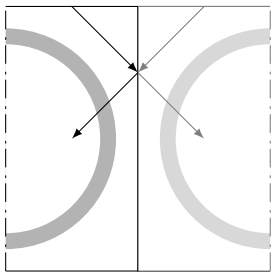

Figure 3.6: The arrows demonstrate stress waves reflected at the boundary. The lighter arrows are those propagating in an adjacent RVE. If the boundary was not there, stress propagating from the adjacent RVE would coincide with the reflected stress. Thus, full reflection at the boundary is necessary to capture stress waves propagating from adjacent RVEs.

3.3 Choice of Elements

When applied to a dynamic analysis, higher-order elements tend to produce noise when stress waves move across a FE mesh. [8] We will therefore avoid higher-order elements in our analysis. It should be mentioned that ABAQUS/Explicit only allows higher-order *triangular* elements. All elements will use reduced integration, and the quadrilateral elements will use *enhanced* hourglass

control as a remedy for spurious energy modes. Triangular elements do not have any such modes. The elements used are

shell: CAX4R (quadrilateral 4-noded axisymmetric element with reduced integration),

core/matrix: CAX3 (triangular 3-noded axisymmetric element).

3.4 The Pressure Pulse

In ABAQUS the user specifies a pressure force using a *magnitude*, P_{mag} and an *amplitude*, $P_{\mathrm{amp}}(t)$. The magnitude is a constant that is multiplied with a time dependent amplitude. We will use a magnitude of $1000\,\mathrm{g\,m^{-6}\,s^{-2}}$, which corresponds to $1\,\mathrm{MPa}$:

$$P_{\mathrm{mag}} = 1\,\mathrm{MPa}. \tag{3.8}$$

The amplitude is designed to be similar to the pulse used to measure sound velocity of material samples in section 3.11, and is the convolution of a sine function of the specified centre frequency, f_0 and a square cosine window, as follows

$$P_{\mathrm{amp}}(t) = \begin{cases} \sin(2\pi f_0 t) \cdot \cos^2\left(2\pi f_0 \frac{t-t_0}{n}\right) & \text{for } t \in [0, 2t_0], \\ 0 & \text{elsewhere}, \end{cases} \tag{3.9}$$

where t_0 is the time shift of the cosine function and n is the number of half sines included in the pulse. The pressure pulse, $P(t)$, is the product of the magnitude and amplitude, i.e.:

$$P(t) = P_{\mathrm{mag}} \cdot P_{\mathrm{amp}}(t). \tag{3.10}$$

We want a short pulse with centre frequency;

$$f_0 = 5\,\mathrm{MHz}. \tag{3.11}$$

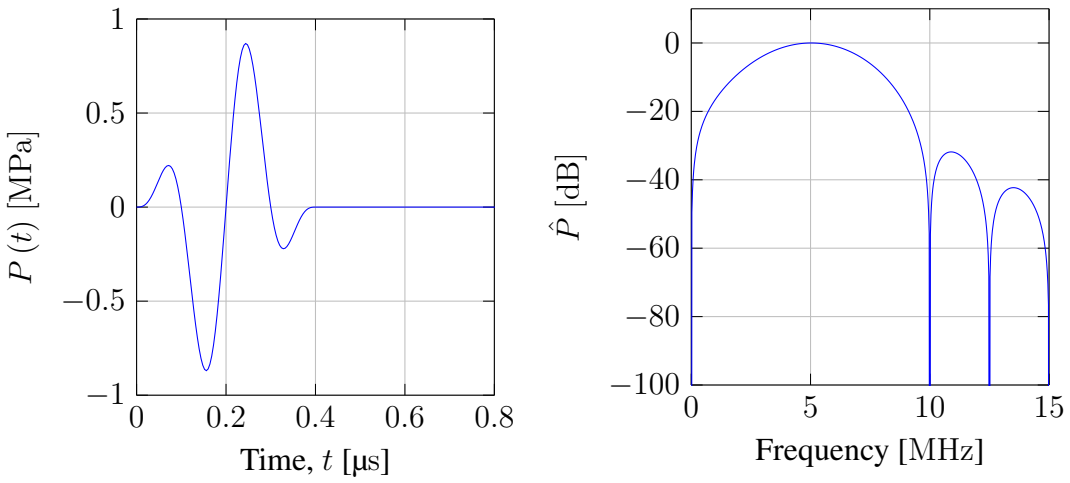

(a) The pressure pulse in the time domain. It has a maximum less than $1\,\mathrm{MPa}$

(b) The normalized pressure pulse in the frequency domain.

Figure 3.7: The pulse multiplied with its $1\,\mathrm{MPa}$ magnitude, and used as a pressure force in ABAQUS.

We therefore decide to include four half sines, $n = 4$, as this short pulse would have a broad bandwidth similar to the one used for the experiment, but still long enough so that its centre frequency is well defined. The time displacement of the cosine window, t_0, can then be found to be

$$2\pi f_0 t_0 = \frac{n\pi}{2} \Rightarrow t_0 = \frac{n}{4f_0} \tag{3.12}$$

The pressure pulse and its frequency spectrum is plotted in fig. 3.7, and it obvious that there is a distinct centre frequency at $5\,\mathrm{MHz}$.

3.5 Materials

The materials used in ABAQUS are summarized in table 3.1. The densities of all the materials except silver was provided by Conpart AS, and found in table 3.1, column ρ_{CP}. Conpart did not have any information on the other mechanical properties, and the necessary properties are therefore taken from the literature. We will use the density provided by Conpart in ABAQUS, and the density from the literature is just there as a tool of comparison. The exception is of course silver, where the density given in the literature is the one that will be used.

Table 3.1: Material parameters used in the FE models. The velocity is calculated using the density given by Conpart AS.

	λ [GPa]	μ [GPa]	E [GPa]	ν	ρ [g cm^{-3}]	ρ_{CP} [g cm^{-3}]	c_{L} [m s^{-1}]
Silver [18]	78.9	27.8	76.0	0.37	10.49	-	3580
PMMA [2]	4.37	2.00	5.37	0.343	1.175	1.16	2686
Epoxy (3012) [2]	4.44	1.59	4.35	0.368	1.18	1.12	2608
Polystyrene (PS) [2]	3.21	1.27	3.45	0.358	1.053	1.05	2340

3.6 Time Delay Estimation

Classical Time Delay Estimation (TDE) techniques consists of identifying the maximum value of the cross-correlation between a reference and a delayed signal. In our case, we use the stress in the top elements as the reference signal, and the stress in the bottom elements as the delayed signal. The approximated cross-correlation, $\hat{R}^{\mathrm{XC}}$, and time delay, $\hat{D}^{\mathrm{XC}}$, for discrete signals can be estimated using direct correlation:

$$\hat{R}^{\mathrm{XC}}(\tau) = \frac{1}{M}\sum_{m=1}^{M} x(mT)\, y(mT+\tau), \tag{3.13}$$

$$\hat{D}^{\mathrm{XC}} = \operatorname{argmax}\left\{\hat{R}^{\mathrm{XC}}(\tau)\right\}, \tag{3.14}$$

where T is the time step, m specifies an index in the signal vector, $(M-1)T$ is the estimation window width and τ is the shifted time lag. We will use the MATLAB-function `xcorr(x,y)` to find the approximated cross correlation between the delayed signal `x` and lagged copies of the reference signal `y` as a function of the lag. Because these are discrete signals, our cross-correlation accuracy is limited by the resolution of our signals. The actual maximum of the cross-correlation is most likely found somewhere between sampling points; thus, interpolation is necessary. We follow the procedure of Jacovitti and Scarano [13], which suggest that the correlation function can be approximated by a convex parabola in the neighbourhood of its maximum, i.e.:

$$\hat{R}^{\mathrm{XC}}(\tau) = a\tau^2 + b\tau + c \tag{3.15}$$

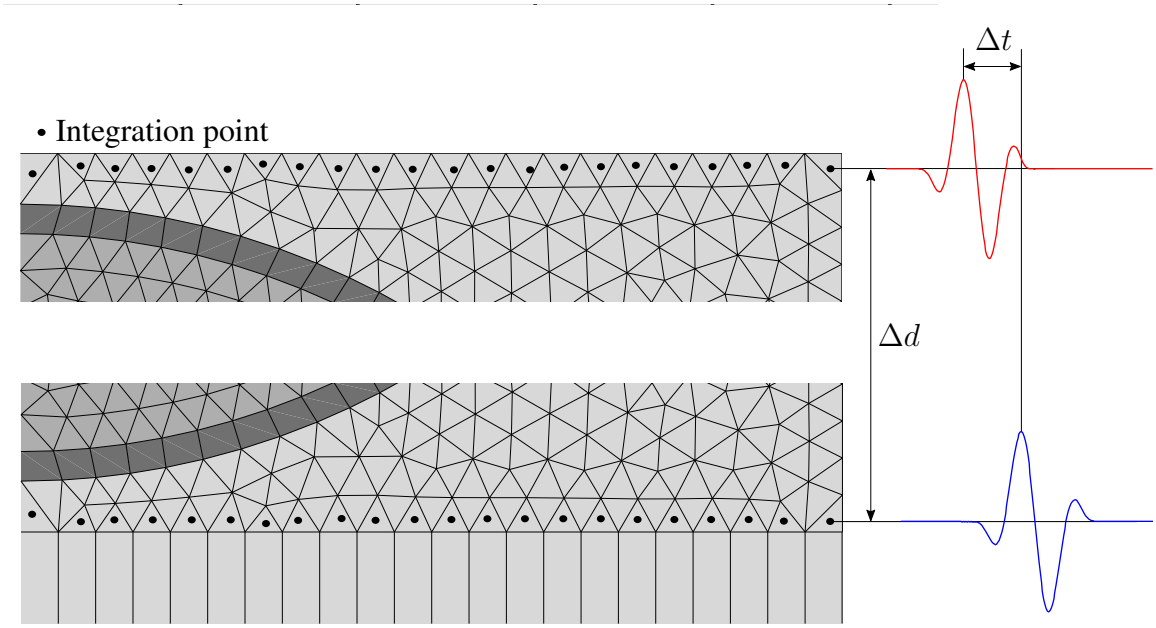

Figure 3.8: Because of the size of the model, only the very top and bottom is included. The stresses are measured in the integration points in the top and bottom elements, and the time delay is approximated as the shift between the pulses. The light grey triangles represent the matrix elements, the dark grey squares represent the shell elements and grey triangles represent the core elements. The infinite elements are the vertically aligned squares at the bottom.

where a, b and c are parameters fitting the measured correlation. Using eq. (3.14) yields

$$\hat{D}^{\mathrm{XC}} = -\frac{b}{2a}. \tag{3.16}$$

Let l_m represent the lag that maximizes $\hat{R}^{\mathrm{XC}}$ in eq. (3.13) before interpolation, and T be the time steps, so that $\hat{R}_m^{\mathrm{XC}}(l_m T)$ represent the maximum of the discrete correlation obtained by using the `xcorr`-function in MATLAB. If we use the two adjacent points, $\hat{R}_{m-1}^{\mathrm{XC}}$ and $\hat{R}_{m+1}^{\mathrm{XC}}$, we can solve eq. (3.16) into the following parabolic interpolation:

$$\hat{D}^{\mathrm{XC}} = \left[\frac{\hat{R}_{m-1}^{\mathrm{XC}} - \hat{R}_{m+1}^{\mathrm{XC}}}{2\left(\hat{R}_{m+1}^{\mathrm{XC}} - 2\hat{R}_m^{\mathrm{XC}} + \hat{R}_{m+1}^{\mathrm{XC}}\right)} + l_m \right] \cdot T. \tag{3.17}$$

In ABAQUS we can specify the sampling frequency by specifying the number of samples for the total time period. Unfortunately, these time steps are not necessarily equally sized. The cross-correlation returns the lag (number of time steps) needed to give the best match between the reference and the delayed signal. If these steps vary in length, multiplying the lag with one specific time step would most certainly lead to a wrong result. Thus, uniform time steps are necessary and we re-sample all the data in MATLAB.

To optimize the TDE, we can filter the stresses in the top and the bottom elements, so that the bottom stresses resemble the top stresses as much as possible. In that way, we remove any trailing vibrations in the bottom stress. If they are not removed, these might shift the cross-correlation later in time, resulting in an incorrect transit time of the stress wave. We therefore manipulate the stress to filter out vibrations by using a *Tukey window*, as shown in fig. 3.9. The length of the unfiltered zone is set by the pulse length, so that it only manipulates the trailing vibrations.

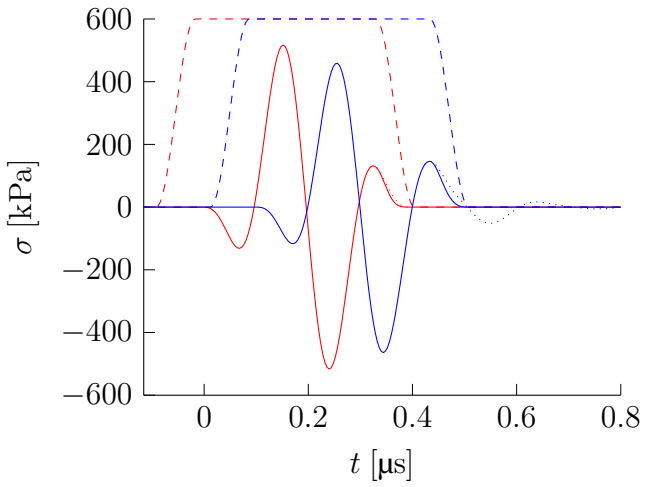

Figure 3.9: Red and blue curves correspond to the filtered normal stresses in the z-direction at top and bottom element, respectively. The dashed lines are the corresponding Tukey windows and the dotted lines are the unfiltered stresses. We clearly see the trailing vibrations and how they are eliminated using the Tukey window.

3.7 Velocity Estimation

The velocity of the composite can be estimated by using eq. (3.4), by assuming constant velocity. The time delay has been estimated by using the cross-correlation as explained in the previous section. We now need to find the distance between the points of measure to be able to approximate the velocity. First, what needs to be considered is that the stresses are measured in the *integration points* of the elements. Because we have chosen to use reduced integration elements, there is only one integration point per element, located in its centre, as shown in fig. 3.10.

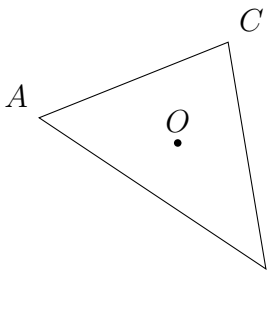

$$O_x = \frac{A_x + B_x + C_x}{3}, \tag{3.18}$$

$$O_y = \frac{A_y + B_y + C_y}{3}. \tag{3.19}$$

Figure 3.10: The location of the integration point, O, of a triangle element with reduced integration.

When the integration points are located, we can easily find the distance between the top and bottom

elements. Utilizing the fact that there is an equal number of elements along the top and bottom edges of supposedly same size, we can expect that every bottom element has a belonging top element located at the same position in the radial direction. The stresses in these opposite elements are used to estimate the time delay, and we therefore also measure the distance between the integration point of these opposite elements, as illustrated in fig. 3.8. We can then use eq. (3.4) to calculate the average constant velocity of the column of composite material between these two elements. Figure 3.11 shows the approximated velocity profile of the composite with two different core material, which tells us that they vary differently depending on the core material. The model with polystyrene as core material has a much lower velocity close to its centre, than the model with PMMA as the core material. This is no surprise, as the velocity in polystyrene is lower than the velocity in PMMA. What is more surprising is that the difference is larger when we use PMMA as the core, even though it has a velocity much closer to that of the epoxy.

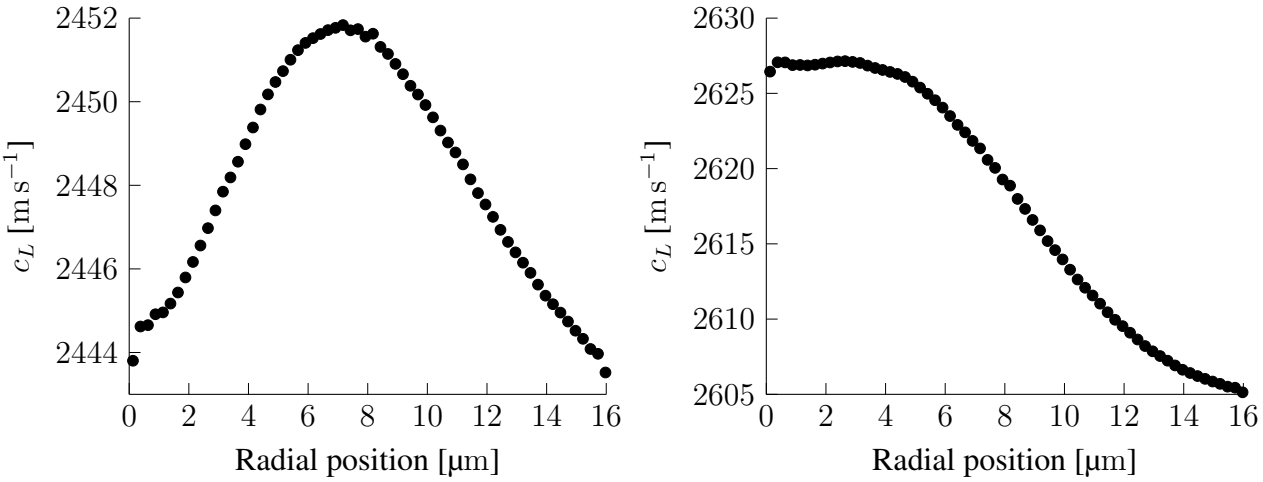

(a) Polystyrene is used as the core material.

(b) PMMA is used as the core material.

Figure 3.11: The velocity profiles of the axisymmetric model with parameters: $R = 15\,\mu\mathrm{m}$, $\eta = 0.1\,\mu\mathrm{m}$, $\vartheta_p = 0.55$ and a mesh size of $0.25\,\mu\mathrm{m}$. Each mark represent velocity of one element column. Note the scaling difference of the two plots; the difference between the minimum and maximum is $9\,\mathrm{m\,s^{-1}}$ and $22\,\mathrm{m\,s^{-1}}$ for polystyrene and PMMA as core material, respectively.

When the velocity for every column is estimated, we need to average the velocities in order to find the parameters describing the homogeneous approximation of the heterogeneous ICA. Because our FE model is axisymmetric, we must take into account that every element represents an annulus, as each element is supposed to be revolved around the symmetry axis. The annulus furthest out

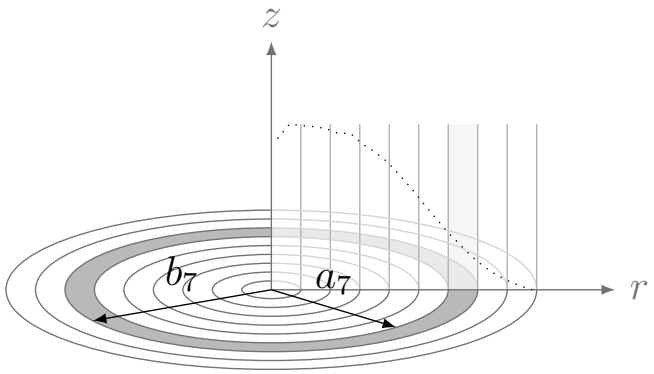

Figure 3.12: The velocity of the material must be approximated by a weighted average because of the axisymmetric approximation. Note that this figure is for illustration purposes only. The graph has a much finer resolution than the annuli. The velocity across an element is constant.

from the symmetry axis has a much greater area, then the innermost, and should therefore weigh more in an averaging of the velocity. We do a weighted average

$$\bar{\dot{u}} = \sum_{n=1}^{N} \dot{u}_n \frac{b_n^2 - a_n^2}{w^2}, \tag{3.20}$$

where n is the element number, N is the total number of elements along the bottom edge and a and b are the inner and outer radius of the element annulus, as illustrated in fig. 3.12 for the seventh element. Henceforth, every reference to the FE models' velocities are the weighted velocities.

3.8 Computational Costs

When we use explicit integration methods, the cost per time step is low, but so is the critical time step. As we know from eq. (2.95), the critical time step is proportional to the size of the elements; smaller elements give smaller time steps. Figure 3.13 shows the section between two particles with and without connection, which tells us that for the FE model to capture the geometry of connected particles, it needs small elements. A single small element (with large stiffness, which is the case for silver) may seriously reduce the Δt_{cr} for the entire FE mesh. [8] The computational cost are therefore higher for the random FE models, than for the ordered FE models.

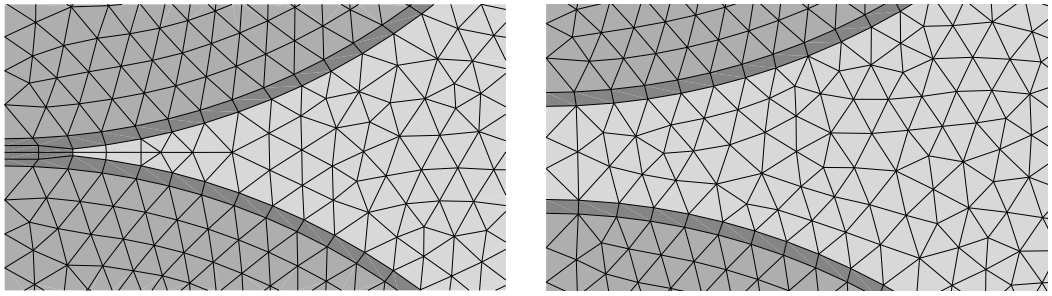

(a) Two particles with connection. **(b)** Two particles with no connection.

Figure 3.13: $R = 5.0\,\mu\text{m}$, $\eta = 0.1\,\mu\text{m}$ and $\xi = 0.5\,\mu\text{m}$. The overall mesh size is $0.25\,\mu\text{m}$. We can see how the element size is reduced to capture the geometry of the connection zone.

3.9 Two-Step Homogenization scheme

The Three Phase Model is used for homogenization of a two-phase composite. In our case, we want to use it to find the effective properties of a three-phase composite. We must therefore use it in two steps; first we find the effective properties of a homogeneous particle and then we use that effective particle and homogenize the composite, as illustrated in fig. 3.14. When we later use the TPM, it is this two-step scheme we refer to.

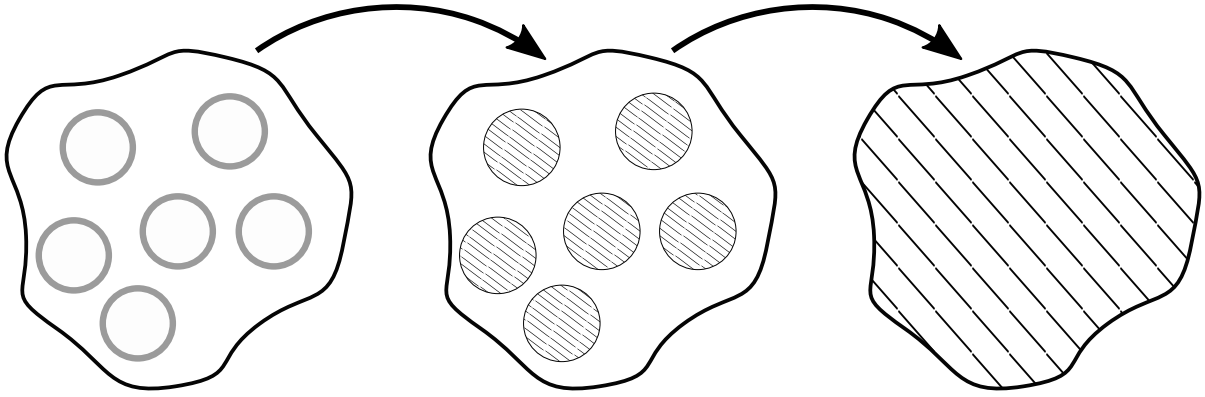

Figure 3.14: The composite must be homogenized in two steps; first the two-phase particles, then the composite with the homogeneous particles.

3.10 Verification of the FE model

To do numerical experiments using the FE models, the models need to be verified in the range of interest. We will do three types of verification studies:

- *RVE Verification* where we study the length scale of averaging of the model, i.e. the size of the FE model needed for the heterogeneous ICA to be approximated as a homogeneous material.
- *Mesh Independence* where we study the mesh dependency of the FE models.
- *Random Model Boundaries* where we study the random distribution of acoustic impedance using the random FE model, and whether the fully connected and ordered FE models might function as bounds on the distribution.

We will first represent the method used, followed by the results and in the end a discussion of these results. We choose to include this part in the method chapter of the thesis, because the results of the study are used to verify the models we will use for our numerical experiments later in this thesis.

3.10.1 Method

RVE Verification

We want to verify the size of our FE model, making sure it is a RVE. By means of the homogenization theory in section 2.4.1, we let the radius of a sphere be the characteristic dimension of the inhomogeneity, and the length scale of averaging be the height of the model. Because of the way the model is created, the height of the model is decided by how many spheres we include, thus our length scale of averaging is related to the number of spheres used in our model. To be able to reduce computational cost, but also making sure the model gives adequate result, we must study how many spheres we must include in the model for it to be an RVE. By doing simulations on a model with the exact same geometric parameters, and only changing the number of spheres included, we can study the convergence of the model with respect to number of spheres.

We want to find the necessary height for the model to be homogeneous, which is when the velocity with respect to number of particles included converge. Let us assume that the model

including the most particles has the exact solution of the longitudinal velocity. The velocity error of a model with fewer particles can then be expressed as

$$\epsilon_{c_\mathrm{L}}^{\mathrm{RVE}}(N) = \frac{|\hat{c}_\mathrm{L}^{(N)} - \hat{c}_\mathrm{L}^{\mathrm{NX}}|}{\hat{c}_\mathrm{L}^{\mathrm{NX}}}, \quad 2 \leq N \leq X. \tag{3.21}$$

where $\hat{c}_\mathrm{L}^{(N)}$ is the approximated longitudinal velocity of a model with N particles and $\hat{c}_\mathrm{L}^{\mathrm{NX}}$ is the assumed exact longitudinal velocity when X particles are included, being the model with the most particles.

Because we are going to do simulations on various designs, the model must be valid for all these variations. If we can create one model that captures the worst possible design in terms of simulation errors, we can use the verification of that model as a measure of the necessary model size needed for it to be an RVE. However, this is easier said than done, as we do not know what design is the worst.

We will assume that the length scale of averaging, δ, is the same for all models, thus the height of all the models is the same, independent of the size of the particles. The total height of both the FE model with continuous contact between spheres and the ordered model is

$$\delta = 2w \cdot N, \tag{3.22}$$

where N is the number of spheres included. Substituting eq. (3.7) into eq. (3.22) yields

$$\delta = 2\sqrt[3]{\frac{2}{3\vartheta_p}}\,(R+\eta)\,N. \tag{3.23}$$

This hypothesis must be tested, so we will do simulations on three models of different radius, $5\,\mu\mathrm{m}$, $10\,\mu\mathrm{m}$ and $15\,\mu\mathrm{m}$ and use that result to find the necessary height. The shell thickness will not contribute much to the total height of the model; however, the thinnest shell has the smallest elements. Even if we chose the global mesh size to be $0.25\,\mu\mathrm{m}$, a shell thinner than this has smaller elements for it to capture the geometry. It is known that abrupt changes in element size should be avoided, because a disturbance appears in the gradient field in the neighbourhood of an abrupt element size change [8]. We want to verify the worst possible design of the FE model, and therefore

choose the volume fraction of particles and shell thickness so that we have the densest packed FE model with the thinnest shell in our range of interest, i.e.:

$$\eta = 0.1\,\mu\text{m} \quad \text{and} \quad \vartheta_p = 0.55\,\text{vol}\%. \tag{3.24}$$

Table 3.1 tells us that PMMA has a higher longitudinal velocity than polystyrene, but how it will affect the necessary height is not clear to us at this point. We therefore study both PMMA and polystyrene as the core material. Summing up the parameters:

$$R = 5\,\mu\text{m}, 10\,\mu\text{m and } 15\,\mu\text{m}, \quad \eta = 0.1\,\mu\text{m}, \quad \vartheta_p = 0.55 \quad \text{and} \quad \xi = 0.5\,\mu\text{m}. \tag{3.25}$$

To reduce computational cost, we only use the ordered model when we study polystyrene. To further test our hypothesis stating that δ is equal for all models in the range stated in eqs. (3.1) to (3.3), we do two more convergence studies, one with PMMA as the core material and another with polystyrene, but now we choose

$$R = 8\,\mu\text{m}, \quad \eta = 0.2\,\mu\text{m}, \quad \vartheta_p = 0.45 \quad \text{and} \quad \xi = 1.5\,\mu\text{m}. \tag{3.26}$$

The results are presented in section 3.10.2, where we first present the results with PMMA as the core material in figs. 3.15 to 3.18, then for polystyrene in figs. 3.19 to 3.22.

Mesh Independence

To decide the proper mesh for all future models, we must examine their mesh dependency. We will do two studies; a pure material convergence study, and a composite convergence study. In the first one, we compare the approximated velocity to the material velocity in table 3.1, and in the latter, we compare the approximated velocity to the approximation using the finest meshing. The error in meshing is calculated by

$$\epsilon_{c_\text{L}}^{\text{pure}} = \frac{|\hat{c}_\text{L} - c_\text{L}|}{c_\text{L}} \quad \text{for the pure material and} \tag{3.27}$$

$$\epsilon_{c_\text{L}}^{\text{comp}} = \frac{|\hat{c}_\text{L} - \bar{c}_\text{L}|}{\bar{c}_\text{L}} \quad \text{for the composite,} \tag{3.28}$$

where $\bar{c}_{\mathrm{L}}$ is the approximated velocity with the finest meshing. We expect the mesh error to be largest at the core-shell and shell-adhesive interfaces, due to the transition in element size, element type and material. By increasing the number of particles in our model, we also increase the number of interfaces. From the results of the RVE verification study in section 3.10.2, we know that the model with the smallest particles needs to include the most particles to fulfil our requirement of the RVE size. Thus, we believe that the smallest particles will create the worst design in terms of simulation errors, and therefore use the following geometric parameters:

$$R = 5\,\mu\mathrm{m}, \quad \eta = 0.1\,\mu\mathrm{m}, \quad \vartheta_p = 0.55, \quad \text{and for the random,} \quad \xi = 0.5\,\mu\mathrm{m}. \tag{3.29}$$

We will do two pure material convergence studies; one for each of the FE models where we use silver as the material. The idea is that since silver has the greatest velocity, it will be the most sensitive material to a bad mesh. We will construct the model just like before, with cores, shells, matrix and contact zones, but now every constituent will consist of silver. The height of the model has been decided by the result of the RVE Verification in section 3.10.2. When we study the random model, all the spheres are linked together. We will also do two composite convergence studies using PMMA as the core material for each of the two models. The results are presented in tables 3.2 to 3.5 and fig. 3.23.

Random Model Boundaries

The random model is created such that spheres can be connected in the z-direction, to try to capture the effect of percolation. How many spheres that make up a chain is unknown and random. We can do many simulations to create a selection to be able to say anything about the random distribution of acoustic impedance. This is computational expensive, so if we instead can come up with the geometries that create the lowest and greatest velocities, they may function as boundaries for all random geometries. Our immediate thought is that the velocity of the FE model is highest when all the particles are connected, and lowest when no particles are connected. We will use three designs where we only change the radius, use PMMA as the core material, a mesh size of $0.5\,\mu\mathrm{m}$ and

$$R = 5\,\mu\mathrm{m},\ 10\,\mu\mathrm{m} \text{ and } 15\,\mu\mathrm{m} \quad \eta = 0.2\,\mu\mathrm{m}, \quad \vartheta_p = 55\%, \quad \text{and} \quad \xi = 0.5\,\mu\mathrm{m}. \tag{3.30}$$

We then do twelve simulations for each design, ten simulations using the random model with random chain lengths, one with continuous contact between spheres and one using the ordered model. In this study, we mainly use the random model, which has a high computational cost, explained in section 3.8. We therefore want to reduce the cost by using the mesh size $0.5\,\mu\mathrm{m}$, and table 3.5 tells us that the error is approximately $0.11\,\%$ for continuous connected particles. The result is plotted in fig. 3.24.

3.10.2 Results

We here present the results of the studies described in section 3.10.1. We start by presenting the results of the RVE verification studies, then follows results from the mesh independence studies and last we present results of the random model boundaries study.

RVE Verification The results of the RVE verification study are presented in figs. 3.15 to 3.22, in the same order as in section 3.10.1; first for the models with PMMA as the core material and radii

$$R = 5\,\mu\text{m},\ 10\,\mu\text{m},\ 15\,\mu\text{m} \text{ and } 8\,\mu\text{m},$$

then for the models with polystyrene as the core material.

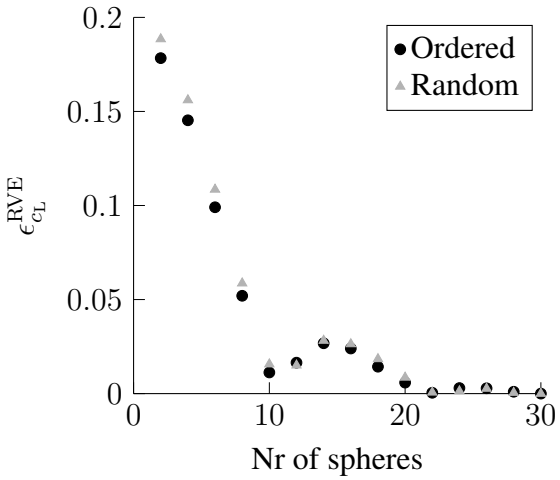

(a) Error of the velocity plotted against the number of spheres.

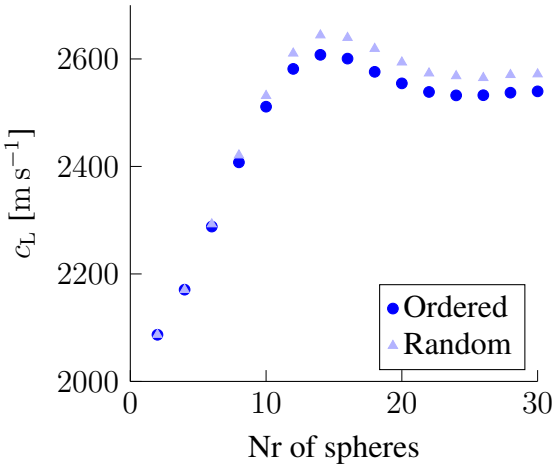

(b) Actual approximated velocity plotted against number of spheres.

Figure 3.15: Model with parameters: $R = 5\,\mu\text{m}$, $\eta = 0.1\,\mu\text{m}$, $\vartheta_p = 0.55$ and for the random FE model: $\xi = 0.5\,\mu\text{m}$. PMMA is used as the core material. A model with only two spheres has an error of 17.8% and 18.8% for the ordered and random model, respectively. However, by including 22 spheres we reduce the error down to only 0.04% and 0.06%.

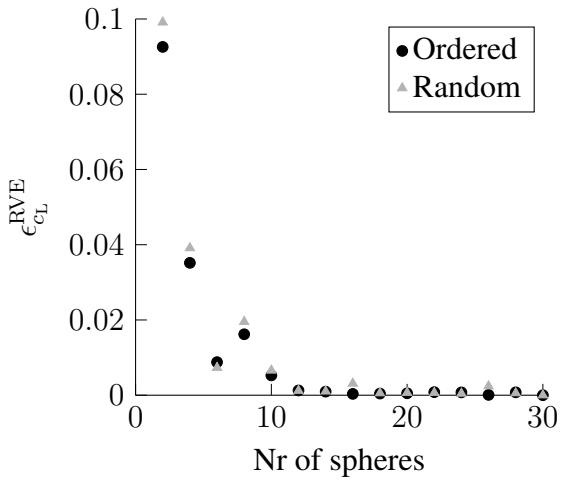

(a) Error of the velocity plotted against the number of spheres.

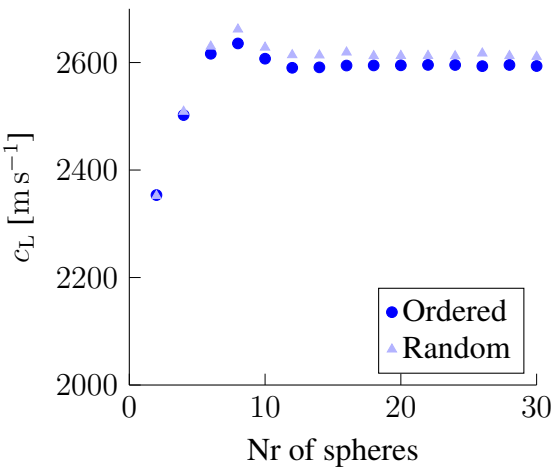

(b) Actual approximated velocity plotted against number of spheres.

Figure 3.16: Model with parameters: $R = 10\,\mu\text{m}$, $\eta = 0.1\,\mu\text{m}$, $\vartheta_p = 0.55$ and for the random FE model: $\xi = 0.5\,\mu\text{m}$. PMMA is used as the core material. A model with only two spheres has an error of 9.3% and 9.9% for the ordered and random model, respectively. However, by including twelve spheres we reduce the error down to 0.13% and 0.12%.

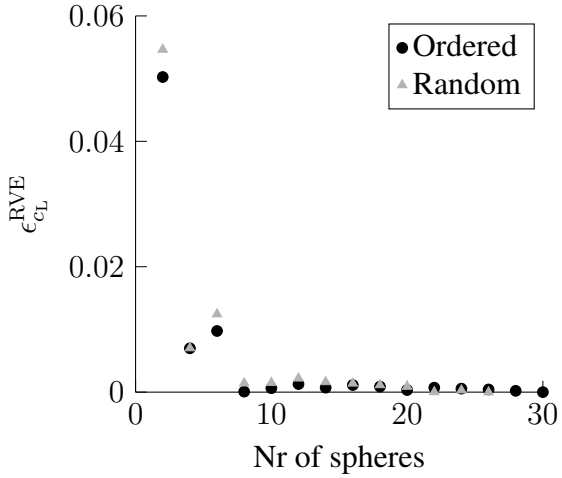

(a) Error of the velocity plotted against the number of spheres.

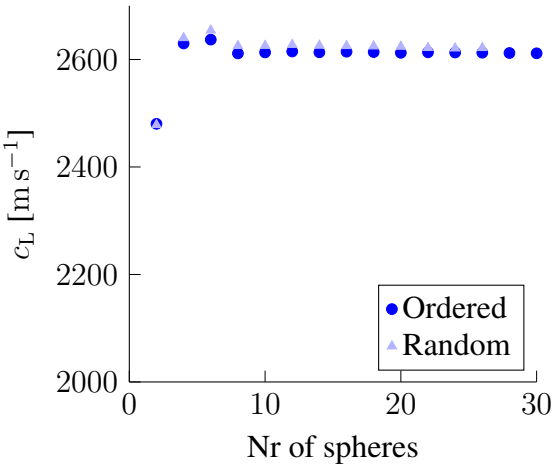

(b) Actual approximated velocity plotted against number of spheres.

Figure 3.17: Model with parameters: $R = 15\,\mu\text{m}$, $\eta = 0.1\,\mu\text{m}$, $\vartheta_p = 0.55$ and for the random FE model: $\xi = 0.5\,\mu\text{m}$. PMMA is used as the core material. A model with only two spheres has an error of 5.0% and 5.5% for the ordered and random model, respectively. However, by including eight spheres we reduce the error down to 0.01% and 0.15. Note that the study stopped at 26 spheres for the random FE model, which means that the error is measured against the value at $X = 26$.

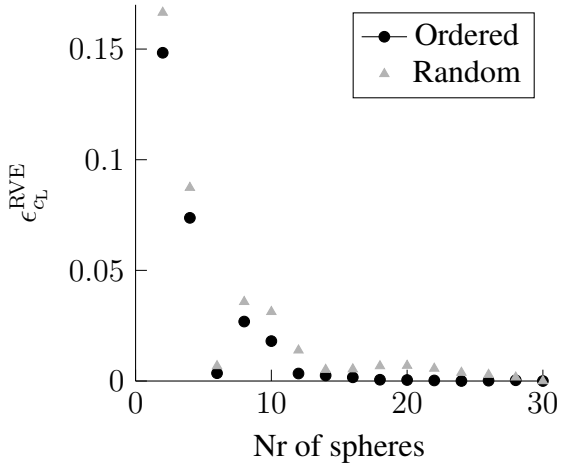

(a) Error of the velocity plotted against the number of spheres.

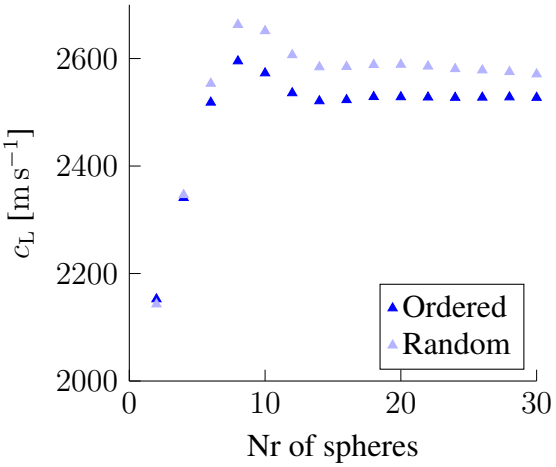

(b) Actual approximated velocity plotted against number of spheres.

Figure 3.18: Model with parameters: $R = 8\,\mu\mathrm{m}$, $\eta = 0.2\,\mu\mathrm{m}$, $\vartheta_p = 0.45$ and for the random FE model: $\xi = 1.5\,\mu\mathrm{m}$. PMMA is used as the core material. A model with only two spheres has an error of 14.8% and 16.6% for the ordered and random model, respectively. However, by including 14 spheres we reduce the error down to 0.25% and 0.51%.

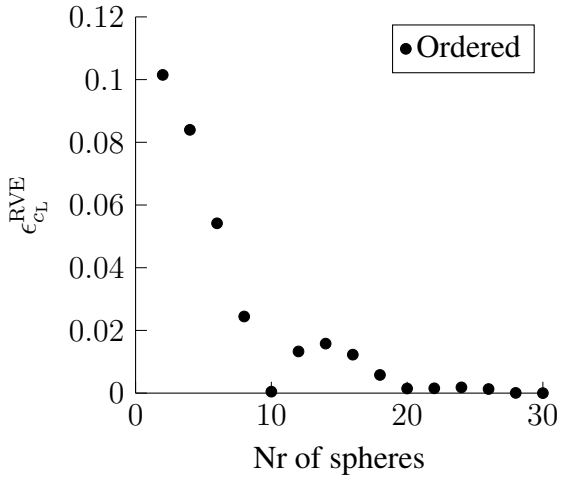

(a) Error of the velocity plotted against the number of spheres.

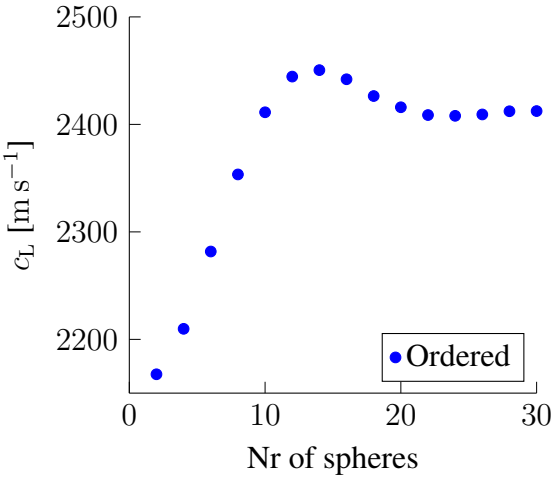

(b) Actual approximated velocity plotted against number of spheres.

Figure 3.19: Model with parameters: $R = 5\,\mu\mathrm{m}$, $\eta = 0.1\,\mu\mathrm{m}$, $\vartheta_p = 0.55$. Polystyrene is used as the core material. A model with only two spheres has an error of 10.1%. However, by including 20 spheres we reduce the error down to only 0.15%.

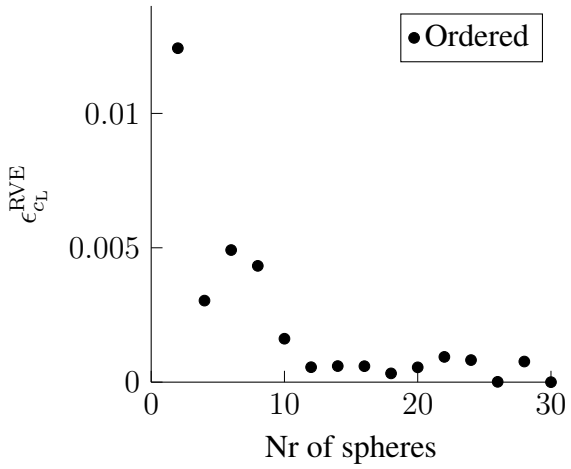

(a) Error of the velocity plotted against the number of spheres.

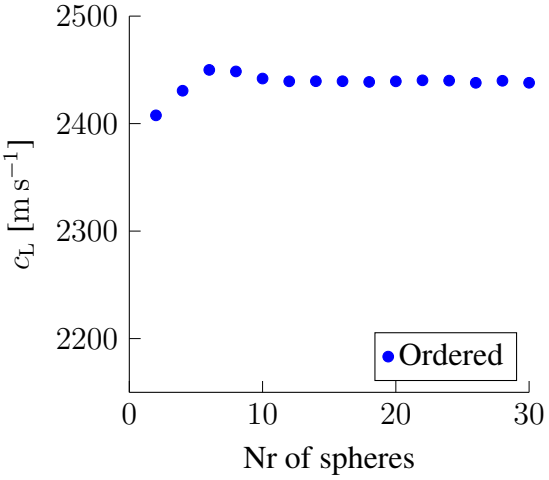

(b) Actual approximated velocity plotted against number of spheres.

Figure 3.20: Model with parameters: $R = 10\,\mu\text{m}$, $\eta = 0.1\,\mu\text{m}$, $\vartheta_p = 0.55$. Polystyrene is used as the core material. A model with only two spheres has an error of only 1.2%. However, by including ten spheres we reduce the error down to 0.16%.

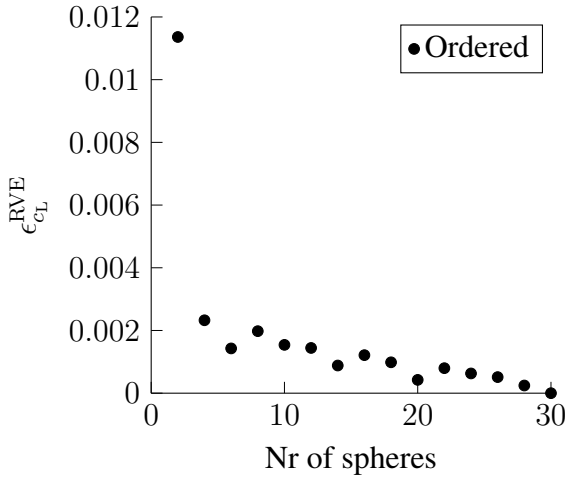

(a) Error of the velocity plotted against the number of spheres.

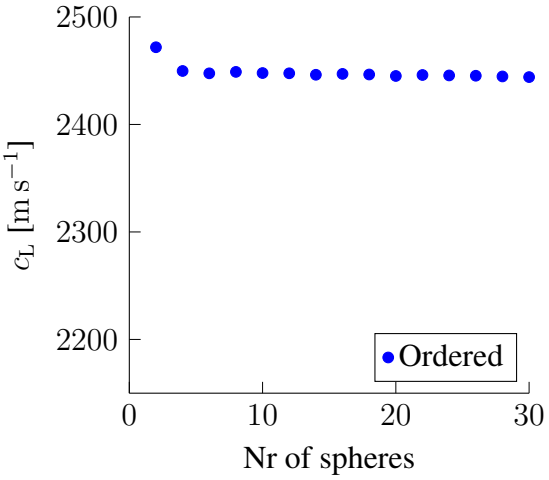

(b) Actual approximated velocity plotted against number of spheres.

Figure 3.21: Model with parameters: $R = 15\,\mu\text{m}$, $\eta = 0.1\,\mu\text{m}$, $\vartheta_p = 0.55$. Polystyrene is used as the core material. A model with only two spheres has an error of 1.1%. If we include six spheres we reduce the error down to 0.14%.

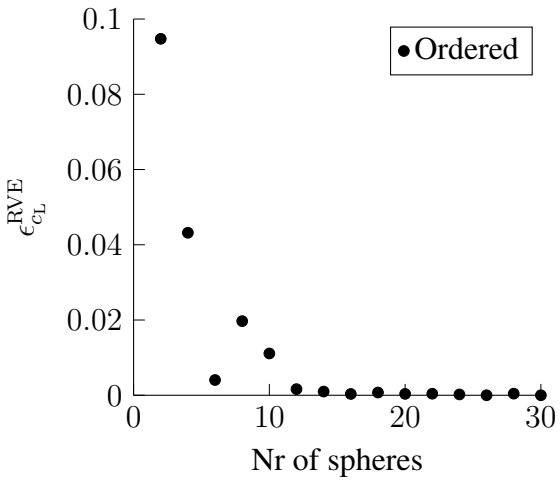

(a) Error of the velocity plotted against the number of spheres.

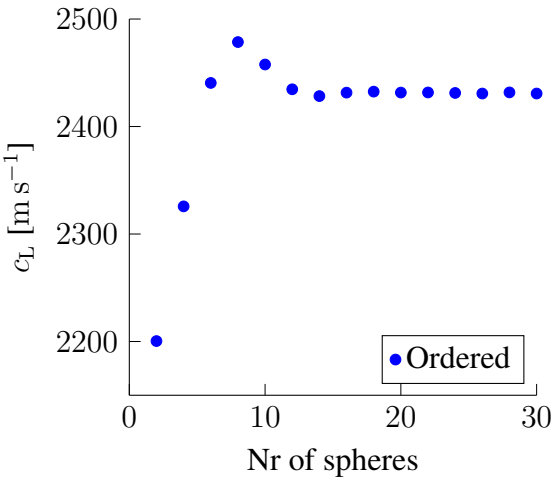

(b) Actual approximated velocity plotted against number of spheres.

Figure 3.22: Model with parameters: $R = 8\,\mu\mathrm{m}$, $\eta = 0.2\,\mu\mathrm{m}$, $\vartheta_p = 0.45$. Polystyrene is used as the core material. A model with only two spheres has an error of 9.5%. If we include 12 spheres we reduce the error down to 0.16%.

Mesh Independence

The results from the pure material studies are tabulated in tables 3.2 and 3.3, and the results from the composite studies are tabulated in tables 3.4 and 3.5. We note that the error using the coarsest mesh is less than $1\,\%$, and the error is greatest for the composites. We also note the small difference in error, while there is a great difference in numbers of elements used (N_{elem}). The velocity profile of the models in table 3.4 are plotted in fig. 3.23, and shows how the number of elements increase the resolution of the velocity profile.

Table 3.2: Mesh study of the ordered FE model with silver as the only material.

Mesh Size [µm]	$\hat{c}_{\text{L}}$ [$\text{m}\,\text{s}^{-1}$]	$\epsilon_{c_{\text{L}}}^{\text{pure}}[\%]$	N_{elem}
1.0	3582.5	0.07	3639
0.5	3582.2	0.06	13926
0.25	3579.5	0.01	53698
0.125	3581.5	0.04	193807

Table 3.3: Mesh study of the random FE model with silver as the only material.

Mesh Size [µm]	$\hat{c}_{\text{L}}$ [$\text{m}\,\text{s}^{-1}$]	$\epsilon_{c_{\text{L}}}^{\text{pure}}[\%]$	N_{elem}
1.0	3581.4	0.04	5198
0.5	3580.5	0.01	15120
0.25	3582.0	0.06	54123
0.125	3578.6	0.04	198874

Table 3.4: Mesh study of the ordered FE model for the composite with PMMA as the core material.

Mesh Size [µm]	$\hat{c}_{\text{L}}$ [$\text{m}\,\text{s}^{-1}$]	$\epsilon_{c_{\text{L}}}^{\text{comp}}[\%]$	N_{elem}
1.0	2535.5	0.23	3639
0.5	2532.6	0.11	13926
0.25	2532.2	0.10	53698
0.125	2533.5	0.15	193807
0.0625	2529.7	-	770802

Table 3.5: Mesh study of the random FE model for the composite with PMMA as the core material.

Mesh Size [µm]	$\hat{c}_{\mathrm{L}}$ [$\mathrm{m\,s^{-1}}$]	$\epsilon_{c_{\mathrm{L}}}^{\mathrm{comp}}[\%]$	N_{elem}
1.0	2573.2	0.2	5198
0.5	2566.8	0.04	15120
0.25	2568.3	0.01	54123
0.125	2565.5	0.09	198874
0.0625	2567.9	-	767697

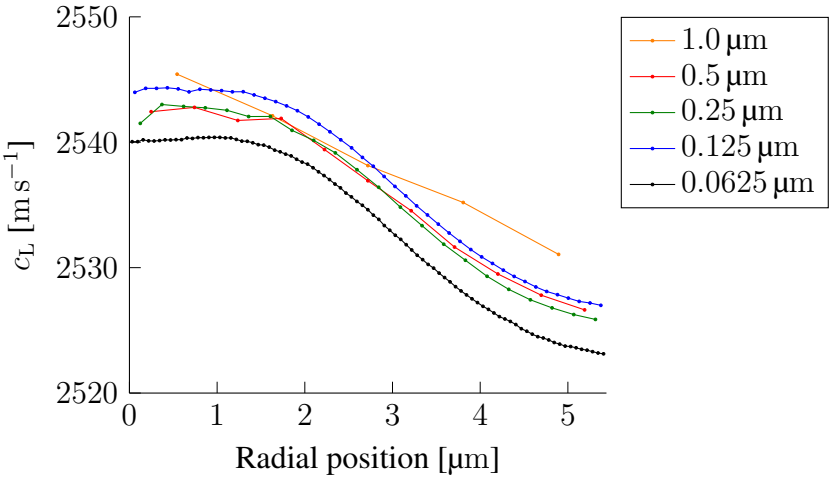

Figure 3.23: Velocity profile of the composite using the ordered FE model with PMMA as the core material. Each mark represents an elements' integration point. The lines between the marks are there only for illustration, as the velocity is constant over the elements. The models are tabulated in table 3.4.

Random Model Boundaries

The results from the random model boundaries are plotted in fig. 3.24. We note that the ordered model is not the lower boundary, but it seems like the continuous connected model is the upper boundary for the random distribution.

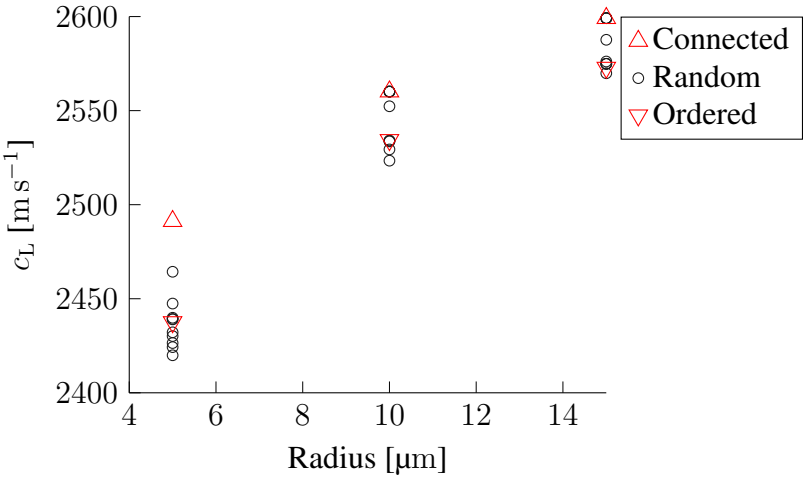

Figure 3.24: The fully connected model might function as a upper limit, but the ordered does not function as a lower limit, as it is closer to an average than a boundary.

3.10.3 Discussion

RVE Verification

We will first discuss the results from the models with PMMA as the core material. We use eq. (3.23) for the three models, i.e.:

$$\delta_5 = 2\sqrt[3]{\frac{2}{3\vartheta_p}}\left(R_5 + \eta\right) N_5, \tag{3.31}$$

$$\delta_{10} = 2\sqrt[3]{\frac{2}{3\vartheta_p}}\left(R_{10} + \eta\right) N_{10}, \tag{3.32}$$

$$\delta_{15} = 2\sqrt[3]{\frac{2}{3\vartheta_p}}\left(R_{15} + \eta\right) N_{15}, \tag{3.33}$$

where the subscripts refer to the radius used in the model. Substituting R_{15} and R_{10} in these

equations with $3R_5$ and $2R_5$, respectively and neglecting the thickness of the shell, yields

$$\delta = 2\sqrt[3]{\frac{2}{3\vartheta_p}}R_5 N_5, \tag{3.34}$$

$$\delta = 2\sqrt[3]{\frac{2}{3\vartheta_p}}2R_5 N_{10}, \tag{3.35}$$

$$\delta = 2\sqrt[3]{\frac{2}{3\vartheta_p}}3R_5 N_{15}, \tag{3.36}$$

where we have assumed that the length scale of averaging is the same for all models ($\delta_5 = \delta_{10} = \delta_{15} = \delta$). We get the following relation for the necessary number of spheres in the RVE

$$N_5 = 2N_{10} = 3N_{15}. \tag{3.37}$$

The plots in figs. 3.15 to 3.17 show the error and longitudinal velocity for with different configurations, and tells us that the necessary number of particles for the model to represented by a homogeneous material is

$$N_5 = 22, \tag{3.38}$$

$$N_{10} = 12, \tag{3.39}$$

$$N_{15} = 8, \tag{3.40}$$

which almost satisfies eq. (3.37). Note the scaling difference of the different error plots. Because $2N_{10}$ and $3N_{15}$ make the upper bound, we use eq. (3.33) to decide the height of the RVE, our length scale of averaging:

$$\delta^{\mathrm{PMMA}} = \delta_{15} = 2\sqrt[3]{\frac{2}{3 \cdot 0.55}}\,(15\,\mu\mathrm{m} + 0.1\,\mu\mathrm{m}) \cdot 8 = 257.6\,\mu\mathrm{m}. \tag{3.41}$$

It should be noted that we have assumed that the height is valid for any sphere radius in the range of $5 - 15\,\mu\mathrm{m}$, and that a change in the volume fraction and shell thickness is not considered. We test the height criteria in eq. (3.41) on the configuration in eq. (3.26) which is plotted in fig. 3.18.

Let N_8 be any whole number greater or equal to what we get using the height $257\,\mu\mathrm{m}$, i.e.:

$$N_8 \geq \frac{257\,\mu\mathrm{m}}{2\sqrt[3]{\frac{2}{3\cdot 0.45}}(8\,\mu\mathrm{m}+0.2\,\mu\mathrm{m})} = 13.7, \quad \Rightarrow N_8 = 14. \tag{3.42}$$

From the plot in fig. 3.18 we see that the error for $N = 14$ is down to 0.25% and 0.51%. Compared to the other results, these are higher values, but we can clearly see a tendency of convergence at $N = 14$ thus the assumption of $\delta^{\mathrm{PMMA}} = 257\,\mu\mathrm{m}$ gives a fair approximation for the necessary height, even when we change the volume fraction, shell thickness and contact width.

We use the same procedure for the result with polystyrene as the core material:

$$N_5 = 20, \tag{3.43}$$

$$N_{10} = 10, \tag{3.44}$$

$$N_{15} = 6, \tag{3.45}$$

and again, using eq. (3.37), we have N_{10} as the upper bound. The necessary height of the FE model with polystyrene as the core material is found to be

$$\delta^{\mathrm{PS}} = \delta_{10} = 2\sqrt[3]{\frac{2}{3\cdot 0.55}}\,(10\,\mu\mathrm{m}+0.1\,\mu\mathrm{m})\cdot 10 = 215\,\mu\mathrm{m}. \tag{3.46}$$

In the same way as before, we test the height criteria in eq. (3.46) on the configuration in eq. (3.26):

$$N_8 \geq \frac{215\,\mu\mathrm{m}}{2\sqrt[3]{\frac{2}{3\cdot 0.45}}(8\,\mu\mathrm{m}+0.2\,\mu\mathrm{m})} = 11.5, \quad \Rightarrow N_8 = 12. \tag{3.47}$$

From the plot in fig. 3.22 we see that for $N = 12$, the error is down to 0.16%, thus the assumption of $\delta^{\mathrm{PS}} = 215\,\mu\mathrm{m}$ gives a fair approximation of the necessary height.

We did not do a convergence study of polystyrene as the core material with continuously connected spheres. This is because the results of the continuously connected PMMA shows the same pattern as the ordered model. To reduce computational costs, we use the result of the fully ordered model with polystyrene as the core material to decide the necessary height of the RVE for the ho-

mogeneous approximation of the heterogeneous ICA. What should be noted is that to be able to do a homogeneous representation, the height of the FE model must be greater than $215\,\mu\mathrm{m}$ and $257\,\mu\mathrm{m}$ when we use polystyrene and PMMA as the core material, respectively. By using the definition of wavelength in eq. (2.62), we get

$$\Lambda_{\mathrm{L}}^{\mathrm{PMMA}} \approx 508 - 524\,\mu\mathrm{m}, \tag{3.48}$$

$$\Lambda_{\mathrm{L}}^{\mathrm{PS}} \approx 482 - 489\,\mu\mathrm{m}, \tag{3.49}$$

where we have used the velocity $c_{\mathrm{L}}^{\mathrm{NX}}$. The range in wavelength is because of the difference in velocity when using different core radii. What we see is that the necessary height to approximate the composite as a homogeneous material is

$$\delta^{\mathrm{PMMA}} \approx 0.5\Lambda_{\mathrm{L}}^{\mathrm{PMMA}} \tag{3.50}$$

$$\delta^{\mathrm{PS}} \approx 0.44\Lambda_{\mathrm{L}}^{\mathrm{PS}} \tag{3.51}$$

Because the composite is intended to be a transducer layer of a $\Lambda/4 \approx \delta/2$ in thickness, it seems as if the composite may *not* be regarded as a homogeneous material. The wavelength is decided by the velocity of the material, which varies with the thickness when it is thinner than δ. We are therefore left with an implicit problem to decide the $\Lambda/4$ thickness of the material:

$$\text{thickness } L = \frac{c_{\mathrm{L}}\left(L\right)}{4f_0}. \tag{3.52}$$

The velocity plots in figs. 3.15 to 3.22 shows that all the plots has a slight increase in velocity before they flatten out to what we here call the homogeneous longitudinal velocity, $c_{\mathrm{L}}^{\mathrm{NX}}$. We know from eqs. (3.50) and (3.51) that the velocity of a $\Lambda/4$ layer should be similar to the velocity approximated by half the model size as for the homogeneous RVE; $N_{\Lambda/4} = N/2$. If this velocity proves to be somewhat similar to the homogeneous velocity, we can use the homogeneous velocity to approximate the thickness of the $\Lambda/4$ layer. Equation (3.52) can then be written as

$$\text{thickness } L = \frac{c_{\mathrm{L}}^{\mathrm{NX}}}{4f_0}. \tag{3.53}$$

The number of particles needed for the FE model to have a thickness of a $\Lambda/4$ is then found by substituting δ in eq. (3.23) for L in eq. (3.53). Solving for $N_{\Lambda/4}^{\mathrm{NX}}$ yields

$$N_{\Lambda/4}^{\mathrm{NX}} \geq \frac{c_{\mathrm{L}}^{\mathrm{NX}}}{8 f_0 \sqrt[3]{\frac{2}{3 \cdot \vartheta_p}} (R + \eta)}. \tag{3.54}$$

Let $R = 10\,\mu\mathrm{m}$, $\eta = 0.1\,\mu\mathrm{m}$, $\vartheta_p = 0.55$ as in fig. 3.16. The velocity, $c_{\mathrm{L}}^{\mathrm{NX}}$, is approximated to be

$$c_{\mathrm{L}}^{\mathrm{NX}} = 2593\,\mathrm{m\,s^{-1}},$$

which, by substituting into eq. (3.54), gives

$$N_{\Lambda/4}^{\mathrm{NX}} \geq 5.8297.$$

If we now do the exact same, but now use the velocity approximated with six particles;

$$c_{\mathrm{L}}^{\mathrm{N6}} = 2616\,\mathrm{m\,s^{-1}},$$

we get

$$N_{\Lambda/4}^{\mathrm{N6}} \geq 5.88.$$

This tells us that the velocity calculated for the homogeneous material might be used to approximate the $\Lambda/4$ thickness of composite. If there is a way to estimate the homogeneous velocity without using FE models, this estimate can be used to approximate the number of particles needed for it to be a quarter wavelength transducer layer. The FE model can then be used to approximate the acoustic impedance of the heterogeneous layer. We are not able to test this hypothesis, because the material samples (tabulated in table 3.6) used for measurement are much too thick ($L >> \Lambda/4$). To test it, we need to do measurements on composite samples with a $\Lambda/4$ thickness, which at this point has not been done. We therefore recommend to investigate this is a later study with samples of the correct thickness. We recommend also doing analyses and measurements with different centre frequencies, such that it might be possible to find an expression for the height with respect to the

wavelength, particle size and shell thickness. Note also that the velocity plots have an interestingly close shape to that of a sinc-function and a converging exponential function. It may therefore be possible to find a mathematical expression that describes the velocity with respect to number of spheres. Unfortunately, we did not have time to investigate this any further. In the next chapter, we do a numerical study of design, and to simplify the analysis, we use the homogeneous case where the number of spheres included does not affect the approximated velocity. We found the necessary height with polystyrene as the core to be

$$N \geq \frac{215\,\mu\mathrm{m}}{2\sqrt[3]{\frac{2}{3\cdot\vartheta_p}}(R+\eta)} \tag{3.55}$$

and with PMMA

$$N \geq \frac{257\,\mu\mathrm{m}}{2\sqrt[3]{\frac{2}{3\cdot\vartheta_p}}(R+\eta)} \tag{3.56}$$

under the assumption of neglecting the shell thickness. If the shell thickness is increased, the assumption might be a source of error when calculating the necessary number of spheres calculated by eq. (3.55) and eq. (3.56).

When we look at the different velocity plots in figs. 3.15b, 3.16b and 3.17b where PMMA is the core material, we see a decrease in the homogeneous velocity when using smaller particles. Smaller core radius and a constant shell thickness gives a larger volume fraction of silver, and since silver has a larger velocity than PMMA, we would expect a smaller core radius to increase the homogeneous velocity. This is not the case, and when using cores of $5\,\mu\mathrm{m}$ and $10\,\mu\mathrm{m}$, the velocity is below that of any of the constituents. Smaller particles do increase the number of particles used in the FEA, but we see that when we use more particles in the models, it does not alter the homogeneous velocity result. Because the model is built on the basis of volume fraction of particles, a larger particle only increases the total size of the model. This means that the only difference between the result in figs. 3.15b and 3.17b is the volume fraction in the particles. We can therefore interpret this result that there might be possible to increase the thickness of silver coating and at the same time reduce the velocity. This would be ideal for a material that needs a low acoustic impedance and a high thermal conductivity. This hypothesis is investigated further in

section 5.3.

Mesh Independence

The tables 3.2 to 3.5 and fig. 3.23 tells us that the error difference for the different mesh sizes is very small, even though there is a large difference in number of elements used. The largest error difference is found in the composite using the ordered FE model. The coarsest mesh has an error of $0.23\,\%$ to the finest mesh, whereas the finest mesh has approximately 200 times as many elements! The top and bottom of the particles are areas where we most likely have stress concentrations. Stress concentrations are a source of numerical error in FEA, thus it needs finer meshing. The random model has much smaller elements on the top and bottom of the particles, because of the contact zones (see fig. 3.13), which act as a mesh refinement at the critical points. This mesh refinement may be the reason for why we see a greater error using the ordered model than the continuously connected model. The largest error, using the ordered model is still below $0.3\,\%$. The small error may be because the velocity is calculated using a weighted average, as described in section 3.7. This averaging scheme may smear out the error of the different elements. By the looks of fig. 3.23 we see how the resolution of the velocity profile is decided by the number of elements. The velocity profiles using the coarsest and finest mesh, 1.0 and $0.0625\,\mu\mathrm{m}$ stands out. The coarsest model shows an almost linear velocity profile, while the finest meshing has a velocity below all the other models. We will not use the finest mesh due to the high computational cost of using it. Since the velocity of the three other models are quite similar, we henceforth use the $0.25\,\mu\mathrm{m}$ mesh, unless other is specified.

Random Model Boundaries

Our initial thought was that the continuously connected model and the ordered model could act as bounds of to the random distribution. From the looks of fig. 3.24, this thought is clearly not correct. The ordered model is far from the lowest velocity approximated with the random model. It seems like the fully connected model might function as a upper bound, but the 30 random models do not give enough information to prove or disprove it. The ordered model is closer to the centre of the spread, so instead of using it as a boundary, we will instead use it as a mean. This is not entirely correct, but a good enough approximation for the scope of this thesis.

3.11 Comparing the FE Model with the ICA

The longitudinal wave velocity can be measured using ultrasound. One method is the so-called *discrete frequency method*, and its theory follows that of [23]. Two identical ultrasound transducers are mounted opposite each other in a water chamber. One of the transducers is used as an emitter and the other as receiver, and they both have resonance frequency at the centre frequency of interest. The pulse is chosen long enough so that its centre frequency is well-defined, yet short enough to avoid interference due to multiple reflections within the sample. A sample of thickness L, whose longitudinal velocity is to be estimated, is inserted so that the ultrasound pulse is transmitted normal to the surface and through the sample. By comparing the arrival time of the pulse with and without the sample, the longitudinal wave velocity of the sample can be estimated as

$$c_{\mathrm{L}} = \frac{c_{\mathrm{w}}}{1 + c_{\mathrm{w}} \Delta t / L} \tag{3.57}$$

where c_{w} is the velocity of water, Δt is the difference in arrival time of the pulse with and without the sample, and L is the thickness of the sample. SURF Technology AS has measured the longitudinal velocity of seven samples provided by Conpart AS, and the data is found in table 3.6. As mentioned in opening of this chapter, there is an uncertainty in the adhesive density of $10\,\%$ due to shrinking of the adhesive during curing. This is a systematic error, as it is related to the adhesive mixture, and should be constant if the same mixture in the adhesive is used. The effective density of the adhesive, $\rho_{\mathrm{M}}^{\mathrm{eff}}$, is calculated by assuming a $5\,\%$ increase of the density tabulated in table 3.1. It is the effective density that is used to calculate the effective acoustic impedance Z^{eff}. We will then use the FE model and the TPM to approximate the acoustic impedances for identical material compositions, so that we can compare the models to the actual materials. We have not included any shrinking of the adhesive in our approximation. The relative error of the FE model is calculated by

$$\epsilon^{\mathrm{eff}} = \frac{Z^{\mathrm{eff}} - Z^{\mathrm{FEM}}}{Z^{\mathrm{eff}}}. \tag{3.58}$$

The results are plotted in fig. 4.1 and tabulated in tables 4.1 and 4.2. SURF Technology AS have reported that there may be some errors in measured velocities of the samples. The ultrasound

probes used in the test-rig have a beam-width of about $10\,\mathrm{mm}$, which also is the diameter of the composite samples. This is problematic because parts of the sound beam go around the sample and into the receiver. The sample must be very well aligned with the beam to minimize the waves going around the sample. We would therefore recommend to do new measurements on samples with a diameter well above $10\,\mathrm{mm}$. SURF Technology AS suggest samples of at least $25\,\mathrm{mm}$. They also report that the samples had a rough surface, which also may contribute to errors. Our FE models have not been verified for composites with a shell thickness of $70\,\mathrm{nm}$ or radius of $20\,\mu\mathrm{m}$. We have chosen to include them anyways, because we only have measured velocities for a few composite samples.

Table 3.6: Particles and measured data provided by SURF Technology

ID	P-ID	Core	R [µm]	η [nm]	ϑ_p [vol%]	L [mm]	ρ_p [g cm^{-3}]	ρ_m^{eff} [g cm^{-3}]	c_{L} [m s^{-1}]	Z^{eff} [MRayl]
CA101-1	AA303-4	styrene	5	140	50	7.06	1.86	1.18	2346	3.56
CA101-2	AA303-4	styrene	5	140	48	6.44	1.86	1.18	2312	3.48
CA101-3	AA280-200	styrene	5	200	48	6.16	2.18	1.18	2296	3.81
CA101-4	AA342-1	PMMA	20	140	48	6.13	1.39	1.18	2584	3.31
CA102-1	AA280-070	styrene	5	70	48	6.59	1.47	1.18	2370	3.13
CA102-2	AA341-1	styrene	10	140	48	6.4	1.59	1.18	2522	3.47
CA102-3	AA121-b-16	PMMA	15	140	48	6.1	1.45	1.18	2564	3.36

3.12 Numerical Experiment in Design

When improving a design, one wants to learn how a quantity of interest is affected by changes in certain design variables. In our case, we want to reduce the acoustic impedance and increase the amount of silver in the material. We have a reason to believe that this can be done by changing certain geometric parameters and material properties. We have in the previous sections verified our FE model in a range of different numerical design variables. As long as we stay inside this range, we can undertake analyses of design [8]. From the analyses, we hope to learn the sensitivity of the acoustic impedance in each design variable, so that we can select the most favorable design. For most of the studies we will use the ordered model. We know from the results plotted in fig. 3.24, that the ordered model can be used as a mean of the random distribution of models.

In this chapter, we start by doing a sensitivity study of elastic properties, where we study the effects the elastic properties of the different constituents have on the acoustic impedance. SURF Technology AS and Conpart AS are designing the composite planned to be used in ultrasound transducers. As we mentioned in section 3.5, Conpart do not know the exact elastic properties of the materials included in the composite. They also have an uncertainty in the density of the adhesive of about $10\,\%$ due to shrinking during curing. The motivation for doing a sensitivity study of the elastic properties is to see how much a slight change in the different materials alter the acoustic impedance. The information obtained from the analyses can also be used as guidelines in choosing the materials in the different constituents of the composite. For every constituent, we will do three studies; Young's modulus, E, Poisson's ratio, ν and density, ρ. We then do analyses where we alter the geometric parameters of the design. We are interested in how much an impact the different properties and parameters have on the overall acoustic impedance. If a parameter changes the velocity AND the density of the material, we might experience a double effect, or a cancelling effect, since both these parameters are included in the calculation of the acoustic impedance.

The geometric properties and elastic parameters will be altered by $\pm 10\%$, and the impact of the

change will be calculated by

$$\Delta 90 = \left(1 - \frac{Z_{X90\%}}{Z_{X100\%}}\right) \cdot 100\%, \tag{3.59}$$

$$\Delta 110 = \left(\frac{Z_{X110\%}}{Z_{X100\%}} - 1\right) \cdot 100\%, \tag{3.60}$$

where X denotes the parameter/property being altered. This can be the radius, R, Young's modulus, E, or any other parameter of interest and the $\%$ denotes the percentage of the initial parameter/property. Z is the approximated acoustic impedance calculated using the ordered FE model. The exception is the analysis of the contact width. We expect a less distinctive change in the acoustic impedance when we alter the contact width, thus we alter it by $\pm 50\%$.

When doing numerical experiments in design, one wants to isolate as many parameters and effects as possible. This is not much of an issue when we vary the elastic properties, but when we alter the geometric parameters, this is sometimes easier said than done. Geometric parameters might be tightly intertwined, and not as easy to isolate. From the velocities and density in table 3.1 we can expect that an increase in volume fraction of silver will increase the overall acoustic impedance, while an increase in volume fraction of polystyrene will decrease the acoustic impedance. If we always change the geometric properties so that the volume fractions are kept constant, the different properties are isolated. This is what we call *scaling*, and by doing this we can isolate the effect of particle size. Let us say we instead increase the shell thickness, whilst keeping the core radius and particle fraction constant. By increasing the shell thickness, we also increase the particle radius. The volume fraction of particles is kept constant, but because we increased the shell thickness, the fraction of shell in the particle has increased, and we have thus also reduced the volume fraction of core material,

$$\vartheta_{\text{core}} = \frac{V_{\text{core}}}{V_{\text{particle}}} = \frac{R^3}{(R+\eta)^3}, \quad \vartheta_{\text{shell}} = 1 - \vartheta_{\text{core}} = \frac{R^3}{(R+\eta)^3}. \tag{3.61}$$

An increased shell thickness increases the amount of silver and reduces the amount of polystyrene, where both procedures has the effect of increasing the overall impedance. If we instead increase the core radius whilst keeping the shell thickness constant, we reduce the amount of silver and increase

the amount of polystyrene, both procedures having the effect of decreasing the overall impedance of the material. By increasing the young's modulus, we know from the longitudinal velocity in eq. (2.33) that we increase the velocity of the material. By increasing the Poisson's ratio, we also increase the velocity. However, by increasing the density, we reduce the velocity, but because the acoustic impedance is a product of velocity and density, an increase in density will increase the impedance. Thus, by increasing any of the elastic properties, we increase the acoustic impedance. To evaluate whether the homogenization method using the Three Phase Model from section 2.4.3 is applicable for our problem, we do the exact same parametric studies using the TPM. We then compare the results to the results using the FE model. The acoustic impedance approximated using the TPM is denoted $\bar{Z}$. The elastic properties that will be altered for every constituent are:

- Young's modulus, E.
- Poisson's ratio, ν.
- Density, ρ.

The geometric parameters that will be altered are:

- Sphere radius, R.
- Shell thickness, η.
- Contact width, ξ.
- Volume fraction of particles, ϑ_p.

In section 3.10.3, we saw how the homogeneous velocity of the composite decreased as the core radius decreased. We know from eq. (3.61) that a reduced core radius and a constant shell thickness results in a reduced volume fraction of core and an increased volume fraction of shell. Therefore, we have seen that the velocity of the composite is reduces as the shell fraction is increased. We will therefore try to find a volume fraction of the shell, ϑ_{shell}, that minimizes the acoustic impedance. We use the TPM to study a composite with $\vartheta_p = 50\,\text{vol}\%$. We will also use the TPM to see if there is a volume fraction of particles, ϑ_p in the range $45\,\text{vol}\%$ to $55\,\text{vol}\%$ that minimizes the acoustic

impedance of the composite. The range is decided so that it is above the percolation limit and below what we have been told to be a too viscous mixture. The results are plotted in figs. 4.10 and 4.11.

All the studies are based on the ordered model, unless other is specified. The initial geometry is:

$$R_0 = 10\,\mu\text{m}, \quad \eta_0 = 0.2\,\mu\text{m}, \quad \vartheta_{p0} = 50\,\%, \tag{3.62}$$

where the subscript "0" denotes the initial geometry. This gives an initial distribution of materials

$$47\,\% \text{ Core material},$$
$$3\,\% \text{ Shell material},$$
$$50\,\% \text{ Matrix material}.$$

When we do analyses of the contact width, we use the random model with a continuous connected system, and the same initial geometry as in eq. (3.62), but now also an initial contact width

$$\xi_0 = 1.0\,\mu\text{m}. \tag{3.63}$$

For all the models we use

$$\text{Core material: Polystyrene},$$
$$\text{Shell material: Silver},$$
$$\text{Matrix material: Epoxy},$$
$$\text{Mesh size: } 0.25\,\mu\text{m}.$$

Chapter 4

Results

This chapter presents the results of the comparison study and numerical experiment. The methods used to get the results are described in sections 3.11 and 3.12, respectively.

4.1 Comparing the FE Model with the ICA

The measured acoustic impedances in table 3.6 are plotted in fig. 4.1. As mentioned in section 3.11 the acoustic impedance is calculated using the density of the adhesive calculated with $5\,\%$ shrinking. The error bars in fig. 4.1 span the error in acoustic impedance, where the lowest is for a material with no shrinking of the adhesive and the greatest is for a material with a shrinkage of $10\,\%$. The approximations using the ordered FE model is marked by dark diamonds and the TPM as light squares. The density of the matrix material used in the approximations is the one tabulated in table 3.1 with no shrinking. Values are plotted in fig. 4.1 and tabulated in tables 4.1 and 4.2.

Table 4.1: The acoustic impedance of the particles plotted in fig. 4.1a. The unit of the tabulated impedances are MRayl, and is left out to make the table more readable.

ID	Core	R [µm]	η [nm]	ϑ_p [vol%]	Z^{min}	Z^{eff}	Z^{max}	Z^{TPM}	Z^{FEA}	$\epsilon^{\text{eff}}[\%]$
CA102-1	styrene	5	70	48	3.05	3.13	3.21	3.11	3.12	0.39
CA101-1	styrene	5	140	50	3.5	3.56	3.64	3.52	3.51	1.35
CA101-2	styrene	5	140	48	3.41	3.48	3.56	3.5	3.5	0.44
CA101-3	styrene	5	200	48	3.74	3.81	3.89	3.79	3.78	0.78

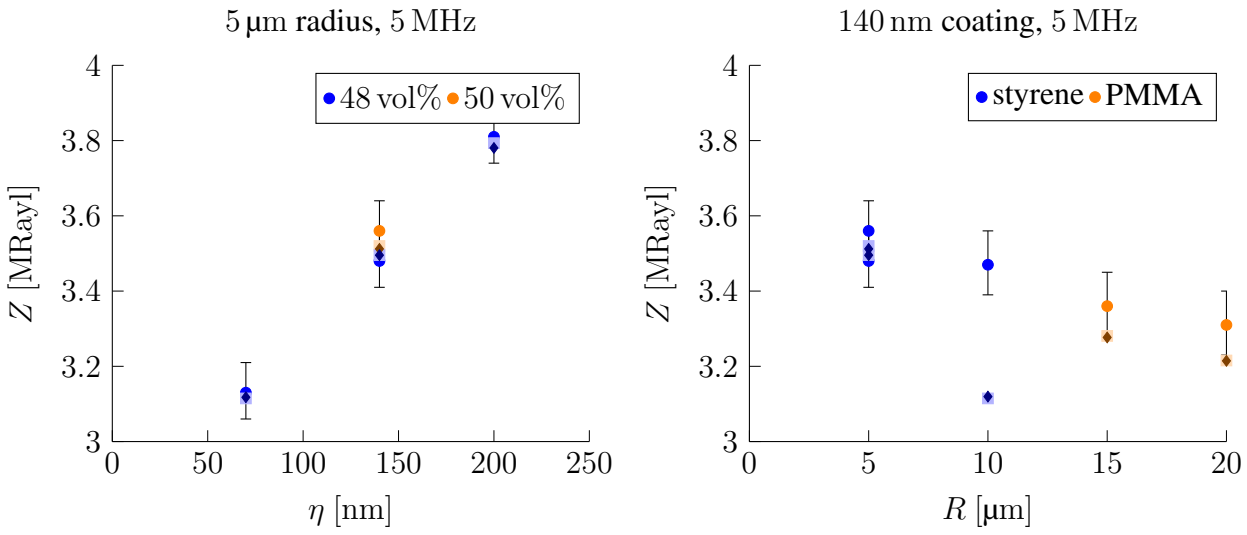

(a) The exact values are tabulated in table 4.1

(b) The exact values are tabulated in table 4.2

Figure 4.1: The measured acoustic impedances from table 3.6 are plotted as circles with error bars representing the shrinking of adhesive. The approximations by the ordered FE model are represented by dark diamonds and TPM by light squares.

Table 4.2: The acoustic impedance of the particles are plotted in fig. 4.1b. The unit of the tabulated impedances are MRayl, and is left out to make the table more readable.

ID	Core	R [µm]	η [nm]	ϑ_p [vol%]	Z^{min}	Z^{eff}	Z^{max}	Z^{TPM}	Z^{FEA}	ϵ^{eff}[%]
CA101-1	styrene	5	140	50	3.5	3.56	3.64	3.52	3.51	1.35
CA101-2	styrene	5	140	48	3.41	3.48	3.56	3.5	3.5	0.44
CA102-2	styrene	10	140	48	3.39	3.47	3.56	3.11	3.12	10.1
CA102-3	PMMA	15	140	48	3.28	3.36	3.44	3.28	3.28	2.48
CA101-4	PMMA	20	140	48	3.23	3.31	3.4	3.22	3.21	2.89

4.2 Numerical Experiment in Design

The results from the procedure in section 3.12 are presented in this section on the following order:

- Young's modulus, E.
- Poisson's ratio, ν.
- Density, ρ.
- Sphere radius, R.
- Shell thickness, η.
- Contact width, ξ.
- Volume fraction of particles, ϑ_p.
- Ideal concentration of silver layer and particles.

We present the results for both the FE models and the TPM in the same tables and figures. It should be noted that the FE model is presented as marks in the plots, whereas the TPM is presented as continuous lines. When we study the elastic properties, the results for all three constituents (core, shell and matrix) are plotted in the same figures. The belonging TPM-lines has the same colours as the FE model marks for the same constituents. The TPM (blue lines) and the FE model (black marks) have different colours when we study the geometric parameters.

4.2.1 Young's Modulus

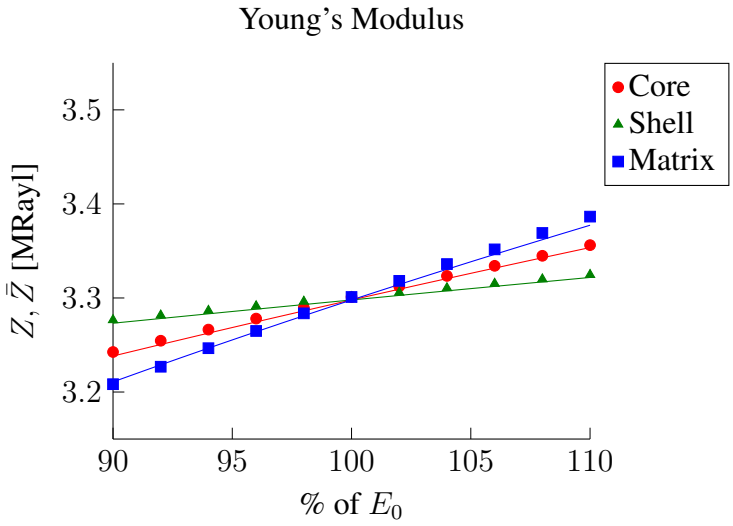

Figure 4.2: The Young's modulus is varied from 90%-110% of the initial Young's modulus, E_0, of the materials. Note that the marks are values approximated using the ordered FE model, whereas the lines are approximated using the TPM.

Table 4.3: Young's modulus of the core.

Core	$E_{100\%}$	$E_{90\%}$	$E_{110\%}$	$\Delta 90[\%]$	$\Delta 110[\%]$
E[GPa]	3.45	3.105	3.795	-	-
Z[MRayl]	3.301	3.243	3.356	1.8	1.7
$\bar{Z}$[MRayl]	3.298	3.238	3.354	1.8	1.7

Table 4.4: Young's modulus of the shell.

Shell	$E_{100\%}$	$E_{90\%}$	$E_{110\%}$	$\Delta 90[\%]$	$\Delta 110[\%]$
E[GPa]	76.0	68.4	83.6	-	-
Z[MRayl]	3.301	3.277	3.325	0.7	0.7
$\bar{Z}$[MRayl]	3.298	3.273	3.322	0.7	0.7

Table 4.5: Young's modulus of the matrix.

Matrix	$E_{100\%}$	$E_{90\%}$	$E_{110\%}$	$\Delta 90[\%]$	$\Delta 110[\%]$
E[GPa]	4.35	3.915	4.785	-	-
Z[MRayl]	3.301	3.208	3.386	2.8	2.6
$\bar{Z}$[MRayl]	3.298	3.211	3.377	2.6	2.4

4.2.2 Poisson's Ratio

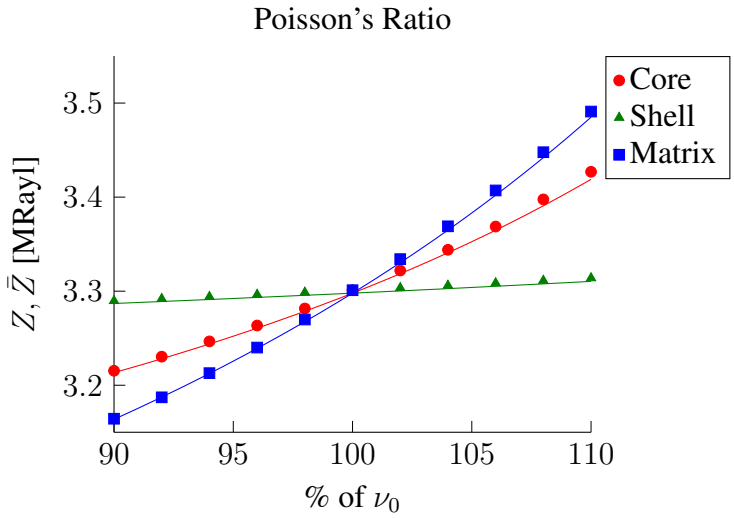

Figure 4.3: The Poisson's ratio is varied from 90%-110% of the initial Poisson's ratio, ν_0, of the material. Note that the marks are values approximated using the ordered FE model, whereas the lines are approximated using the TPM.

Table 4.6: Poisson's ratio of the core.

Core	$\nu_{100\%}$	$\nu_{90\%}$	$\nu_{110\%}$	$\Delta 90[\%]$	$\Delta 110[\%]$
ν	0.3580	0.3222	0.3938	-	-
Z[MRayl]	3.301	3.215	3.427	2.6	3.8
$\bar{Z}$[MRayl]	3.298	3.213	3.419	2.6	3.7

Table 4.7: Poisson's ratio of the shell.

Shell	$\nu_{100\%}$	$\nu_{90\%}$	$\nu_{110\%}$	$\Delta 90[\%]$	$\Delta 110[\%]$
ν	0.370	0.333	0.407	-	-
Z[MRayl]	3.301	3.290	3.314	0.3	0.4
$\bar{Z}$[MRayl]	3.298	3.287	3.310	0.3	0.4

Table 4.8: Poisson's ratio of the matrix.

Matrix	$\nu_{100\%}$	$\nu_{90\%}$	$\nu_{110\%}$	$\Delta 90[\%]$	$\Delta 110[\%]$
ν	0.368	0.331	0.405	-	-
Z[MRayl]	3.301	3.164	3.491	4.1	5.8
$\bar{Z}$[MRayl]	3.298	3.164	3.485	4.1	5.7

4.2.3 Density

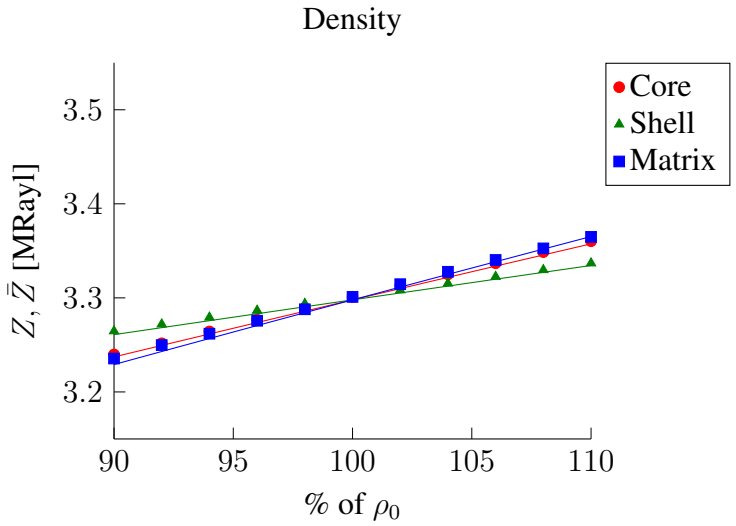

Figure 4.4: The density varied from 90%-110% of the initial density, ρ_0, of the materials. Note that the marks are values approximated using the ordered FE model, whereas the lines are approximated using the TPM.

Table 4.9: Density of the core.

Core	$\rho_{100\%}$	$\rho_{90\%}$	$\rho_{110\%}$	$\Delta 90[\%]$	$\Delta 110[\%]$
$\rho[\mathrm{g\,cm^{-3}}]$	1.05	0.945	1.155	-	-
$Z[\mathrm{MRayl}]$	3.301	3.240	3.360	1.9	1.8
$\bar{Z}[\mathrm{MRayl}]$	3.298	3.237	3.357	1.8	1.8

Table 4.10: Density of the shell.

Shell	$\rho_{100\%}$	$\rho_{90\%}$	$\rho_{110\%}$	$\Delta 90[\%]$	$\Delta 110[\%]$
$\rho[\mathrm{g\,cm^{-3}}]$	10.49	9.441	11.539	-	-
$Z[\mathrm{MRayl}]$	3.301	3.265	3.337	1.1	1.1
$\bar{Z}[\mathrm{MRayl}]$	3.298	3.261	3.334	1.1	1.1

Table 4.11: Density of the matrix.

Matrix	$\rho_{100\%}$	$\rho_{90\%}$	$\rho_{110\%}$	$\Delta 90[\%]$	$\Delta 110[\%]$
$\rho[\mathrm{g\,cm^{-3}}]$	1.12	1.008	1.232	-	-
$Z[\mathrm{MRayl}]$	3.301	3.236	3.365	2.0	1.9
$\bar{Z}[\mathrm{MRayl}]$	3.298	3.229	3.365	2.0	2.0

4.2.4 Radius

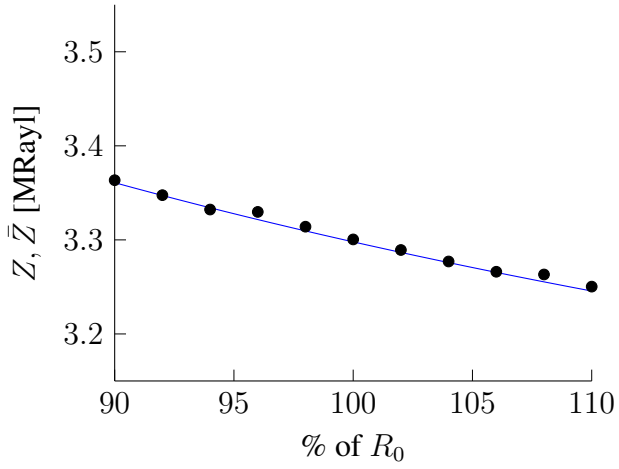

Figure 4.5: The core radius varied from 90%-110% of the initial radius, R_0, of the core. Note that the marks are values approximated using the ordered FE model, whereas the lines are approximated using the TPM.

When we change the core radius whilst keeping the shell thickness and volume fraction of particles constant, we change two parameters; the volume fraction of the core and the volume fraction of the shell. If we increase the R, we reduce the amount of silver, because the volume fraction of silver per particle is reduced, reducing the total volume fraction of silver. Let us assume that the thinnest shell possible to manufacture is $100\,\mathrm{nm}$. We can then reduce the volume fraction by increasing the core radius. We therefore want to see how much the change of core radius with a constant shell thickness will change the overall properties. We can expect a decrease in acoustic impedance.

$$90\%R_0 \leq R \leq 110\%R_0, \quad \eta = \eta_0, \quad \vartheta_p = \vartheta_{p0}. \tag{4.1}$$

Table 4.12: Radius of the core.

Radius	$R_{100\%}$	$R_{90\%}$	$R_{110\%}$	$\Delta 90[\%]$	$\Delta 110[\%]$
$R[\mu\mathrm{m}]$	10.0	9.0	11.0	-	-
$Z[\mathrm{MRayl}]$	3.301	3.363	3.250	1.9	1.5
$\bar{Z}[\mathrm{MRayl}]$	3.298	3.361	3.246	1.9	1.6

4.2.5 Shell Thickness

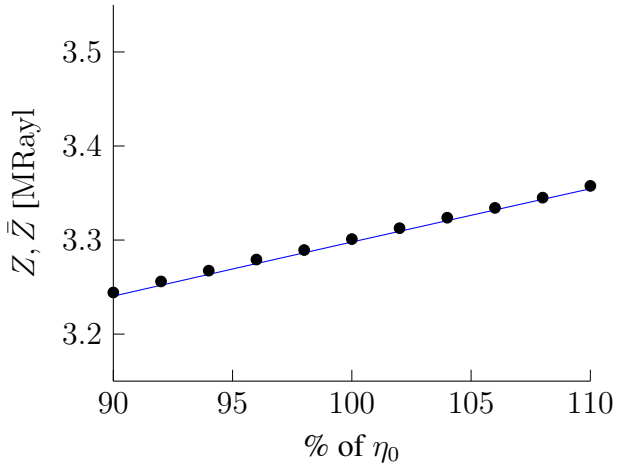

Figure 4.6: The shell thickness varied from 90%-110% of the initial thickness, η_0, of the shell. Note that the marks are values approximated using the ordered FE model, whereas the lines are approximated using the TPM.

The most direct and obvious way of increasing the amount of silver in the model, is to increase the shell thickness. By changing the thickness of silver, we increase the radius of the particle, and thus we reduce the volume fraction of the core. We can expect an increase in acoustic impedance

$$R = R_0, \quad 90\%\eta_0 \leq \eta \leq 110\%\eta_0, \quad \vartheta_p = \vartheta_{p0}. \tag{4.2}$$

Table 4.13: Thickness of the shell.

Thickness	$\eta_{100\%}$	$\eta_{90\%}$	$\eta_{110\%}$	$\Delta 90[\%]$	$\Delta 110[\%]$
$\eta[\mu m]$	0.2	0.18	0.22	-	-
Z[MRayl]	3.301	3.244	3.357	1.7	1.7
$\bar{Z}$[MRayl]	3.298	3.240	3.354	1.7	1.7

4.2.6 Scaling

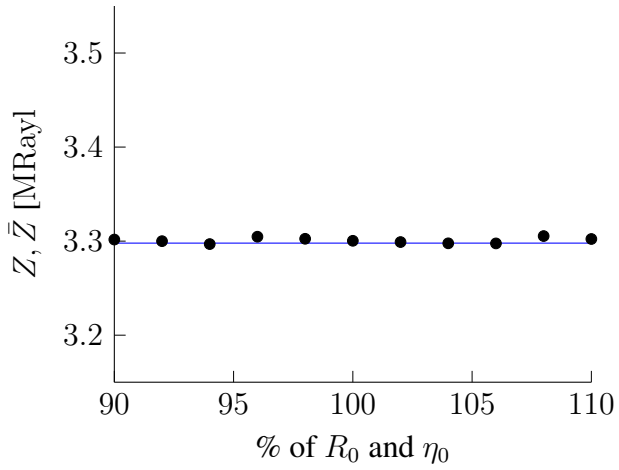

Figure 4.7: The radius and shell thickness is varied from 90%-110% of the initial radius and thickness, R_0 and η_0. Note that the marks are values approximated using the ordered FE model, whereas the lines are approximated using the TPM.

We want to investigate how the size of the particle changes the overall properties. By increasing the radius whilst keeping the shell and particle fraction constant, we can see how much the particle size affects the overall velocity. We alter the core radius, whilst keeping the volume fraction of particles constant, i.e.:

$$90\%R_0 \leq R \leq 110\%R_0, \quad \eta = \frac{R}{R_0}\eta_0, \quad \vartheta_p = \vartheta_{p0}. \tag{4.3}$$

Table 4.14: Scaling of the particle.

Scaling	$R_{100\%}, \eta_{100\%}$	$R_{90\%}, \eta_{90\%}$	$R_{110\%}, \eta_{110\%}$	$\Delta 90[\%]$	$\Delta 110[\%]$
R[µm]	10.0	9.0	11.0	-	-
η[µm]	0.2	0.18	0.22	-	-
Z[MRayl]	3.300	3.302	3.302	0.0	0.0
$\bar{Z}$[MRayl]	3.298	3.298	3.298	0.0	0.0

4.2.7 Contact Width

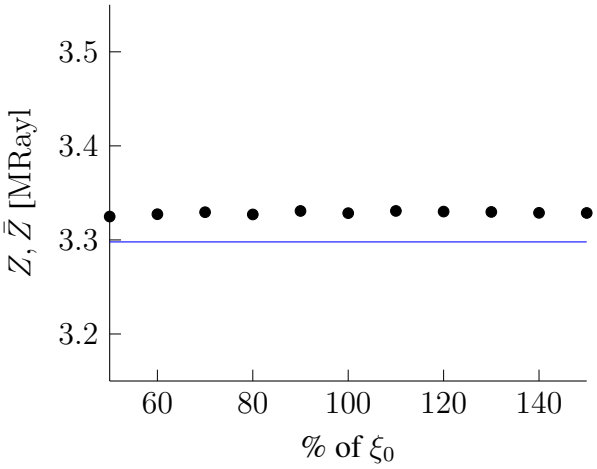

Figure 4.8: The contact width is varied from from 50%-150% of the initial contact width, ξ_0. Note that the marks are values approximated using the ordered FE model, whereas the lines are approximated using the TPM.

The contact width between the particles is believed capable to be altered by increasing the amount of silver ions, Ag^+, in the adhesive before curing. These ions might then move along the shell and "solder" the particles together. How it is done is not of importance, let us just say it is possible. By increasing the contact width, we also increase the amount of silver in the material and reduce the amount of matrix material. Note that the velocity is approximated correctly in ABAQUS, but when we calculate the impedance in post-processing, the density multiplied with the velocity in the equation for acoustic impedance does not include the additional silver due to the contact width. The density used to calculate the impedance is therefore slightly less than the actual amount.

$$R = R_0, \quad \eta = \eta_0, \quad \vartheta_p = \vartheta_{p0}, \quad 50\%\xi_0 \leq \xi \leq 150\%\xi_0. \tag{4.4}$$

Table 4.15: Contact width between particles.

Contact Width	$\xi_{100\%}$	$\xi_{50\%}$	$\xi_{150\%}$	$\Delta 50[\%]$	$\Delta 150[\%]$
ξ[µm]	1.0	0.5	1.5	-	-
Z[MRayl]	3.329	3.245	3.329	0.1	0.0
$\bar{Z}$[MRayl]	3.298	3.298	3.298	0.0	0.0

4.2.8 Volume Fraction of Particles

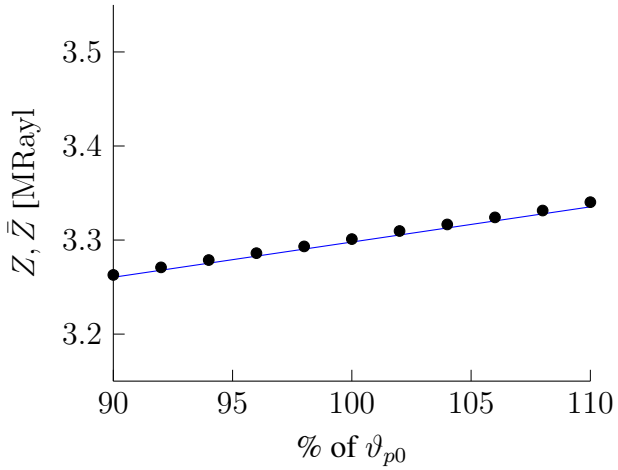

Figure 4.9: The particle concentration is varied from from 90%-110% of the actual contact width, ϑ_{p0}. Note that the marks are values approximated using the ordered FE model, whereas the lines are approximated using the TPM.

By decreasing the particle fraction, we decrease the amount of core material and shell material, and increase the amount of matrix material. Since the core material is polystyrene, we expect an increase in acoustic impedance when we decrease the volume fraction of core material, but a reduction in silver would mean a decrease in impedance. These two effects work against each other, so the expected effect is somewhat unclear when we changing the volume fraction of particles.

$$R = R_0, \quad \eta = \eta_0, \quad 90\%\vartheta_{p0} \leq \vartheta_p \leq 110\%\vartheta_{p0}. \tag{4.5}$$

Table 4.16: Volume fraction of particles.

volume fraction	$\vartheta_{p100\%}$	$\vartheta_{p90\%}$	$\vartheta_{p110\%}$	$\Delta 90[\%]$	$\Delta 110[\%]$
$\vartheta_p[\%]$	50	45	55	-	-
$Z[\text{MRayl}]$	3.301	3.263	3.340	1.2	1.2
$\bar{Z}[\text{MRayl}]$	3.298	3.260	3.335	1.1	1.1

4.2.9 Ideal Concentration

The velocity and impedance with respect to the volume fraction of shell in the particles are plotted in fig. 4.10. The volume fraction of particles, ϑ_p, is 0.5. The velocity does indeed decrease with an increase in shell fraction. However, it is the acoustic impedance that is of interest, which increases with the shell fraction. The velocity and impedance with respect to the volume fraction of particles, ϑ_p, is plotted in fig. 4.11. The velocity decreases with an increased volume fraction and the acoustic impedance increases.

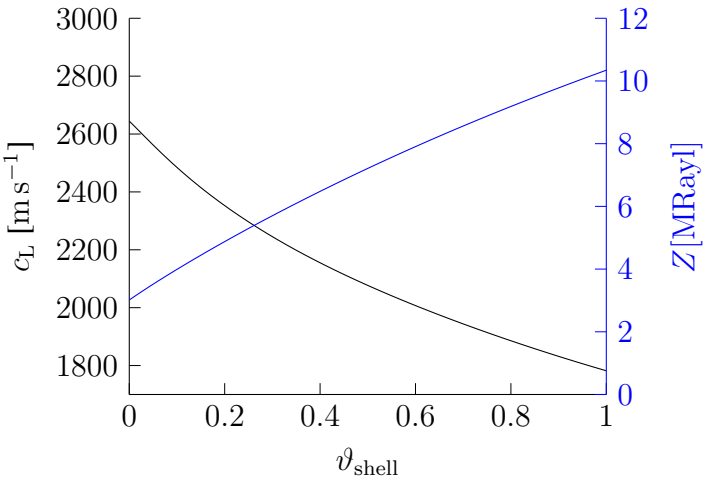

Figure 4.10: The volume fraction of shell in the particle is varied from 0 to 1.The velocity and acoustic impedance is approximated using the TPM.

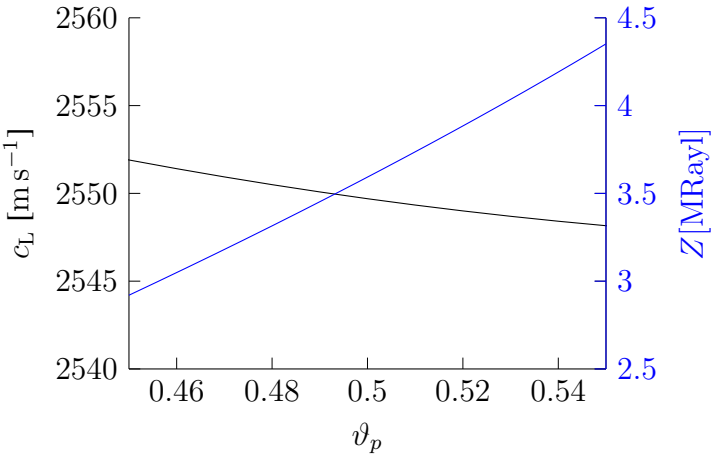

Figure 4.11: The volume fraction of particles is varied from 0.45 to 0.55.The velocity and acoustic impedance is approximated using the TPM.

Chapter 5

Discussion

In this chapter we discuss the assumptions made in the FE model. We then discuss how well the FE model and TPM describes the ICA, based on the results in found in sections 4.1 and 4.2 as well as discussing the design of the composite.

5.1 FE Model Approximations

We modelled the composite using axisymmetric elements in ABAQUS. This assumption introduces a systematic ordering of particles. If we assume that waves only propagate along the z-direction, the waves furthest out in the r-direction will not propagate through any particles, whereas waves at the center will propagate through the center of all particles. Christensen states in [7] that for the heterogeneous composite to provide an attenuation effect, due to incoherent scattering by the inhomogeneities, it must be of a random nature. Christensen also says that in many practical problems, a heterogeneous material can be assumed homogeneous (in the manner of scattering effects) if the inhomogeneities are small compared to the wave length. If we use the wavelength found in eqs. (3.48) and (3.49) and the diameter of the particles as the characteristic length of the

inhomogeneities, we see that the particles with a diameter of $30\,\mu\mathrm{m}$ is

$$\frac{2R}{\Lambda_L^{PMMA}} \approx 5.9\,\%, \tag{5.1}$$

$$\frac{2R}{\Lambda_L^{PS}} \approx 6.2\,\%, \tag{5.2}$$

of the wavelength, thus attenuation due to scattering is not of an issue and the axisymmetric simplification is acceptable. However, there is attenuation in the composite. Friction due to sliding contact between particle-adhesive and particle-particle and viscoelastic effects are sources of loss. We have in the FE models assumed perfect bonding between the constituents which neglects the loss of friction. It is a fair assumption because the scope of this thesis has been to give clarity to how the elastic properties and geometric parameters affect the acoustic impedance. This is also the reason for why we used an elastic representation of the viscoelastic polymers. The mechanical loss in a material used as a transducer layer is of great interest, and we would recommend in a later study to simulate it by introducing a *loss interface layer* surrounding the particles like what has been done in [17]. This layer lumps together possible loss mechanisms and provides a mean for describing the composite behaviour without knowing what happens at the interface. Parameters deciding the size and loss in the layer can then be decided be doing a curve fit with measured attenuation.

5.2 Comparing the FE Model with the ICA

The results in fig. 4.1 and tables 4.1 and 4.2 tells us that the deviations between the measured values and the approximations are small. For the particles with a core radius $5\,\mu\mathrm{m}$, the error is below $1.35\,\%$. The particles with a shell thickness $140\,\mathrm{nm}$, has an error below $2.89\,\%$. The exception being the material sample "CA102-2", which has a relative error of $10.1\,\%$. It should be noted that the density used in the approximations corresponds to the adhesive without any shrinking. Therefore, the approximations should be at the bottom of the error bars. The results seem therefore better than they are, as the approximations seem to overestimate the acoustic impedance of the composite. The best match is for the particles with PMMA as the core material and a shell thickness of $140\,\mathrm{nm}$, as these are closest to the minimum. This is not entirely correct, because the composite samples used

in the experimental measuring probably have experienced some shrinking. From the expression of the longitudinal velocity in eq. (2.32), which we repeat here for convenience

$$c_L^2 = \frac{\lambda + 2\mu}{\rho}, \tag{2.32}$$

we see how a higher density (caused by shrinking) will reduce the velocity. Let us say we know the density of the sample; ρ^{eff}. If we want to calculate the minimum and maximum impedance, we should consider how the density might differ when measuring the velocity as well

$$(c_L^{\text{min}})^2 = \frac{\lambda + 2\mu}{\rho^{\text{eff}}} \cdot \frac{\rho^{\text{eff}}}{\rho^{\text{min}}}, \tag{5.3}$$

$$(c_L^{\text{max}})^2 = \frac{\lambda + 2\mu}{\rho^{\text{eff}}} \cdot \frac{\rho^{\text{eff}}}{\rho^{\text{max}}}. \tag{5.4}$$

The density of the composite "CA101-2", which has particles of radius $5\,\mu\text{m}$, shell thickness $140\,\text{nm}$ and a particle packing of $48\,\text{vol}\%$, can be found to be

$$\rho^{\text{min}} = 1.48\,\text{g}\,\text{cm}^{-3}, \quad \rho^{\text{eff}} = 1.51\,\text{g}\,\text{cm}^{-3} \quad \text{and} \quad \rho^{\text{max}} = 1.54\,\text{g}\,\text{cm}^{-3}, \tag{5.5}$$

where min, eff and max corresponds to $0\,\%$, $5\,\%$ and $10\,\%$ shrinking of the adhesive, respectively. Substituting eq. (5.5) in eqs. (5.3) and (5.4) yields,

$$(c_L^{\text{min}})^2 = (c_L^{\text{eff}})^2 \cdot 1.02, \tag{5.6}$$

$$(c_L^{\text{max}})^2 = (c_L^{\text{eff}})^2 \cdot 0.98, \tag{5.7}$$

which slightly compensate for the change in density when we calculate the acoustic impedance. The error bars in fig. 4.1 should therefore be shorter. The measured impedance and the approximations do show a good match, but because of the numerous sources of error we cannot say if the approximations over or underestimates the acoustic impedance. We therefore agree with SURF Technology to do new measurements on samples with diameter $25\,\text{mm}$ and a smoother surface. A better control of the shrinking process should be emphasized.

5.3 Numerical Experiment in Design

Our first observation from the results in figs. 4.2 to 4.8 is that there is good match between the FE models with a size above the homogeneous limit and the TPM. It may therefore be possible to use the TPM to approximate the properties of homogeneous representation of the heterogeneous ICA. The TPM assumes spherically shaped particles, which in our case does not involve an approximation. The ICA consists of monodisperse coated particles, and for both steps in our two-step scheme, described in section 3.9, the inclusions are spherical; first the spherical core is embedded in the silver matrix, then the effective homogeneous spherical particle is embedded in the epoxy matrix. The use of perfectly shaped spheres may be the reason for the good fit between our FE approximations and the TPM.

The most sensitive elastic parameter is the Poisson's ratio of the matrix material, as we can see from table 5.1. When it is changed to $110\,\%$ of ν_0 the acoustic impedance increases by $5.8\,\%$. We mentioned in the opening of this chapter how there is an uncertainty in the matrix density (due to shrinking of the adhesive during curing) of approximately $10\,\%$. From the result in table 4.11, a $10\,\%$ uncertainty in matrix density results in an uncertainty of $2\,\%$ in the acoustic impedance of the composite. The parameters and properties that changes the impedance the most are listed in table 5.1. It shows that the three elastic properties of the matrix material are among the top four, which tells us that altering the matrix material makes the biggest impact on the acoustic impedance. We will therefore recommend changing the matrix material to reduce the acoustic impedance. Even though the Poisson's ratio is lower for PMMA, the Young's modulus and density is greater, so we would recommend using polystyrene as the core material.

In section 3.10.3, we made a statement that there may be an ideal ratio of core and shell, because the velocity was reduced when silver was added. In fig. 4.10 we used the TPM to plot the velocity and acoustic impedance of the composite while varying the core-shell ratio and the volume fraction of particles. If the TPM is trustworthy, which it seems to be by the match in figs. 4.2 to 4.9, it tells us that the velocity is decreasing with the increase of silver, while the acoustic impedance is increasing. Because we are interested in a low impedance composite, we see from fig. 4.11 that no particles give the lowest impedance. If we have a particle fraction, $\vartheta_p = 50\,\mathrm{vol}\%$, fig. 4.10 tells

Table 5.1: The parameters are sorted from the most to the least sensitive to change with respect to the acoustic impedance. This table is just a reordering of the results found in section 4.2

Parameter	$\Delta 90$ [%]	$\Delta 110$ [%]
ν_{matrix}	4.1	5.8
ν_{core}	2.6	3.8
E_{matrix}	2.8	2.6
ρ_{matrix}	2	1.9
ρ_{core}	1.9	1.8
E_{core}	1.8	1.7
R	1.9	1.5
η	1.7	1.7
ϑ_p	1.2	1.2
ρ_{shell}	1.1	1.1
E_{shell}	0.7	0.7
ν_{shell}	0.3	0.4
R, η	0	0
ξ	0	0

us that particles without shell gives the lowest acoustic impedance. The composite is introduced to increase the thermal conductivity, and therefore should include a layer of silver. The thickness of the silver will increase the impedance, and it must therefore be made a trade-off between the acoustic impedance and the thermal conductivity. To reduce the thermal contact resistance, we can reduce the number of contact points between particles by increasing the size of the particles. The particles can be scaled such that the core-shell ratio is constant, which we have seen from section 4.2.6 do not alter the acoustic impedance. We sum up our most important observations:

- The TPM is just as good as the FE model to approximate the homogeneous properties of the material. However, the $\Lambda/4$ layer might be too thin to be assumed homogeneous.
- It is the adhesive material that changes the acoustic impedance the most, second is the core material. We therefore recommend looking at other options for adhesive material, and we recommend using polystyrene over PMMA as the core material.
- Larger particles increases the thermal conductivity, and as long as they are scaled, the size do no alter the acoustic impedance.

Chapter 6

Conclusion

The work conducted in this thesis concerns the development of a method to approximate the acoustic impedance of composites comprising silver coated polymer spheres in a polymer adhesive using FEA. Our results agree well with both real values and the analytic TPM. The TPM proves to be an efficient and cheap method to approximate the homogeneous acoustic impedance, and if we only are interested in the homogeneous approximation of the heterogeneous ICA, the TPM is just as good as the FE model. However, we show that the composite used as a transducer layer may be too thin to be assumed homogeneous at a macroscopic level. We have not succeeded in finding an ideal geometric configuration that will give both a low acoustic impedance as well as a high thermal conductivity, as these properties are inversely proportional to each other. However, larger particles are favourable to increase the thermal conductivity, and as long as the particles are scaled, we have not seen any change in acoustic impedance. In conclusion, large particles are better to use in an isolation layer, and polystyrene is more favourable than PMMA as the core material.

6.1 Future Work

Much of the work in this thesis has gone into understanding how the mechanical properties of a composite material alter its acoustic impedance. There is much more to learn and many factors that can be included. We will end by summing up some future work that would be interesting to do:

- Test whether the $\Lambda/4$ thick composite can be assumed homogeneous by measure the acous-

tic impedance on samples at approximately a $\Lambda/4$ thickness. These samples should have a diameter of about $25\,\mathrm{mm}$ and a smooth surface.

- Measure the longitudinal and transverse sound velocity on adhesive samples to calculate the mechanical properties.
- Do analyses and measurements with different centre frequencies, such that it might be possible to find a mathematical expression for the homogenization height, δ, with respect to the wavelength, particle size and shell thickness.
- Use viscoelastic material model when modelling the polymers, to study viscous loss.
- Include loss interface layers similar to what has been done in [17].
- Simulate thermal conductivity in a three-dimensional model and do a experimental study in design with respect to thermal conductivity.

Bibliography

[1] ABAQUS, D. S., 2010. Version 6.11 documentation. Dassault Systemes.

[2] Aggelis, D., Tsinopoulos, S., Polyzos, D., 2004. An iterative effective medium approximation (iema) for wave dispersion and attenuation predictions in particulate composites, suspensions and emulsions. The Journal of the Acoustical Society of America 116 (6), 3443–3452.

[3] Angelsen, B. A., 2000. Ultrasound imaging: waves, signals, and signal processing. Vol 1. Emantec.

[4] Bell, K., 2015. Engineering approach to finite element analysis of linear structural mechanics problems. Akademica Publishing.

[5] Christensen, R., Lo, K., 1979. Solutions for effective shear properties in three phase sphere and cylinder models. Journal of the Mechanics and Physics of Solids 27 (4), 315–330.

[6] Christensen, R. M., 1990. A critical evaluation for a class of micro-mechanics models. Journal of the Mechanics and Physics of Solids 38 (3), 379–404.

[7] Christensen, R. M., 2005. Mechanics of Composite Materials. Dover Publications.

[8] Cook, R. D., et al., 2007. Concepts and applications of finite element analysis. John Wiley & Sons.

[9] Gakkestad, J., Li, Z., Helland, T., Wong, C., 2013. Thermo-mechanical properties of isotropic

conductive adhesive filled with metallized polymer spheres. In: Electronics Packaging Technology Conference (EPTC 2013), 2013 IEEE 15th. IEEE, pp. 213–218.

[10] Graff, K. F., 1975. Wave Motion in Elastic Solids. Dover Publications.

[11] Hopperstad, O., Børvik, T., 2015. Material Mechanics Part I.

[12] Irgens, F., 2008. Continuum mechanics. Springer Science & Business Media.

[13] Jacovitti, G., Scarano, G., 1993. Discrete time techniques for time delay estimation. IEEE Transactions on signal processing 41 (2), 525–533.

[14] Jain, S., Whalley, D., Cottrill, M., Helland, T., Kristiansen, H., Redford, K., Liu, C., 2013. The effect of coating thickness on the electrical performance of novel isotropic conductive adhesives prepared using metallised polymer micro-spheres. In: Electronic Components and Technology Conference (ECTC), 2013 IEEE 63rd. IEEE, pp. 796–802.

[15] Jain, S., Whalley, D. C., Cottrill, M., Kristiansen, H., Redford, K., Nilsen, C., Helland, T., Liu, C., 2011. Electrical properties of an isotropic conductive adhesive filled with silver coated polymer spheres. In: Microelectronics and Packaging Conference (EMPC), 2011 18th European. IEEE, pp. 1–7.

[16] Kerner, E., 1956. The elastic and thermo-elastic properties of composite media. Proceedings of the physical society. Section B 69 (8), 808.

[17] Marra, S., Ramesh, K., Douglas, A., 1999. The mechanical properties of lead-titanate/polymer 0–3 composites. Composites science and technology 59 (14), 2163–2173.

[18] MatWeb, L., 2017. Matweb—material property data. Accessed: 2017-04-08.

[19] Myhre, O. F., Johansen, T. F., Angelsen, B. A. J., 2017. Analysis of acoustic impedance matching in dual-band ultrasound transducers. The Journal of the Acoustical Society of America 141 (2), 1170–1179.
URL http://dx.doi.org/10.1121/1.4976096

[20] Myhre, O. F., Johansen, T. F., Johan Angelsen, B. A., 2017. Analysis of acoustic impedance matching in dual-band ultrasound transducers. The Journal of the Acoustical Society of America 141 (2), 1170–1179.

[21] Pettersen, S. R., Kristiansen, H., Nagao, S., Helland, S., Suganuma, K., Zhang, Z., He, J., et al., 2016. Contact resistance and metallurgical connections between silver coated polymer particles in isotropic conductive adhesives.

[22] Rose, J. L., 2014. Ultrasonic guided waves in solid media. Cambridge University Press.

[23] Wu, J., 1996. Determination of velocity and attenuation of shear waves using ultrasonic spectroscopy. The Journal of the Acoustical Society of America 99 (5), 2871–2875.